Published for SISSA by Springer

Received: *August 21, 2025*
Accepted: *December 28, 2025*
Published: *February 16, 2026*

Trapping, chaos and averaging in bubbling AdS spaces

David Berenstein,[a,b,c] **Mihailo Čubrović**[d] **and Vladan Đukić**[d]

[a] *Department of Physics, University of California, Santa Barbara, CA 93106, U.S.A.*
[b] *Institute of Physics, University of Amsterdam, Science Park 904, PO Box 94485, 1090 GL Amsterdam, The Netherlands*
[c] *Delta Institute for Theoretical Physics, Science Park 904, PO Box 94485, 1090 GL Amsterdam, The Netherlands*
[d] *Center for the Study of Complex Systems, Institute of Physics Belgrade, University of Belgrade, Pregrevica 118, 11080 Belgrade, Serbia*

E-mail: dberenstein@ucsb.edu, cubrovic@ipb.ac.rs, djukic@ipb.ac.rs

Abstract: We discuss chaos and ensemble averaging in 1/2 BPS bubbling AdS spaces of Lin, Lunin and Maldacena (LLM) by studying trapped and escaping null geodesics and estimating their decay rates. We find typical chaotic scattering behavior and confirm the Pesin relation between escape rates, Lyapunov exponents and Kolmogorov-Sinai entropy. On the other hand, for geodesics in coarse-grained (grayscale) LLM geometries (which exhibit a naked singularity) chaos is strongly suppressed, which is consistent with orbits and escape rates averaged over microscopic backgrounds. Also the singularities in these grayscale geometries produce an attractive potential and have some similarities to black hole throats trapping geodesics for a long time. Overall, averaging over the ensembles of LLM geometries brings us closer toward the typical behavior of geodesics in black hole backgrounds, but some important differences remain, in particular the existence of a threshold timescale when the averaging fails.

Keywords: Black Holes in String Theory, AdS-CFT Correspondence, Spacetime Singularities, Models of Quantum Gravity

ArXiv ePrint: 2508.09669

https://doi.org/10.1007/JHEP02(2026)157

Contents

1 Introduction

The bubbling AdS space solutions of Lin, Lunin and Maldacena (LLM) [1] are an excellent playground for studying the microscopic physics of smooth geometries, without horizons or singularities, obtained as top-down string theory solutions, and yet with some resemblance to black holes. They preserve 16 SUSY generators (they are half BPS). The spacetimes are a warped product of a four-dimensional manifold and two three-spheres, and they have an $SO(4) \times SO(4) \times \mathbb{R}$ spacetime symmetry. These geometries are solutions of type IIB SUGRA, holographically dual to a 1/2 BPS state of $\mathcal{N} = 4$ SYM on $\mathbb{S}^3 \times \mathbb{R}$. The LLM geometries can be completely reconstructed from solving a boundary value problem for a PDE, where the boundary is a two dimensional plane (known as the LLM plane) and the boundary conditions are determined from regularity of the ten dimensional metric. The regularity condition produces a two coloring of the LLM plane. They can be described as a state in the lowest Landau level (LLL) in a quantum Hall fluid and the dual field theory can be formulated as a quantum mechanical matrix model [2]. In M-theory it is U-dual to the solution of Bena and Warner [3]. The representation in terms of the LLL of a Fermi fluid yields a very intuitive picture of the solution: the two-dimensional Fermi surface of the

JHEP02(2026)157

fluid divides a plane into black areas (particles) and white areas (holes); the geometry and topology of the black and white patterns classifies completely the solutions [4].

As was noted in [5], LLM geometries are not the best test case for fuzzball geometries, aimed to describe black holes as approximations to smooth string theory solutions, since the corresponding 1/2 BPS "black hole" does not have a horizon, but a naked singularity [6]. The singular generalization, known as the superstar or grayscale solution [6–8], is obtained by generalizing the boundary conditions in the LLM plane: normally, only one of the two three-spheres has vanishing radius in the plane; in superstar/grayscale solutions, the radius of both spheres shrink to zero, which produces a singularity. Crucially, this can be understood as coarse-graining over small-scale details of black and white patterns of solutions, very much in line with the idea of ensemble averaging in gravity [9–14]. The purpose of this paper is to explore explicitly if the averaged, grayscale backgrounds also yield ensemble-averaged observable physics.

Despite the fact that the averaged geometry is not a black hole but just a naked singularity, we still hope to capture some interesting phenomenological insights into the question if black holes can be understood as ensemble-averaged objects, or more specifically how to distinguish microstate geometries from black holes. This is in a similar philosophy to [8], which explores other aspects of the emergent horizon.

Geodesic motion and equations of motion for particles and fields in black hole spacetimes like the Schwarzschild solution, which is described just by general relativity, are all well known to be integrable (separable), while this is not the case for a generic member of some class of microstate geometries [15–17]. The smoking gun for integrability is the existence of the Killing-Yano conformal tensor [15, 17]. It turns out that hidden conformal symmetries, which are responsible for the separability of the wave equation, also allow one to construct the holographic dual CFT description for generic black holes, both supersymmetric and non-supersymmetric ones (and further to use it correctly calculate the black hole entropy via the Cardy formula [18–21]). On the other hand, if the smooth microstate geometries are to look like a black hole, we expect the following features that mimic the physics of geometries with horizons: trapping of generic infalling geodesics and diffusion dynamics near the horizon. It is hard to imagine that these can be obtained if the motion of geodesics is integrable in the ensemble of microstate geometries. In that case we expect that the motion is quasiperiodic and that the periods of the action-angle variables are not too different from the light-crossing time of the black hole region. Chaos (non-integrability) is obviously the key for understanding how generic microstate geometries can both mimic aspects of black holes, and on the other hand differ from them crucially by not having a singularity. For example, there is a large number of periodic orbits in time independent Hamiltonian chaotic systems, although they are still a set of zero measure. Other solutions can stay very close to these periodic orbits for a long time and they might seem trapped if the periodic orbit they are close to is "deep inside the black hole region". Also, since in chaotic systems we expect mixing in phase space, these can give properties similar to diffusion.

This motivates our study of chaotic features of null geodesics in LLM backgrounds. The non-integrable character of such geodesics is in contrast with the bulk integrability of most black hole backgrounds, while the "weak" chaos that is present in the dual CFT description

JHEP02(2026)157

("BPS chaos", studied in [22]) is again in discrepancy with the maximal chaos of thermal gauge theories, i.e. the well-known fact that black holes are the fastest scramblers, based on the MSS bound $\lambda \leq 2\pi/\hbar\beta$ [23]. On the other hand, even when the bulk dynamics of some simple probes is integrable, for example in the presence of thermal horizons, the MSS bound seems to hold and can be related via the QNM spectrum to the thermalization time scales in the dual gauge theory [24]. This is the case because the Lyapunov exponent is not the best indicator of chaos, since it can also be positive in the presence of an unstable saddle point in an otherwise integrable system. Thus along the lines of that research direction our final goal would be to construct the holographic dictionary for chaos that would be valid regardless of the presence or absence of thermal horizons. It has been argued indirectly that essentialy all LLM geometries produce chaotic dynamics [16], except for the global $AdS_5 \times S^5$ ground state. Chaos has already been established numerically for a subset of null geodesics that reside inside the LLM plane in *generic* LLM geometries [25]. These become integrable when one imposes one additional restriction: rotational symmetry in the LLM plane. Hence, it is also interesting to investigate geodesics outside the LLM plane for these setups, which can also be microstates in the grayscale setup. Moreover, one usually imagines that the horizon of the 1/2 BPS black hole when it stops being supersymmetric would form close to the grayscale singular region of the LLM geometry. The motion of infalling geodesics (especially light) into this black hole requires motion in the direction perpendicular to the LLM plane, so it is important to also study geodesic motion in this extra direction. This paper studies such geodesic motion. We find chaos explicitly, even in situation where the in-plane LLM geodesics become integrable.

Clearly, the phenomenology of chaos is intimately related also to the puzzle of averaging, which is especially appealing as it offers a glimpse into the workings of averaging in higher dimensions. In two- and more recently three-dimensional AdS it was argued that the holographic dual of pure quantum gravity is not one single CFT, but rather an average over an ensemble of CFTs [9, 11]. But this feature might well be an artifact of our ignorance about the UV physics [10, 13]. Since supergravity is an effective description of string theory, such solutions are not UV-complete and should therefore also display this averaging feature. The grayscale vs. black and white LLM geometries present a perfect testing ground for this reasoning.

The plan of the paper is the following. In section 2 we study the dynamics of geodesics in black and white ("normal") LLM geometries, and inspect chaos in terms of escape rates, fractal structures and the Pesin relation. In section 3 we perform the same study for the grayscale, singular LLM backgrounds, compare it to the black and white case and show how it can be understood in terms of the ensemble averaging picture. Section 4 summarizes the conclusions.

2 Null geodesics in LLM geometries

2.1 Generalities

In this section we study the dynamics of null geodesic motion in the LLM geometry. Let us first concisely summarize the basics of the LLM solution [1, 3]. Its most appealing feature is that, thanks to the dual matrix model [2], it can be understood as being sourced by a Fermi sea in a two-dimensional plane (the LLM plane), where the inside of the Fermi surface

JHEP02(2026)157

is conventionally considered "black", whereas the holes live in "white" regions. One can learn a lot from a complete classification of the LLM solutions in terms of black and white patterns. Here we will focus on two representative configurations: disk+ring and 3-disk geometries. We are mainly motivated by [25] and we extend their analysis from the geodesics in the LLM plane to full 3D dynamics. This is the residual number of directions that are not determined by conservations laws.

The LLM geometry consists of two 3-spheres, $\widetilde{S}^3$ and S^3, and the 3+1-dimensional spacetime with the x-y plane (LLM plane) located at $\xi = 0$, so that ξ can be interpreted as a radial direction [1]:

$$g_{\mu\nu}dx^\mu dx^\nu = \frac{1}{h^2}\left[-(dt+V_a dx^a)^2 + h^4\left(d\xi^2 + dx_a dx^a\right) + \left(\frac{1}{2}-z\right)d\widetilde{\Omega}_3^2 + \left(\frac{1}{2}+z\right)d\Omega_3^2\right], \tag{2.1}$$

with

$$h^2 = \frac{1}{\xi}\sqrt{\frac{1}{4}-z^2}, \quad \partial_\xi V_a = \frac{\epsilon_{ab}\partial_b z}{\xi}. \tag{2.2}$$

Notice that the radii of the spheres are given by

$$R_1^2 = h^{-2}\left(\frac{1}{2}-z\right), \quad R_2^2 = h^{-2}\left(\frac{1}{2}+z\right) \tag{2.3}$$

and that therefore $R_1^2 R_2^2 = h^{-4}(1/4 - z^2) = \xi^2$. Thus when $\xi \to 0$ necessarily at least one of the spheres degenerates to zero size.

We thus have a family of solutions determined by the function $z(\xi, x, y)$. The equation is obtained from compatibility of the various Killing spinor equations that must be satisfied to preserve the supersymmetries

$$\partial_a\partial_a z + \xi\partial_\xi\left(\frac{\partial_\xi z}{\xi}\right) = 0. \tag{2.4}$$

This function z only depends on the three variables x, y, ξ, so the time direction t has translation symmetry. Given the conservation laws, only motion in x, y, ξ will need to be solved explicitly. For the geometry to be smooth (devoid of singularities) one of the spheres has to vanish in the LLM plane. This leads to the "black and white" picture of the boundary conditions at $\xi = 0$ for the Killing spinor equation:

$$\begin{aligned} &\lim_{\xi\to 0} z = +1/2, && \widetilde{S}^3 \text{ contracts to } 0 \\ &\lim_{\xi\to 0} z = -1/2, && S^3 \text{ contracts to } 0. \end{aligned} \tag{2.5}$$

The regularity condition is that only one sphere shrinks to zero at generic point in the LLM plane, so the function h^2 stays finite.

For example, a black disk in the plane would correspond to the $AdS_5 \times S^5$ geometry. We are interested in more complicated solutions where the integrability of probe geodesics breaks down, specifically:

1. Disk+ring configuration, with a black disk and a black ring concentric with the disk in a white plane (figure 1). This geometry is still integrable in the LLM plane [25] (because

JHEP02(2026)157

of the conserved angular momentum) but the motion in the full 3+1-dimensional space (not counting the spheres) is chaotic. This configuration is straightforwardly generalized to a system of multiple concentric rings.

2. The 3-disk configuration, a set of 3 black disks in the white plane (figure 2). Unless specified otherwise, we use these same parameters for all 3-disk geometries in the paper (disk radii $R = 5$, disks centered at $(x_c, y_c) = (0,0),\ (20,0),\ (10,20)$).

Both setups can be obtained as superpositions of (black and white) circles in the LLM plane. After all, these circle configurations are a complete classification of the quantum states that preserves half the supersymmetry [2]. For disk+rings we prescribe a set of radii $R_1 > R_2 > \dots R_n$. For disk+(single) ring, the main case in this section, we have $n = 3$ and, unless specified otherwise, the radii are $R_1 = 5$, $R_2 = 9$, $R_3 = 10$. The solution to the Killing spinor equation (2.4) for a disk of radius R reads

$$z(\xi, x, y; R) = \frac{\rho^2 + \xi^2 - R^2}{2\sqrt{(\rho^2 + \xi^2 + R^2)^2 - 4\rho^2 R^2}}, \quad \rho^2 \equiv x^2 + y^2. \tag{2.6}$$

Therefore, the full solution is the superposition

$$\tilde{z}_{\text{full}} = \sum_i (-1)^{i+1} \tilde{z}(\xi, x, y; R_i), \quad \tilde{z}(\xi, x, y; R_i) = z(\xi, x, y; R_i) - 1/2. \tag{2.7}$$

In this case we have cylindrical symmetry, so we can employ the polar coordinates $\{x = \rho\cos\phi,\ y = \rho\sin\phi\}$, which brings some additional simplifications: the vector field V_a simplifies to

$$V_\rho = \cos\phi\ V_x + \sin\phi\ V_y = 0, \quad V_\phi = \rho\left(-\sin\phi\ V_x + \cos\phi\ V_y\right). \tag{2.8}$$

For the 3-disk solution, besides the set of disk radii $\{R_1, R_2, R_3\}$, we also need to specify the positions of disk centers $\{(x_{01}, y_{01}), (x_{02}, y_{02}), (x_{03}, y_{03})\}$. The full solution is again the superposition of disks of the form (2.7), with the same solution for a single disk as in (2.6), but now the disk center is not at the origin and all disks are black, therefore:

$$z(\xi,x,y;R,x_0,y_0) = \frac{\rho^2+\xi^2-R^2}{2\sqrt{(\rho^2+\xi^2+R^2)^2-4\rho^2R^2}}, \qquad \rho^2 \equiv (x-x_0)^2+(y-y_0)^2 \tag{2.9}$$
$$\tilde{z}_{\text{full}} = \sum_i \tilde{z}(\xi,x,y;R_i,x_{0i},y_{0i}), \qquad \tilde{z}(\xi,x,y;R_i,x_{0i},y_{0i}) = z(\xi,x,y;R_i,x_{0i},y_{0i}) - 1/2$$

Now that we have specified the backgrounds, we can write down the geodesic equations. We start from the Lagrangian for the null geodesic

$$\mathcal{L} = \frac{1}{2}\, g_{\mu\nu}\left[x(\tau)\right] \dot{x}^\mu(\tau)\dot{x}^\nu(\tau). \tag{2.10}$$

Due to the $\mathrm{SO}(4) \times \mathrm{SO}(4) \times \mathbb{R}$ symmetry, we have a set of three integrals of motion that we label as $\{J_-, J_+, E\}$, following [25]. The Hamiltonian in the general form reads

$$\mathcal{H} = \frac{1}{2h^2}\left[P_\xi^2 + (P_x + EV_x)^2 + (P_y + EV_y)^2 - h^4\left(E^2 - \frac{2J_-^2}{1-2z} - \frac{2J_+^2}{1+2z}\right)\right], \tag{2.11}$$

JHEP02(2026)157

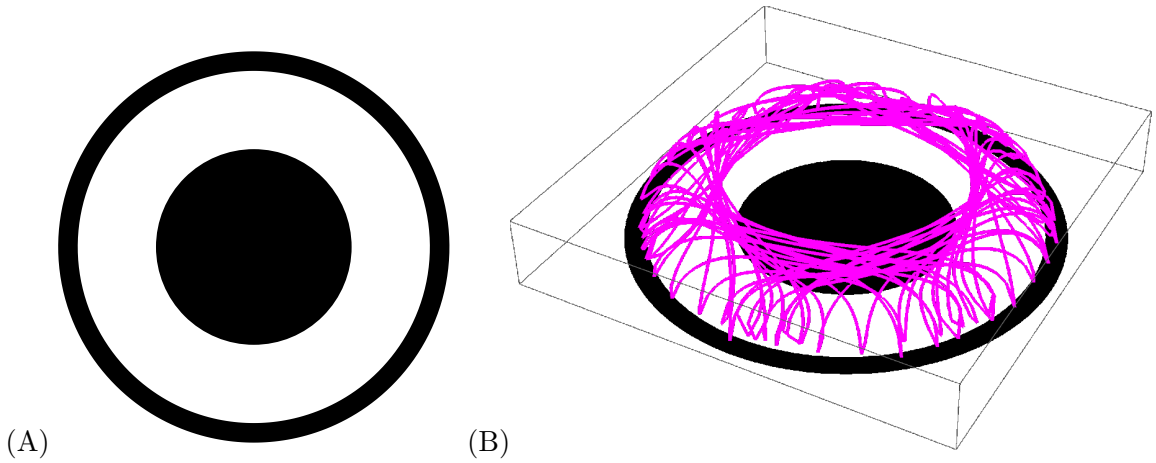

Figure 1. Disk+ring configuration in the LLM plane (A) and the null geodesic (magenta) in the whole 3D space (x, y, ξ) (B) in the same background.

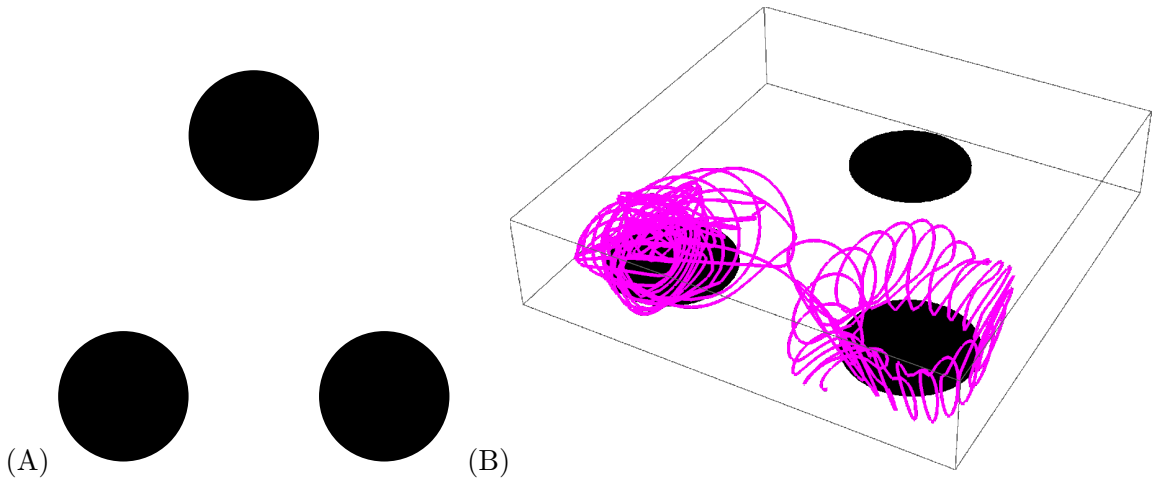

Figure 2. The 3-disk configuration in the LLM plane (A) and a null geodesic (magenta) in the whole 3D space (x, y, ξ) (B) in the same background. Notice how the trajectory can jump between disks after being *trapped* near one for a while to become trapped by another one.

where P_ξ, P_x, P_y are the canonical momenta. The quantity E translates to $\Delta - J$ in the CFT, where Δ is the dimension of the dual operator to the full quantum state of the system and J is its R-charge. This is the departure from being a 1/2 BPS state, where J includes the background geometry, similar to the BMN Hamiltonian [26], see also [27]. The corresponding quantum background state is an eigenstate of $\Delta - J$, but not Δ, J separately.

Since null geodesics are solutions with $\mathcal{H} = 0$, and these are invariant under conformal rescalings of the metric, we can also use the modified Hamiltonian given by

$$\mathcal{H}' = \left[P_\xi^2 + (P_x + EV_x)^2 + (P_y + EV_y)^2 - h^4 \left(E^2 - \frac{2J_-^2}{1-2z} - \frac{2J_+^2}{1+2z} \right) \right], \tag{2.12}$$

which makes it easier to understand the trajectories, as the kinetic term is canonical. The terms EV_x, EV_y produce an effective magnetic field in the directions x, y, ξ. Also, away from

JHEP02(2026)157

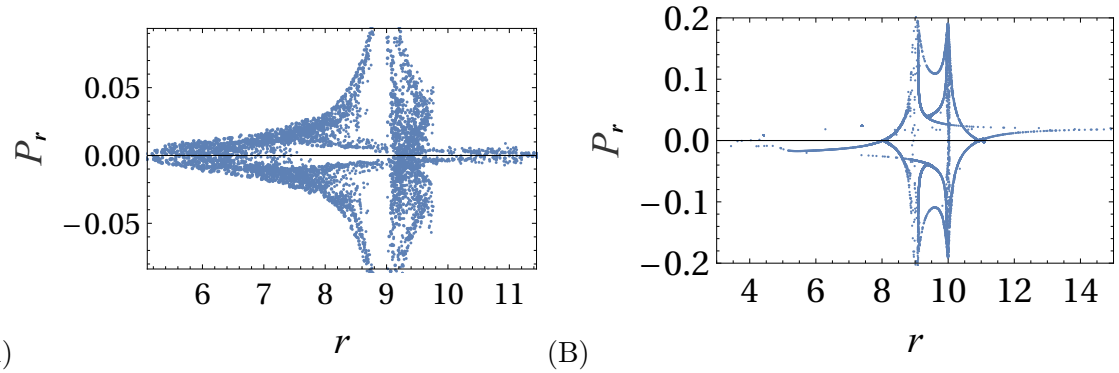

Figure 3. Poincare section $P_\xi = 0$ in $P_r - r$ plane for two sets of null geodesic orbits in the LLM geometry sourced by disk + ring 'source' pattern in a plane. Integrals of motion are $\{J_- = 0.01, J_+ = 0.01, E = 0.1\}$ and $P_\phi = 0.002$. The panels (A) and (B) differ just by boundary conditions: in (B) we see trapping, where orbits explore a smaller volume in phase space, while remaining equally chaotic.

$z = \pm 1/2$ (basically $\xi = 0$), the terms in the effective potential with J_-^2, J_+^2 are regular on the (x, y, ξ) base. In these geometries h is finite at a generic point on the LLM plane, except at the boundaries between black and white regions. There, the metric is still smooth [1], but one needs a change of coordinates to see that it is locally a plane wave geometry. Essentially, the term with $J_-^2/(1-2z)$ provide a repulsive force from the region $z = 1/2$ and the term with $J_+^2/(1+2z)$ provides a repulsive force from the region $z = -1/2$. The trajectories that live inside the LLM plane have either $J_- = 0$ or $J_+ = 0$, so they are very constrained.

2.2 Disk+ring

Following [16], we find that the LLM geometries which are invariant under rotations in the LLM plane, i.e. $\partial_\phi z = 0$, are best dealt with in spherical coordinates:

$$\xi = r \sin\theta, \quad x = r\cos\theta\cos\phi, \quad y = r\sin\theta\sin\phi. \tag{2.13}$$

The Hamiltonian (2.11) in these coordinates reads

$$\mathcal{H}' = 2h^2\,\mathcal{H} = P_r^2 + \frac{P_\theta^2}{r^2} + \frac{(P_\phi + EV_\phi)^2}{r^2\cos^2\theta} - h^4\left(E^2 - \frac{2J_-^2}{1-2z} - \frac{2J_+^2}{1+2z}\right), \tag{2.14}$$

where $V_\phi = r\cos\theta\,(-\sin\phi\,V_x + \cos\phi\,V_y)$. The extra integral of motion (the conserved angular momentum) is P_ϕ. We are thus dealing with a system with two degrees of freedom $\{r, \theta\}$, i.e. a four-dimensional phase space.

In figure 3 we give the Poincare section defined by $P_\theta = 0$ ($P_\xi = 0$). The areas densely filled with points, clearly visible in the panel (A), correspond to the chaotic sea. In the panel (B) we zoom in into a region with long escape times/low escape rate, corresponding to trapped orbits. Here the chaotic sea is much less prominent although as we will see the Lyapunov exponents are of the same order of magnitude. The orbit in figure 1(B) also gives a qualitative idea of the dynamics.

JHEP02(2026)157

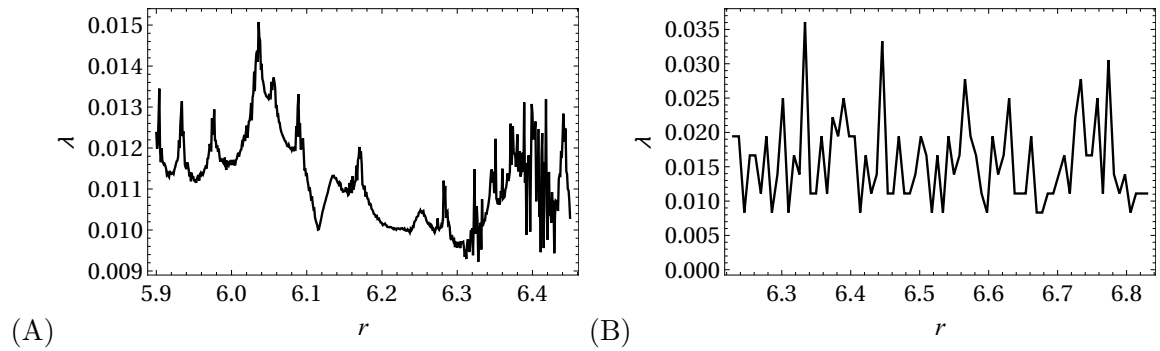

Figure 4. Positive principal Lyapunov exponents for the disk+ring system, with the same initial conditions and integrals of motion as in figure 3. The sticky orbits of figure 3(B) have about the same Lyapunov exponent (even somewhat larger in this case) as the orbits in figure 3(A) which are obviously chaotic.

As a more quantitative chaos indicator and also to check the Pesin theorem, we compute the maximum Lyapunov exponent λ.[1] Similar to [25], we find that λ is non-zero but extremely small — figure 4. This is likely because of the strongly mixed nature of the phase space, with remnants of invariant tori. These are seen as the nearly empty spaces in the Poincare section and will also show up as smooth areas in the escape rate calculation. For some numerical subtleties on computing λ see appendix A.

The central quantity for the deeper questions of our study (how closely can LLM geometries and their ensemble averages mimic black holes?) is the escape rate γ (see figure 5). The rate γ is defined for an ensemble of initial conditions and basically measures how many orbits are still inside the trapped region after time t. However, we first need to define an "escape event". Strictly speaking, an orbit has escaped to infinity (without ever coming back) once it crosses the Lyapunov curves [28]. In practice, computing the Lyapunov curves takes time and is not worth the effort: we just define some arbitrary long-distance cutoff in r and check that the result is reasonably robust to changing the cutoff. One is faced with the same problem when studying chaotic matrix models as toy models of black holes [29] and the problem is treated similarly: one defines an arbitrary cutoff and then checks that the result is robust. There is the additional problem that the AdS geometry is a mirror for particles that try to reach infinity. That means that most null geodesic orbits never get to infinity and return back instead. The only null geodesics that can reach infinity must have one of the angular momentum vanish (the one that corresponds to angular momentum on the S^5). This angular momentum counts as a mass for the particle in AdS and all massive AdS geodesics fail to reach infinity. This is taken care of by specializing to the correct set of geodesics.

To see this effect in the LLM coordinates, notice that the function z satisfies a linear elliptic PDE with bounded boundary conditions similar to a Laplace equation. Since the region in white extends to infinity and the black region does not, for asymptotically large r the value of z tends to that of the white region and produces an effective angular momentum barrier repulsion unless the angular momentum of the corresponding sphere vanishes. This is

[1] This is different from the principal Lyapunov exponents λ_i obtained as the eigenvalues of the variational matrix.

JHEP02(2026)157

how the reflection from the boundary is seen in these coordinates. Asymptotically, this is the three sphere that arises from the S^5, rather than the AdS_5. From the effective reduction to particles moving in AdS_5 with some mass, the mass is given essentially by the angular momentum and these trajectories cannot reach infinity. Escape only makes sense for the orbits that are effectively massless in AdS_5.

For a single orbit (or for a vanishingly small cell of initial conditions in phase space), the escape rate is just the inverse of the escape time: $\gamma_0 = 1/t_{\rm esc}$ (or $\gamma_0 = N_0/t_{\rm esc}$ for N_0 orbits starting infinitely close to each other). However, we can also define the escape rate *coarse-grained over the initial conditions* γ. In this case, we start from a finite-sized (but still small) cell with N orbits with different initial conditions inside the cell. The escape rate is then given by

$$N(t) \sim N_0 e^{-\gamma t} \quad \Rightarrow \quad \gamma \equiv -\frac{\dot{N}}{N}, \tag{2.15}$$

which of course only holds until some late time when the ensemble is almost depleted.

It is necessary to make the cell sufficiently small so that it does not encompass very different regions of phase space (chaotic sea, stability islands, KAM tori etc). As can be seen in figure 5, the main message is that, due to the highly complicated structure of the mixed phase space, there are several different orbit populations with distinct escape rates, which dominate over different timescales. These few escape rates repeatedly appear as we zoom into the phase space and determine the fractal structure of chaos. The correct definition of γ also requires that we take $t \to \infty$ and take a very large ensemble because there will be fluctuations associated to individual trajectories in an ensemble. This becomes impractical, as it requires evolving very many geodesics for a very long time. We have struck a balance to get an approximate measure of γ.

While the averaged escape rates are more appropriate for trapping and transport calculations, for the understanding of dynamics the escape times $t_{\rm esc}$ (or equivalently non-averaged escape rates γ_0) are more useful. In figure 6 we can visually identify the complex structure of the phase space, in particular the high KS entropy and the remnants of invariant tori (in the zoom-in panel (B)). Linear sections of figure 6, shown in figure 7, make the approximate self-similarity of the phase space particularly obvious.

Finally, we want to check the Pesin relation [28, 30, 31] between the escape rate, the sum of positive Lyapunov exponents and the Kolmogorov-Sinai entropy:

$$\Lambda \equiv \sum_{\lambda_+ > 0} \lambda_+ = h_{\rm KS} + \gamma. \tag{2.16}$$

Besides being a litmus test of developed Hamiltonian chaos, it is also conceptually important as it provides a connection to diffusion and transport, which are naturally related to the black hole membrane paradigm. From the original derivation in [30], the ensemble-averaged escape rate γ is the right one to consider as the derivation starts from a measure of non-escaping orbits in phase space. The numerical check of the $\Lambda - h_{\rm KS} - \gamma$ relation for the disk+ring configuration is found in figure 8.

JHEP02(2026)157

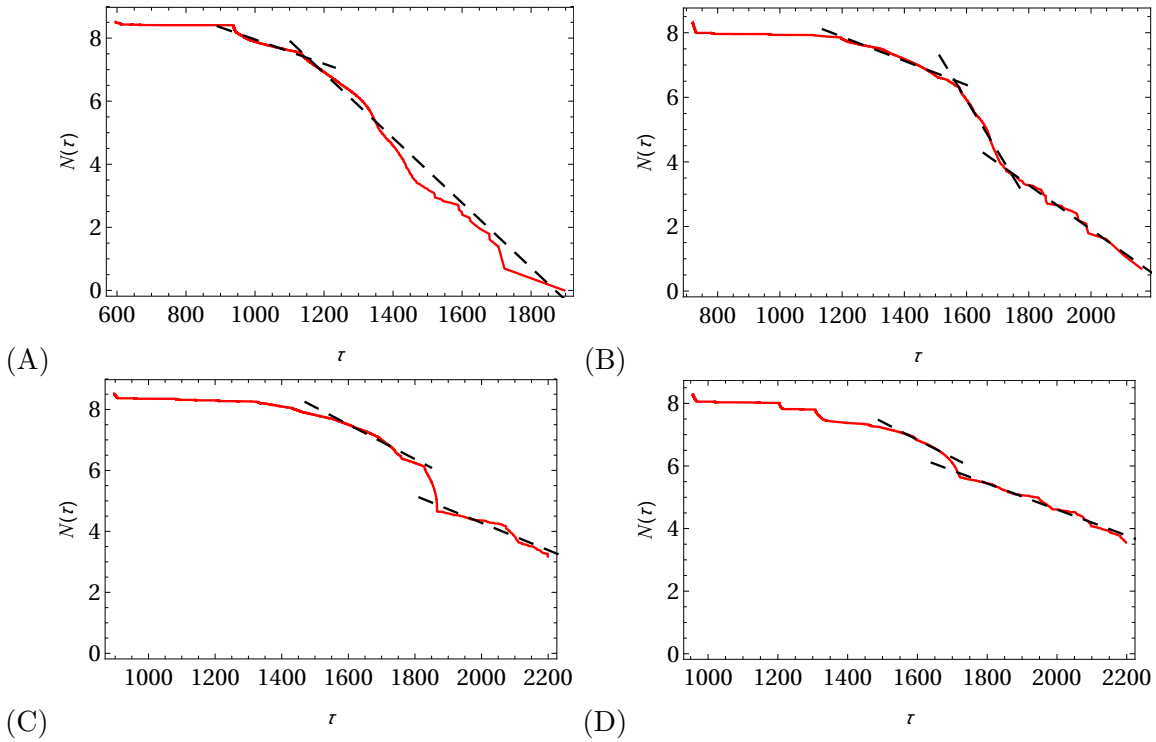

Figure 5. Decay of the number of trapped orbits as a function of proper time $N(\tau)$ (red full lines) for the disk+ring geometry, for four cells of initial conditions of decreasing size, given by $r^{(0)} = 20, P_r^{(0)} = -0.02$, $P_\theta^{(0)} = -0.001$, $\phi^{(0)} = \pi/8$ and $\theta^{(0)}$ from the interval $\theta^{(00)} \pm \Delta\theta$, with $\Delta\theta = 10^{-3}, 10^{-7}, 10^{-8}, 10^{-9}$ (A to D respectively). The black dashed lines yield the best linear fit, the slope defining the escape rate γ from $N(\tau) \sim \exp(-\gamma\tau)$. We detect four distinct populations of orbits, corresponding to the four escape rates on the fits: $\gamma \approx 0.010, 0.0038, 0.0043, 0.0057$.

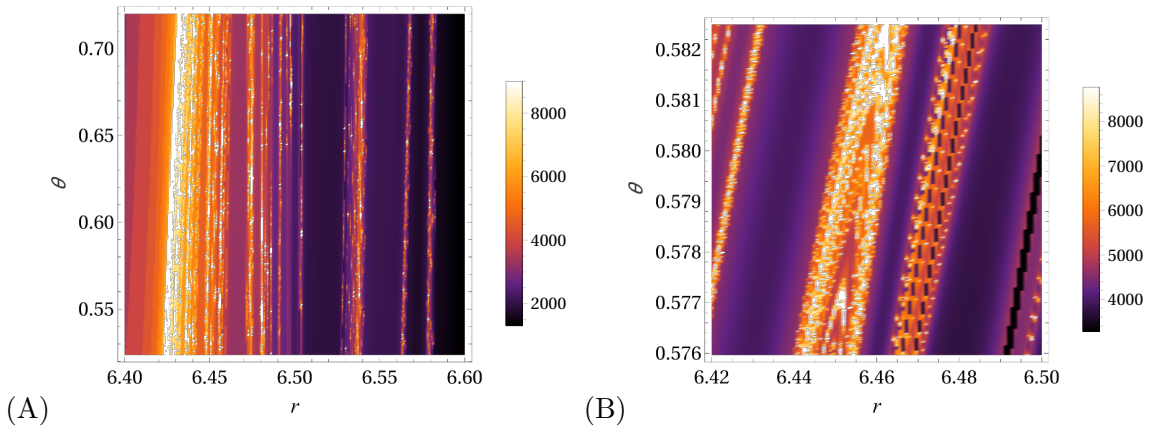

Figure 6. Escape time for a regular grid of initial conditions in (r, θ), with $P_r^{(0)} = -0.001, P_\theta^{(0)} = 0.01$ and integrals of motion $(E, J_-, J_+, P_\phi) = (0.1, 0.01, 0.01, 0.002)$. Every initial condition along r and θ is color-coded for escape time. In (A) we recognize the complex and jagged boundaries of slow- and fast-escape basins, in the zoom-in shown in (B) we recognize the typical shapes of cantori and the remnants of the stability islands. The system shows a typical mixed phase space.

JHEP02(2026)157

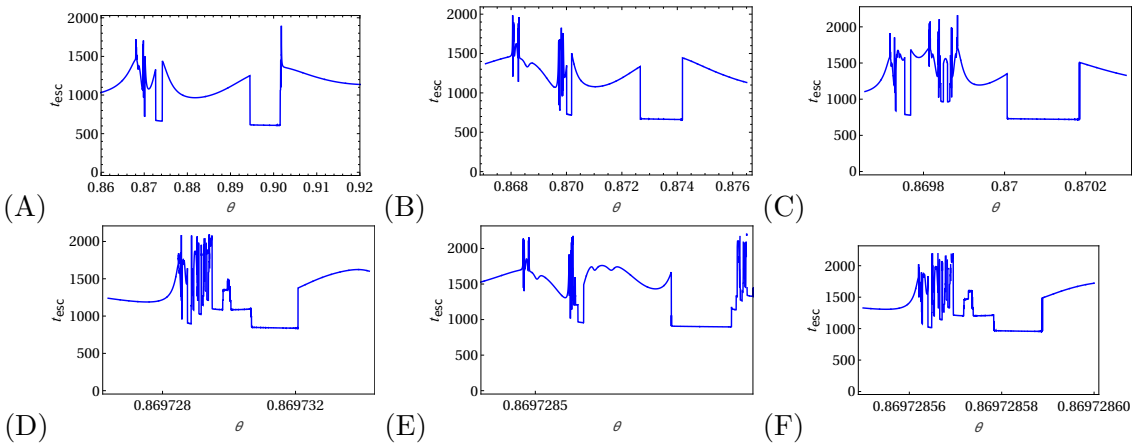

Figure 7. Escape time as a function of the angle θ at six zoom levels, showing approximately self-similar structures. The initial conditions and integrals of motion are the same as in figure 6 (what we show here are thus 1D sections of figure 6).

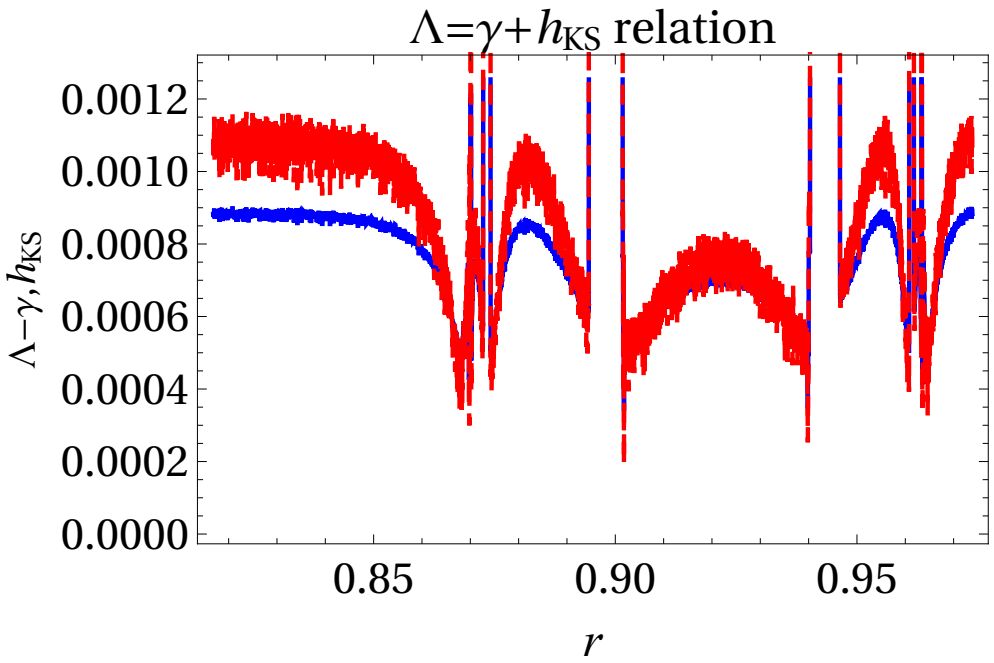

Figure 8. The numerical check of the Pesin relation (2.16) between the KS entropy $h_{\rm KS}$, escape rate γ and the sum of positive Lyapunov exponents Λ, for the disk+ring system. We plot the KS entropy (red) versus the difference $\Lambda - \gamma$ (blue) which is expected to equal the KS entropy. While the fluctuations are large, there is obviously a strong correlation between the two quantities. The calculations are done for the disk+ring system with the initial conditions $r^{(0)} = 20, P_r^{(0)} = -0.02, \theta^{(0)} = 0.275\pi \pm 0.025\pi, P_\theta^{(0)} = -0.001, \phi^{(0)} = \pi/8$ and integrals of motion $(E, J_-, J_+, P_\phi) = (0.1, 0.01, 0.01, 0.002)$.

JHEP02(2026)157

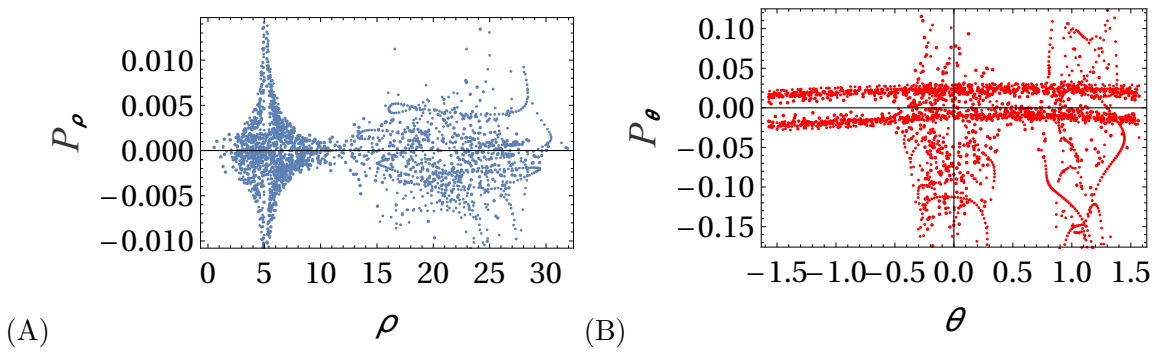

Figure 9. Poincare section $P_\xi = 0$ in $P_\rho - \rho$ and $P_\theta - \theta$ planes for a set of null geodesic orbits in the LLM geometry sourced by the 3-disk pattern in a plane. The chaotic sea is more dominant than for the disk+ring case. Integrals of motion for this set of orbits are $\{J_- = 0.001, J_+ = 0.001, E = 0.02\}$.

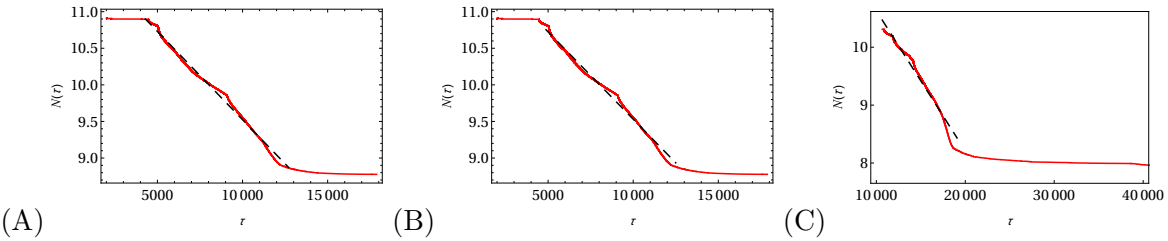

Figure 10. Decay of the number of trapped orbits as a function of proper time $N(\tau)$ (red full lines) for the 3-disk geometry, for three cells of initial conditions of decreasing size, given by $\xi^{(0)} = 4.7, P_\xi^{(0)} = -0.01$, $\phi^{(0)} = \pi/8, P_\phi^{(0)} = 0.002$, $P_r^{(0)} = 0.001$ and $r^{(0)}$ from the interval $r^{(00)} \pm \Delta r$, with $\Delta r = 0.3, 1.0 \times 10^{-9}, 5. - \times 10^{-13}$ (A to C respectively). The black dashed lines yield the best linear fit, the slope defining the escape rate γ from $N(\tau) \sim \exp(-\gamma\tau)$. The 3-disk case generally exhibits stronger chaos, yielding a single, rather universal escape rate $\gamma \approx 0.0023 \pm 0.0002$.

2.3 Multi-disk geometries

Even though the geodesic dynamics is now truly 3-dimensional, with no extra integrals of motion, it is still convenient to transform the Cartesian coordinates in the LLM plane to the polar ones ($x = \rho\cos\phi$, $y = \rho\sin\phi$), while keeping the "altitude" ξ (corresponding essentially to cylindrical coordinates). The Hamiltonian (2.11) for a null geodesic in these coordinates reads:

$$2h^2\,\mathcal{H} = P_\xi^2 + (P_\rho + EV_\rho)^2 + \frac{(P_\phi + EV_\phi)^2}{\rho^2} - h^4\left(E^2 - \frac{2J_-^2}{1-2z} - \frac{2J_+^2}{1+2z}\right). \tag{2.17}$$

We can again look at the Poincare surface of section defined by $P_\xi = 0$. The corresponding sections in $P_\rho - \rho$ and $P_\theta - \theta$ planes are shown in figure 9. In comparison with the disk+ring case it is more chaotic, as expected given the fact that we have one more degree of freedom (i.e. one integral of motion less). Similar conclusions can be gained from the more uniform and universal behavior of the escape rate, shown in figure 10 — now there is only one rate, i.e. only one chaotic component, as the surviving invariant tori do not form barriers in phase space.

The phase space is again mixed, with stability islands and cantori dispersed in the chaotic sea, but we expect this to have less influence on averaging as the phase space dimension is now 6 instead of 5, thus the chaotic orbits have a lower chance to bump into quasiregular structures.

JHEP02(2026)157

3 Null geodesics in grayscale LLM geometries and ensemble averaging

3.1 Grayscale LLM geometries

Grayscale LLM geometries are best understood as coarse-grained LLM solutions [8]. In the matrix model [2], they are obtained from "smoothed" Young tableaux which are only defined up to an order $O(1)$ fluctuation in the number of squares in each row (i.e. where we cannot detect adding/removing $O(1)$ squares); in the supergravity picture they correspond to "smoothed" boundary conditions where the z-functions from eq. (2.4) are allowed to have any value of gray between $-1/2$ and $1/2$:

$$z(\xi \to 0) = b, \quad -1/2 \leq b \leq 1/2. \tag{3.1}$$

This restriction is forced on us by positivity of the metric of the three spheres away from the singularity (one can relate the fact that chronology should be protected to unitarity of the free fermion model and its relation to the Fermi exclusion principle [32]).

Looking at our Hamiltonian (2.12), we notice that the effective potential is given by

$$V_{\text{eff}} = -h^4 \left(E^2 - \frac{2J_-^2}{1-2z} - \frac{2J_+^2}{1+2z} \right), \tag{3.2}$$

and notice that since z is finite as $\xi \to 0$, none of the terms with angular momentum are more divergent near the grayscale LLM plane region than the term that also includes E. The divergence in the potential in this case comes from $h^{-2} \to 0$ as $\xi \to 0$, which does not have a fixed sign. In black and white setups, h is generically finite near $\xi \to 0$ and one of the two terms with angular momentum produces a repulsive force that overwhelms the term with the energy E, so in black and white patterns trajectories are generically repelled when they get sufficiently close to the LLM plane. To make sense of the fact that a grayscale pattern should be thought of as averaging over geometries, this repulsion must be happening on distances that are small relative to the coarse-graining scale.

For a single disk, this gives the solution for z which is exactly the same as for the black disk on white background (eq. (2.6)), but multiplied by g: $z(\xi, x, y, R) \mapsto gz(\xi, x, y, R)$. The generalization for multiple disks is obtained analogously, multiplying each disk solution by the appropriate flux. As we approach the LLM plane $\xi = 0$, the most diverging metric coefficients in any solution with a gray disk scale as $\sim h^2 \sim \sqrt{1/4 - z^2}/\xi$. Therefore, one should expect that the scalar curvature in the LLM plane diverges as violently as ξ^{-3}.

On the other hand, there is still no horizon. We have thus produced a singularity but not a black hole. However, it is a good singularity in the Gubser scheme [33], and one should in principle be able to construct a black hole out of it. Such an object begs the question that is now of utmost importance in quantum gravity: *is the coarse-graining/averaging a fundamental one, i.e. averaging over an ensemble, or is it an effective averaging due to finite resolution, i.e. averaging over small details of a given fixed LLM geometry?* Our central idea is to answer this question in detail for geodesics and their dynamical properties.

The picture that emerges is that when we use a grayscale averaging, the singularity becomes effectively attractive and more similar to a black hole with a tiny horizon, where we would expect similar phenomena. This can also be explained as follows. In the metric (2.1),

JHEP02(2026)157

the function h^{-2} is g_{tt}, the warp factor of the time direction. If $h^{-2} \to 0$, there is a region near the singularity where time is warped very much and it produces a gravitation potential barrier to get out. This warping is typical of near horizon regions, where the horizon is usually characterized by $g_{tt} = 0$ in more conventional setups.

3.2 Geodesics in grayscale geometries

Although no new integrals of motion appear in grayscale, and the system is still nonintegrable, the dynamics is much simpler now. We now have two "attractors": the singularity in addition to infinity, as follows from looking at the effective potential (3.2).[2] Naively, one might think that this would lead to even more complex behavior, but it turns out that most orbits are short and quickly end either at infinity or in the singularity.

Figure 11 presents the variation of escape time with initial conditions analogously to figures 5 and 10. Now the dependence is smooth, without complex structures, and panel (B) additionally shows that sticky orbits are very few and far apart. In figure 12(A) the one-dimensional cut along the r-axis explicitly compares the grayscale geodesics (red) with the black and white ones (blue), again showing that the strongly chaotic region vanishes. In figure 12(B) we delineate the unstable periodic orbit dividing the escaping orbits ($r > r_0$) from those which fall into the singularity ($r < r_0$). This is analogous to the black hole's photon ring, and might be interestingly related to the quasinormal mode spectrum; we postpone this line of thinking for further work. Here, our main point is the simplicity of dynamics: although nonintegrable, it comes closer to the regular behavior of geodesics on most black hole backgrounds.

3.3 Grayscale vs. averaging over black-and-white

3.3.1 On the origin of grayscale geometries

So far we have considered grayscale geometries, but we have not stated their origins. There are a number of approaches that can lead to effectively averaged solutions at the supergravity level. One approach is to start from the free fermion description of half-BPS states [2]: any reasonable wave function for the fermions (i.e., a normalizable state with bounded energies, etc) is a state that might be describable by supergravity solutions that we have considered above. For example, we can consider a fractional quantum Hall state wave function. It is an example of a physically reasonable state, but not a ground state for the free fermion Hamiltonian. Such a wave function is a ground state wave function of a different type of incompressible fluid and one can check that it has constant density on the occupied region of the fermion phase space. It is not easy to describe it in terms of the Young tableaux basis that spans the Hilbert space, but it is one possible wave function of the system that some clever experiment might have prepared for us. In that sense, it is possible to imagine that we can generate a single microstate with different grayscale factors in different regions, where the precise given wave function that generates such a pattern might be very complicated.

[2]Of course, there is no attractor in a Hamiltonian system. However, in Hamiltonian scattering, infinity can be thought of as an attractor (for unbounded orbits), and in our case the singularity is also attractor-like in the sense that an open set of orbits near it cannot get away from it.

JHEP02(2026)157

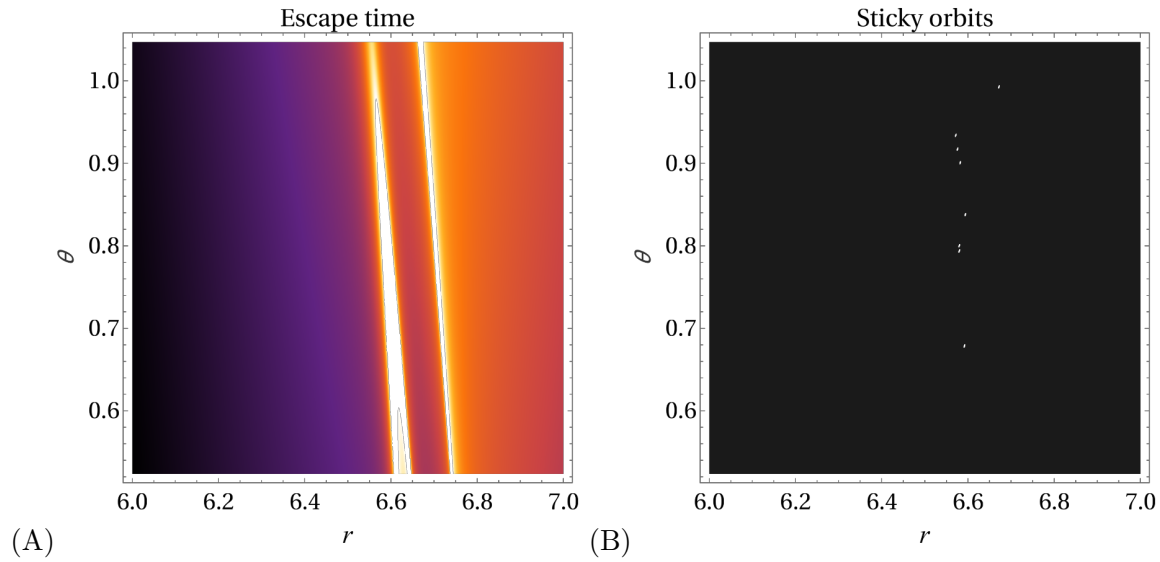

Figure 11. Escape time for a regular grid of initial conditions in (r, θ), with $P_\theta^{(0)} = -0.01, P_r^{(0)} = 0.001$ and integrals of motion $(E, J_-, J_+) = (0.1, 0.01, 0.01)$. In (A) every initial condition is color-coded for escape time — the dependence on initial conditions is smooth and no zooming is necessary as there are no sticky islands or similar complex structures. In (B) we indicate the sticky orbits ($t_{\rm esc}/t_0 > 50000$): there are only very few such orbits (and even these might be numerical artifacts) and we can conclude there is neither stickyness nor developed chaos. The color code in (A) is the same as in figure 5.

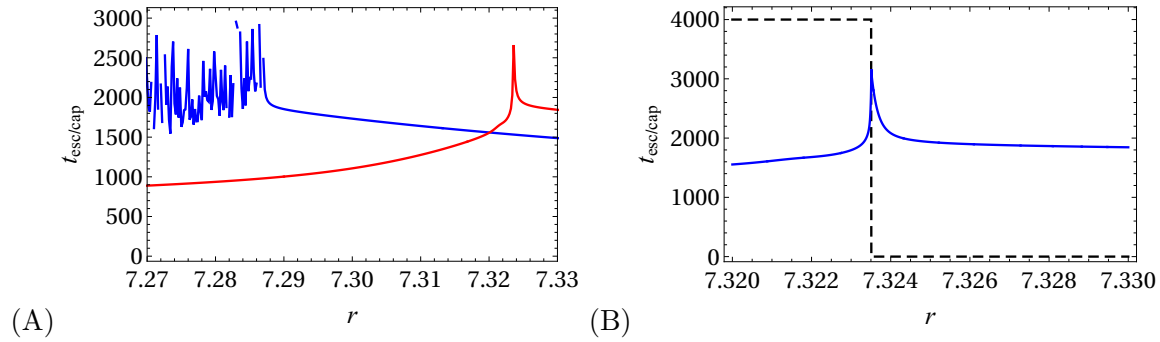

Figure 12. (A) Escape/capture time as a function of r for grayscale disk+ring geometry (red) and for a specimen from an ensemble of $N = 31$ black and white rings (blue). Only the latter shows a complex dependence of the escape time on initial condition, indicative of chaotic scattering: everything is washed out in grayscale. In (B) we show that the critical point in ther grayscale escape/capture time, where the time seemingly diverges, corresponds to the bifurcation between escaping ($r < r_0$) and captured ($r > r_0$) orbits, with $r_0 \approx 7.3235$.

JHEP02(2026)157

A slightly different approach is to consider a non-trivial set of concentric ring geometries with excitations on top of them that are entangled between different edges of the geometry. In [34] it was shown how to explicitly write down such excitations; one can then build an approximate squeezed state between different such excitations that in expectation values produces a grayscale pattern locally. Concerning the local degrees of freedom near the corresponding edge, since they are entangled with other degrees of freedom that are far away, the local physics can be thought of as a generalized ensemble of geometries with thermal-looking modes, with a different temperature for each mode. This would be a version of a generalized Gaussian ensemble for the local degrees of freedom.

Basically, we can justify building a locally preferred grayscale pattern by averaging over some ensemble of choice that can be used to represent these options. We can then ask if the physics of the probes we are considering (the lightlike geodesics) are sensitive to the details. That is, can we distinguish a fundamental grayscale state from a state that is gray just because a very large class of wave functions locally can be thought of as a classical statistical ensemble of geometries near the region we want to study? At the level of our present analysis, the answer is no: the geodesics do not see the wave function, i.e. the microstate, and are solely determined by the geometry, which is the same no matter what is the origin of the coarse-graining. Our goal is then to build a simple model as an example of this idea.

3.3.2 Averaging in a toy model

We will again consider the disk+ring geometry but now the area between the disk and the ring is grayscale, with a value between $-1/2$ and $1/2$. The equations for the metric remain the same as (2.1)–(2.4) except that the boundary conditions (2.5) are replaced by (3.1). This solution can be understood as the coarse-grained sequence of black and white rings with separation less than $\sqrt{\hbar}$, the coarse-graining scale. In order to understand how the averaging works, we will compare the grayscale geometry with a coarse-grained sequence of black and white rings of finite separation, which nevertheless should capture the basic workings of the averaging when the total number of rings is large.

This works at values of ξ, where ξ is strictly non-zero and fixed, as we take the concentric rings to be smaller and smaller. Only then, we are allowed to take the limit $\xi \to 0$. Basically, the coarse-graining procedure requires taking a particular order of limits. Notice that in the ξ variables, the warp factor of the grayscale geometry satisfies $g_{tt} \to 0$ with a single zero at $\xi = 0$, typical of black hole horizons. The metric, restricted to the t, ξ coordinates near this region looks like $-\xi dt^2 + d\xi^2/\xi$, which is a metric of Rindler space in two dimensions and starts looking like a black hole throat near the singularity. Orbits that fall to the $\xi \to 0$ region take a long time to get out because of the warp factor. Essentially, when we integrate the time variable in the geometry relative to ξ we find that the time scales as $t \simeq -\log(\xi)$. This is different than the effective time of the Hamiltonian system we solve, which is an affine parameter of the null geodesic. The region near the singularity is very similar to a near horizon geometry of a black hole and it traps orbits for a long time.

Going back to the averaging procedure, consider a specific model of $2N+1$ concentric rings, where the black disk of radius R_1 is followed by a white ring extending to R_2, followed by a

JHEP02(2026)157

black ring to R_3 and so on, ending with a black ring between R_{2N} and R_{2N+1} (figure 13(A)).[3] For $R_i - R_{i-1}$ small ($2 \leq i \leq 2N$), a grayscale geometry with a gray ring extending from R_1 to R_{2N} (figure 13(B)) should be a good approximation. In order to approximate the gray area, we average over $2N-2$ numbers: R_i with $2 \leq i \leq 2N-1$; R_1, R_{2N} and R_{2N+1} are fixed. The probability density $P(R_2, \ldots R_{2N-2})$ must be normalized:

$$\int dR_2 \ldots \int dR_{2N-2} P(R_2, \ldots R_{2N-2}) = 1 \tag{3.3}$$

and conserve the total flux through the LLM plane. In the language of the matrix model this is the Luttinger theorem (the total number density is conserved). For our concentric circles model this means (it is understood that $R_0 \equiv 0$)

$$\sum_{i=1}^{N} \left(R_{2i+1}^2 - R_{2i}^2 \right) \equiv \frac{\mathcal{A}}{\pi} = R_1^2 + g \left(R_2^2 - R_1^2 \right) + R_3^2 - R_2^2. \tag{3.4}$$

As we have already described, we are justified in using such an ensemble because local classical features can appear to be in a mixed state in the quantum mechanical wave function either because we are considering a true *ensemble* of geometries with similar features, or because local features can *appear* to be mixed since they are entangled with degrees of freedom that are far away. Many such wave functions could lead to the same local ensemble, which is justified by stating that a density matrix in the particular Young diagram basis is built to be (locally) diagonal in that basis as a member of a general class of ensembles with similar properties.

We can also consider a slightly different point of view: take a superposition of different classical ring geometries as a type of Schrödinger cat state. Since classically they are different, any sufficiently reasonable classical measurement would be diagonal in this basis and would lead to a distribution like the one determining P in (3.3), which would be sensitive to the amplitudes of the superposition, but not to the phases of individual states.

Now the average of any observable $O(x(\tau))$ which is a function of a geodesic $x(\tau)$ is obtained as

$$\langle O\left(x\left(\tau\right)\right)\rangle = \prod_{i=2}^{2N-1} dR_i P(R_2, \ldots R_{2N-2}) O(x(\tau)), \tag{3.5}$$

where it is understood that the geodesic $x(\tau)$ implicitly depends on the background and thus on R_i. Ideally, one would like to directly calculate the average of a geodesic length or deflection angle, which are relevant for the calculation of correlation functions in the eikonal approximation. We instead do a simpler and more tractable task: averaging the effective potential felt by the geodesic. This should suffice to give an idea of whether the averaging goes through or not.

3.4 Near-plane effective potential

3.4.1 Black and white vs. gray potential

Even this problem, the analysis of the effective potential, is overall analytically intractable. But the dynamics is largely dominated by bounces off the LLM plane, and in this regime

[3] It is easy to see that the total number of disk and ring boundaries must be odd, hence $2N+1$.

JHEP02(2026)157

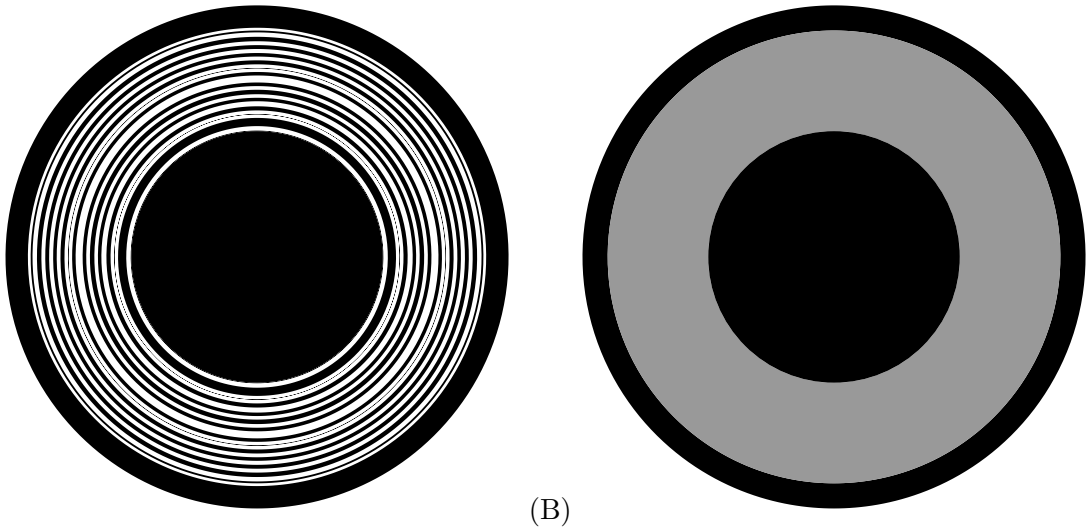

(A) (B)

Figure 13. Geometry with a disk and N thin black rings (A) should be well-approximated by a coarse-grained solution with a single gray ring (B). Our main puzzle, considered in this section, is if this averaging carries over to the geodesic fluctuations.

the effective potential is dominated by the discontinuity at the black-white boundary. This boundary in turn corresponds to the AdS boundary of a given disk (AdS) region, and the effective potential acquires the familiar inverse-square form.

We can show this explicitly by expanding the effective Hamiltonian (2.11) near the LLM plane, i.e. around $\theta = 0$ or $\xi = 0$. Expanding near $\theta = 0$ and the black-white boundary $(\theta = 0, r = R_i)$ and putting $P_r = P_\xi = 0$, we get

$$V_{\text{BW;eff}}(\theta, r) = \frac{J_-^2 \Theta(\rho - R_i) + J_+^2 \Theta(R_i - \rho)}{2r^2\theta^2} + O(\theta^0). \tag{3.6}$$

Doing the same for a gray disk of intensity g with the appropriate metric, we get

$$V_{\text{gray;eff}}(\theta, r) = \frac{J_+^2 + J_-^2 + g\,(J_-^2 - J_+^2)\,\text{sgn}(r^2 - R_i^2) - E^2\frac{1-g^2}{2}}{2r^2\theta^2} + O(\theta^0). \tag{3.7}$$

In the cylindrical ξ coordinate the expressions are analogous:

$$V_{\text{BW;eff}}(\xi, \rho) = \frac{J_-^2 \Theta(\rho - R_i) + J_+^2 \Theta(R_i - \rho)}{\xi^2} \tag{3.8}$$

$$V_{\text{gray;eff}}(\xi, \rho) = \frac{-(\frac{E}{2})^2\,(1 - g^2) + \frac{J_-^2 + J_+^2}{2} + \frac{g}{2}\,(J_-^2 - J_+^2)\,\text{sgn}(\rho - R_i)}{\xi^2} \tag{3.9}$$

Notice the discontinuity at $r = R_i$ which persists also in grayscale. The crucial difference between the black-and-white and gray cases is that, for some interval of g values, the grayscale geometry develops a potential well, corresponding to the fall into the singularity. The black and white potential is always repelling, i.e. positive. The main reason is the behavior of h. For example, in regular LLM geometries the function h remains finite as $\xi \to 0$ (see for example [27]). That is, only one sphere radius shrinks. In the grayscale setup h blows up

JHEP02(2026)157

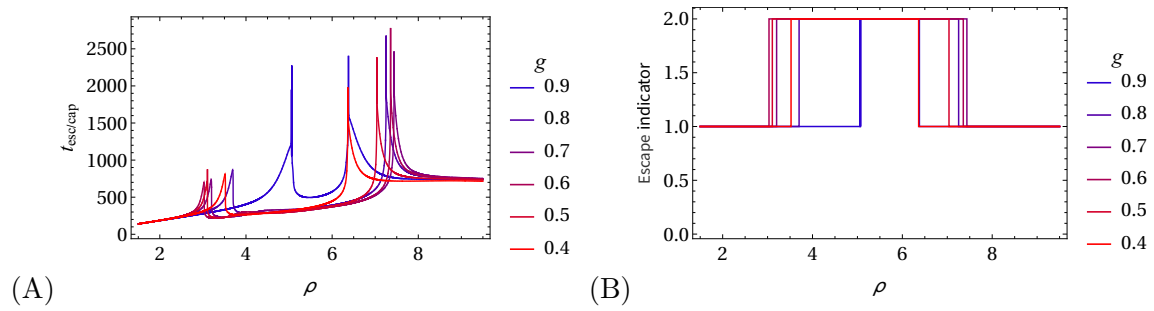

Figure 14. (A) Escape/capture time as a function of r for six grayscale geometries with different fluxes, with initial conditions $\rho^{(0)} = 20, P_\rho^{(0)} = 0.01$ and integrals of motion $(E, J_-, J_+) = (0.1, 0.01, 0.01)$: the time is a smooth function of ρ as already found. (B) Escape indicator for the same setup as in (A): the geodesics escape for 1 or end up in the singularity for 2. For $g < g_- \approx 0.30$ and $g > g_+ \approx 0.90$ all orbits at this energy would end up escaping, because the effective potential becomes strictly positive (i.e., repulsive).

because $z \neq \pm 1/2$. Then, even though this counts as an angular momentum barrier, the contribution of E is of the opposite sign than the contributions from $J_\pm$ and this can produce a strongly attractive potential to the singularity if E is large enough.

This strongly attractive potential means that many orbits cannot wander for a long time but have a simple structure, falling straight into the singularity. That in turn explains the simpler structure of the geodesics and the lack of strongly chaotic orbits. The quantitative criterion for attraction is simply that the effective potential C/ξ^2 has $C < 0$. Equating the coeffficient of eq. (3.9) to zero we get

$$g_\pm = \frac{|J_-^2 - J_+^2| \pm \sqrt{E^4 - 2E^2\left(J_-^2 + J_+^2\right) + \left(J_-^2 - J_+^2\right)^2}}{E^2}. \tag{3.10}$$

The g_+ and g_- solutions correspond to semi-white (positive) and semi-black (negative) values, respectively; for the gray nuances $g_- < g < g_+$ the geodesic falls into the center. These analytical findings are confirmed in figure 14: precisely between the "semi-white" critical value and the "semi-black" critical value the geodesics fall into the LLM plane.

In conclusion, the naked singularity acts as a strong attractor whose domain of attraction is mainly determined by energy. As a result, most orbits of given energy either fall in or escape, and the dynamics is much simpler and more regular compared to the black and white case. Furthermore in the potential C/ξ^2 it takes a finite amount of time in our Hamiltonian system to reach $\xi = 0$. Remember that this is an affine time of the null geodesic and not the time t elapsed in the LLM coordinates that describe the infall. That external time which could be measured by an external observer is actually large.

Notice that a hint of this behavior can be gleaned from figures 1 and 2. There, the null geodesics seem to want to go to the interface between the black and white regions when they are closest to the LLM plane, which is the closest analog of the singularity in smooth solutions.

JHEP02(2026)157

3.4.2 Gray potential as average over black and white

We now reach the core of the matter: are the grayscale orbits well approximated by ensemble averages over black and white? We will now explicitly define the ensembles, and then proceed to do the averaging.

For the whole sequence of $2N+1$ boundaries in a multiring background of figure 13(A) the total black and white potential reads[4]

$$V_{\rm BW}(\xi) = \frac{1}{\xi^2}\sum_{j=1}^{2N+1}(-1)^{j+1}\left[J_-^2\Theta(\rho-R_j)+J_+^2\Theta(R_j-\rho)\right], \tag{3.11}$$

while the grayscale system has the contribution (3.8) for $0<\rho<R_1$ and $R_2<\rho$ and (3.9) for $R_1<\rho<R_2$:

$$\begin{aligned} V_{\rm gray}(\xi) = \frac{1}{\xi^2}\Big[& J_-^2\left(\Theta\left(\rho-R_1\right)+\Theta\left(\rho-R_3\right)\right)+J_+^2\left(\Theta\left(R_1-\rho\right)+\Theta\left(R_3-\rho\right)\right) \\ & -\left(\frac{E}{2}\right)^2\left(1-g^2\right)+\frac{J_-^2+J_+^2}{2}+\frac{g}{2}\left(J_-^2-J_+^2\right)\mathrm{sgn}\left(\rho-R_2\right)\Big] \end{aligned} \tag{3.12}$$

We now want to compare (3.12) to the ensemble-averaged value of (3.11).

In principle, one should quantize the LLM system and average over the fluctuations of the ground state, similar to the procedure for the five-brane stars in [35, 36]. We, however, find this too complicated, and also the global shape of the geodesics should be insensitive to the details of the in-plane black and white pattern, which only influence extremely low-energy behavior. We thus adopt a purely ad hoc Gaussian distribution of $R_2,\dots R_{2N-1}$ (satisfying the constraint (3.4)):

$$P(R_2,\dots R_{2N-2}) = \mathcal{N}e^{-\sum_{j=2}^{2N-1}\frac{(R_j-R_{j;0})^2}{2\sigma^2}}\delta\left(\sum_{j=1}^{2N+1}R_j^2-\frac{\mathcal{A}_0}{\pi}\right) \tag{3.13}$$

where the mean values $R_{i;0}$ are taken to be uniformly spaced:

$$\begin{aligned} R_{j;0} &= R_1+(j-1)\frac{R_{2N}-R_1}{N-2} \\ \mathcal{A}_0 &= \pi\sum_{j=1}^{N}\left(R_{2j}^2-R_{2j-1}^2\right) \end{aligned} \tag{3.14}$$

Now representing the Dirac delta through its Fourier transform the ensemble-averaged potential becomes

$$\begin{aligned} \langle V_{\rm eff}(\xi)\rangle = & \frac{1}{Z}\frac{1}{\xi^2}\prod_{j=2}^{2N-1}\int dR_j\int d\lambda V_{\rm BW;eff}(\xi) \\ & \times\exp\left[-\sum_{j=2}^{2N-1}R_j^2\left(\frac{1}{2\sigma^2}+(-1)^j\imath\lambda\right)+\sum_{j=2}^{2N-1}\frac{R_{j;0}}{\sigma}R_j-\imath\lambda\Sigma_-\right], \end{aligned} \tag{3.15}$$

[4] We adopt cylindrical coordinates as the expressions are simpler.

JHEP02(2026)157

where we have dropped the constant factors as they cancel out with the same factors in the partition function Z, and we have denoted $\Sigma_- \equiv \sum_{j=1}^{2N+1}(-1)^{j+1}R_{j;0}^2$. We can write the above in matrix form as

$$\langle V_{\text{eff}}(\xi)\rangle = \frac{1}{Z}\frac{1}{\xi^2}\prod_{j=2}^{2N-1}\int dR_j \int d\lambda V_{\text{BW;eff}}(\xi)\exp\left[-\mathbf{R}\cdot\hat{\mathbf{M}}\cdot\mathbf{R}-\mathbf{K}\cdot\mathbf{R}-\imath\lambda\Sigma_-\right], \tag{3.16}$$

where the vector $\mathbf{R}\equiv(R_2,\dots R_{2N-1})$ contains the random ring radii and the $(2N-2)\times(2N-2)$ matrix $\hat{\mathbf{M}}$ and the $(2N-2)$-vector $\mathbf{K}$ read

$$\hat{\mathbf{M}} = \text{diag}\left(\frac{1}{2\sigma^2}+(-1)^j\imath\lambda\right), \quad \mathbf{K}=\left(\frac{R_{j;0}}{\sigma}\right), \quad j=2,\dots 2N-1. \tag{3.17}$$

Inserting the expression (3.8) into (3.16) we see that the step functions just modify the limits of the R_j-integrals as

$$\int dR_j\int_0^\infty d'\mathbf{R}\mapsto\sum_{j=2}^{2N-1}\left(J_-^2\int_0^\rho dR_j+J_+^2\int_\rho^\infty dR_j\right)\int_0^\infty d'\mathbf{R}, \tag{3.18}$$

where $\int d'\mathbf{R}\equiv\prod_{k\neq j}\int dR_k$ and in general $\mathbf{R}'=(R)_{k,k\neq j}$. This yields

$$\begin{aligned}\langle V_{\text{eff}}(\xi)\rangle = \frac{1}{Z}\sum_{j=2}^{2N-1}\int d\lambda\Bigg[&\frac{J_-^2}{\xi^2}\int_0^\rho dR_j\int_0^\infty d'\mathbf{R}e^{-R_j^2\left(\frac{1}{2\sigma^2}-\imath\lambda\right)-\frac{R_{j;0}R_j}{\sigma}}e^{-\mathbf{R}'\cdot\hat{\mathbf{M}}'\cdot\mathbf{R}'-\mathbf{K}'\cdot\mathbf{R}'}\\ &-\frac{J_+^2}{\xi^2}\int_\rho^\infty dR_j\int_0^\infty d'\mathbf{R}e^{-R_j^2\left(\frac{1}{2\sigma^2}-\imath\lambda\right)-\frac{R_{j;0}R_j}{\sigma}}e^{-\mathbf{R}'\cdot\hat{\mathbf{M}}'\cdot\mathbf{R}'-\mathbf{K}'\cdot\mathbf{R}'}\Bigg]e^{-\imath\lambda\Sigma_-},\end{aligned} \tag{3.19}$$

where, analogously to the definition of $\mathbf{R}'$, we have $\mathbf{K}'=(K_k)_{k\neq j}$ and $\mathbf{M}'=(M_{kl})_{k,l\neq j}$. Performing the integrals yields

$$\begin{aligned}\langle V_{\text{eff}}(\xi)\rangle = \frac{1}{Z}\frac{\sqrt{\pi}}{2\xi^2}\int d\lambda\sum_{j=2}^{2N-1}\frac{(-1)^{j+1}}{\sqrt{M_{(-1)^j}}}e^{-\frac{R_{j;0}^2}{4\sigma^2M_{(-1)^j}}} \\ \times\left[\left(J_-^2-J_+^2\right)\text{Erf}\left(\frac{R_{j;0}+2\sigma M_{(-1)^j}\rho}{2\sigma\sqrt{M_{(-1)^j}}}\right)+J_+^2-J_-^2\ \text{Erf}\left(\frac{R_{j;0}}{2\sigma\sqrt{M_{(-1)^j}}}\right)\right]e^{-\imath\lambda\Sigma_-}Z_{2N-3;j}.\end{aligned} \tag{3.20}$$

Here, Erf is the error function and $Z_{2N-3;j}$ is the partition function for $2N-3$ disks with radii R_k with $k\neq 1,j,2N,2N+1$; we can also denote $Z_{2N-2}\equiv Z$. The partition function is written out as

$$Z=Z_{2N-2}=\frac{\pi^{N-1}}{(M_+M_-)^{\frac{N-1}{2}}}\prod_{j=2}^{2N-1}e^{\frac{R_{j;0}^2}{4\sigma^2M_{(-1)^j}}}\left[1-\text{Erf}\left(\frac{R_{j;0}}{2\sigma\sqrt{M_{(-1)^j}}}\right)\right] \tag{3.21}$$

$$Z_{2N-3;j}=\frac{\pi^{N-1/2}}{(M_+M_-)^{\frac{N-2}{2}}M_{(-1)^k}^{1/2}}\prod_{k\neq j}e^{\frac{R_{k;0}^2}{4\sigma^2M_{(-1)^k}}}\left[1-\text{Erf}\left(\frac{R_{k;0}}{2\sigma\sqrt{M_\pm}}\right)\right]. \tag{3.22}$$

Noticing that

$$Z_{2N-3;j}=\prod_{k\neq j}Z_{1;(k)},\quad Z_{1;(k)}=\sqrt{\frac{\pi}{M_{(-1)^k}}}e^{\frac{R_{k;0}^2}{4\sigma^2M_\pm}}\left[1-\text{Erf}\left(\frac{R_{k;0}}{2\sigma\sqrt{M_\pm}}\right)\right] \tag{3.23}$$

JHEP02(2026)157

we get

$$\langle V_{\rm eff}(\xi)\rangle = \frac{1}{2\xi^2}\int d\lambda e^{-\imath\lambda\Sigma_-}\sum_{j=2}^{2N-1}\frac{A_j}{Z_{1;(j)}} \tag{3.24}$$

$$\frac{A_j}{Z_{1;(j)}} = \frac{(J_-^2+J_+^2)\,\mathrm{Erf}\left(x_j+\rho\sqrt{M_{(-1)^j}}\right)+(J_+^2-J_-^2)\,\mathrm{Erf}(x_j)}{1-\mathrm{Erf}(x_j)} \tag{3.25}$$

$$x_j \equiv \frac{R_{j;0}}{2\sigma\sqrt{M_{(-1)^j}}}. \tag{3.26}$$

Now the remaining steps are the λ-integral and the coarse-graining. We do the integral in the saddle-point approximation, solving for the zeros off the integrand in (3.24), which can only be done numerically (recall that x_j depends on λ through $M_{(-1)^j}$ so the λ-derivative of the integrand is quite involved).

There is an infinite series of zeros; however, since λ is really the Fourier conjugate variable of R and R is confined between R_1 and R_{2N} it follows that λ is periodic with period $2\pi/(R_{2N}-R_1)$; as usual, the saddle points outside the first Brillouin zone merely introduce a phase shift that cancels out. Calculating the residue and evaluating the integral we find a closed-form expression but very complicated and nonintuitive. We give it in appendix C.

The plots of the black and white, grayscale and ensemble-averaged potential as a function of r,θ[5] in figure 15 reveal that the average introduces the potential well of the naked grayscale singularity when there are many rings to coarse-grain over (panel B). If we only average the position of a single disk (panel A), the average does not have true bound (negative energy) states.

Still, even in the single-disk case there is one important effect: the potential barrier, i.e. the strength of the repelling potential, is reduced (even though it remains positive, i.e. repelling). This effect will push the orbits toward grayscale behavior, *on timescales which are not too long*, in fact shorter than the trapping timescale. In other words, precisely because of the repelling nature of the potential exactly at $\xi=0$, where the black/white pattern is strict, most geodesics cannot come very close to the LLM plane and for that reason do not differentiate much between grayscale and averaged black and white as far as motion in the ξ direction is concerned. When many disks are present, the total effect is larger and we end up with a very good approximation of the grayscale potential, at just the right nuance for this numerical example $g=5/9$.

Finally, we note that conceptually similar result is obtained if we assume a uniform distribution of ring radii, as shown in appendix D. This is less justified as an approximation to actual fluctuations of the background (Gaussian distribution being favored by the usual central limit theorem arguments) but the final result confirms the robustness of the averaging picture.

Another way to think about the universality of these behaviors is that the function z which appears in all these geometries satisfies an elliptic PDE and is similar to a solution of the Laplace equation with fixed (Dirichlet) boundary conditions. The Laplace equation smoothes

[5]Even though the expressions for a single disk are much simpler in polar coordinates, the integration is easier to do in spherical coordinates. This fact and the fact that cylindrical coordinates are not convenient for the 3-disk case have prompted us to use spherical coordinates.

JHEP02(2026)157

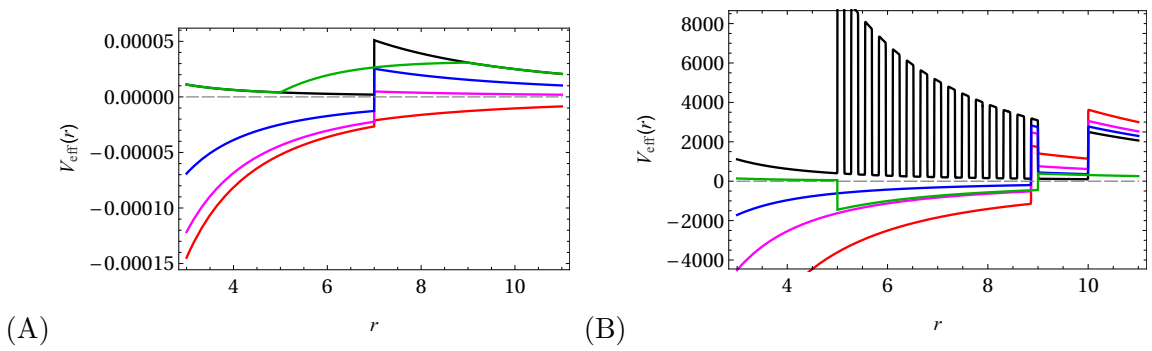

Figure 15. (A) Near-plane effective potential $V_{\text{eff}}(r;\theta \mapsto 0)$ for a single black disk (black), single gray disk with decreasing flux $g = 7/9, 5/9, 1/9$ (blue, magenta, red) and for the average over the size of the black disk (green). The integrals of motion are $(E, J_-, J_+, P_\phi) = (0.1, 0.05, 0.01, 0.1)$. For a single disk the averaging does not mimic the grayscale geometry, i.e. does not create a potential well (though it does create metastable bound states). (B) Same as in (A) for disk+rings configuration with $2N + 1 = 31$ rings. The averaged (green) curve now provides a good approximation of the grayscale potential with appropriate nuance $g = 5/9$ (magenta). In particular, bound states and falling into the center are reproduced.

configurations rapidly away from the boundary, so the precise details of the structure that is exactly at the boundary becomes unimportant when we are some distance away. Also, notice that in all the black and white solutions the function h grows as we try to reach a black and white interface. That is because in this region z is farther away from $\pm 1/2$ as we approach the LLM plane. This provides a reason for the wells to be forming, even though it is not obvious.

3.5 Averaged trajectories

One could argue that an orbit *in averaged effective potential* is not equivalent to an *averaged orbit* itself, i.e. that averaging and solving the equations of motion do not commute. This is certainly true in the rigorous sense, however numerical integrations show that orbits in averaged potentials make a very good approximation of the orbit averages *up to some timescale*.

In figure 16 we compare the orbit in the averaged potential to the orbits in different grayscale backgrounds. For reference, we also include the phase space average, i.e. the average from different initial conditions in a fixed black and white background. The grayscale orbit approximates the ensemble average very well, precisely for the flux that equals the total flux in the black and white ensemble, which further confirms that the averaging works as expected. But this is true for early enough times, i.e. roughly until some crossover time t_c. For $t > t_c$ the agreement is nonexistent as the grayscale orbits end up in the singularity or at infinity — in other words, either $t_{\text{esc}} \sim t_c$ or $t_{\text{fall}} \sim t_c$, whereas for the black and white backgrounds t_{esc} is much longer as we have seen earlier, and there is no singularity ($t_{\text{fall}} = 0$). This is in agreement with the general intuition that self-averaging works at short times. Finally, the fact the phase-space averaging is nearly equivalent to ensemble averaging of backgrounds shows that both kinds of averaging crucially depend on dynamical chaos: phase space averaging is always a signature of developed chaos (which again only works on timescales short enough that most orbits do not explore the remnants of KAM tori).

JHEP02(2026)157

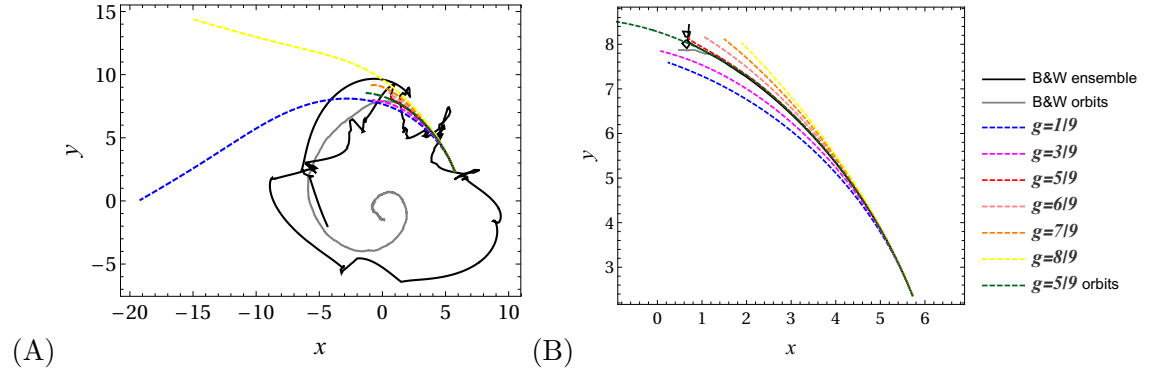

Figure 16. Black and white orbits averaged over the ensemble (black) or over the initial conditions (gray), compared to the grayscale orbits, including the one with the correct averaged flux (green, $g = 5/9$), which indeed shows near-perfect self-averaging for short times.

3.6 Grayscale and averaging in 3-disk geometries

It is instructive to apply the same tests on averaging and grayscale geometries to the 3-disk solution. We envision the following setup: one of the disks is a configuration of $2N + 1$ rings of radii $0 < R_1 < \dots R_{2N} < R_{2N+1}$ with fixed outer radius $R_{2N+1} = \text{const.}$ and fixed total flux $\mathcal{A}$. The remaining two disks remain fully black, with radii R_{2N+1}, and their centers are located at the same points as in figure 2. Now we go through the same numerical tests: we integrate geodesics on ensembles of fixed disks+rings backgrounds, then replace the $2N + 1$-ring disk by a gray disk with the same flux and position (but necessarily different radius), and compare the distribution functions and orbits.

Averaged orbits (see appendix B) show the same general picture as before, but now the self-averaging timescale is much longer. The reason is easy to trace to the absence of the extra integral of motion and thus lesser sensitivity of the system to quasiregular structures.

It is tempting to conclude that the picture of a black hole as an average over microstates applies better to the 3-disk solution than to the disk+rings solution. However, the latter is much easier to interpret and much closer to an AdS black hole metric, whereas the former is a rather exotic, anisotropic configuration.[6] This either means that the averaging we have found in the paper is nevertheless not closely related to black holes, or that quantum corrections would further reduce the measure of stability islands and sticky orbits and increase the averaging time also for the disk+ring configuration.

4 Discussion and conclusions

We have embarked on this work hoping to achieve a coherent picture of how ensemble averaging works in higher-dimensional ($D > 3$) gravity, and to understand if superpositions

[6]Both have the same topology and the same boundary $\mathbb{R} \times \mathbb{S}^3$, as both have a final area of black regions and thus a zero total fraction of black regions in the LLM plane; in the classification of [4], this is the $\langle z \rangle = 1/2$ case, as opposed to $\langle z \rangle < 1/2$ geometries which have a lightlike boundary. But in our case it is not only the topology that is important, so the fact that the 3-disk and disk+ring solutions belong to the same class might not matter much.

JHEP02(2026)157

or coarse-graining of supersymmetric top-down solutions can approach the phenomenology of black holes.

Our main tool and paradigm is the study of null geodesics in these backgrounds and their chaotic dynamics: we know that black holes are dual to maximally chaotic field theories, and that they nearly always have integrable geodesic dynamics — both facts stemming from the near-horizon and inner-region $SL(2,\mathbb{R})$ symmetries. Our analysis shows that black holes are but one extreme in the hierarchy: black holes $\rightarrow$ "incipient black holes" (naked singularities with no horizon but good in the Gubser sense) $\rightarrow$ smooth microstate geometries. Black holes mostly have trivial geodesic dynamics, grayscale solutions are nonintegrable but still show only weak chaos as most orbits are swallowed by the singularity before they develop chaos, and in smooth black and white geometries there is developed geodesic chaos and complex phase space with fractal structure. Therefore, presumably, the less chaotic bulk, so long as it has a singularity or a horizon, the more chaotic the dual field theory.

Averaging over black and white backgrounds produces effective potentials with potential wells, which mimic the singularity in grayscale. This is somewhat counterintuitive — the potential itself is obviously a highly non-self-averaging quantity as we average over potentials with no obvious deep wells and get a deep well as a result. It turned out that this idea of no deep wells is closer to failure exactly at the interfaces of black and white regions. When we have a grayscale geometry, these interfaces are populating the whole of the LLM plane and dominate the details of the geometry. But that precisely makes the orbits themselves very much self-averaging, at least at not too long timescales. This is an explicit example where averaging over backgrounds in higher-dimensional gravity brings us closer to black hole dynamics. We also found out that the time-time component of the metric vanishes in these singular solutions, so the averaged singularity is almost a horizon and the dynamics of infalling geodesics freezes near the singularity as viewed by an external observer.

Much remains to be done. First, the averaging over backgrounds that we perform is just phenomenological — in fact one should integrate over the actual quantum fluctuations of LLM geometries. Second, it might make sense to look at non-asymptotically-AdS LLM patterns, as the AdS boundary acts as a potential box itself and influences the long time dynamics of the system. Third, one should understand the role of unstable periodic orbits, their behavior under averaging and if LLM solutions have an analog notion to a photon ring. Finally, the fractal structure of the bulk can tell us something about the behavior of the correlation functions in the eikonal approximation. We will address the last two points in separate works.

Acknowledgments

We are grateful to Andrei Parnachev, Jorge Russo, Yoav Zigdon and Anayeli Ramirez for stimulating discussions. D.B. work supported in part by the Department of Energy under grant DE-SC 0011702. DB is also supported in part by the Delta ITP consortium, a program of the Netherlands Organisation for Scientific Research (NWO) funded by the Dutch Ministry of Education, Culture and Science (OCW) for the early portions of this work. Work at the Institute of Physics is funded by the Ministry of Education, Science and Technological Development and by the Science Fund of the Republic of Serbia. The work on sections 1, 2 and 3.3–3.4 was supported by Russian Science Foundation Grant

JHEP02(2026)157

No. 24-72-10061 [https://rscf.ru/project/24-72-10061/] and performed at Steklov Mathematical Institute of Russian Academy of Sciences (Mihailo Čubrović).

A Numerical calculation of the maximal Lyapunov exponent

We will here present a method for numerical computation of the maximal Lyapunov exponent. More detailed elaboration can be found in [37]. For a given solution to the Hamiltonian system $\vec{\mathcal{X}}(t)$ we can define a deviation vector $\delta\vec{\mathcal{X}}(t)$ that is a solution to the variational equations. We extract the maximal Lyapunov exponent by taking the following limit

$$\lambda_1 = \lim_{t\to\infty} \frac{1}{t} \log \frac{|\delta\vec{\mathcal{X}}(t)|}{|\delta\vec{\mathcal{X}}(0)|}. \tag{A.1}$$

This procedure may be difficult to implement due to limited memory resources, since $|\delta\vec{\mathcal{X}}(t)|$ can take very large values that are difficult to store on the computer. In such a situation one implements the following trick

$$\log \frac{|\delta\vec{\mathcal{X}}(N\Delta t)|}{|\delta\vec{\mathcal{X}}(0)|} = \log \left(\frac{|\delta\vec{\mathcal{X}}(N\Delta t)|}{|\delta\vec{\mathcal{X}}((N-1)\Delta t))|} \cdot \frac{|\delta\vec{\mathcal{X}}((N-1)\Delta t))|}{|\delta\vec{\mathcal{X}}((N-2)\Delta t))|} \cdots \frac{|\delta\vec{\mathcal{X}}(\Delta t)|}{|\delta\vec{\mathcal{X}}(0)|} \right), \tag{A.2}$$

where $t = N\Delta t$. Therefore, instead of solving the variational equations once on the interval $t \in [0,\ t]$, one solves it N times on a sequence of much smaller intervals $t \in [(k-1)\ \Delta t,\ k\ \Delta t]$, $k = 1, 2, \cdots, N$. From eq. (A.2) it is then obvious that the total value of the maximal Lyapunov exponent is related to a sum of the following sequence

$$\log \frac{|\delta\vec{\mathcal{X}}(t)|}{|\delta\vec{\mathcal{X}}(0)|} = \sum_{k=1}^{N} \log \frac{|\delta\vec{\mathcal{X}}(k\Delta t)|}{|\delta\vec{\mathcal{X}}((k-1)\Delta t))|}. \tag{A.3}$$

A follow-up question is related to how fast such a sequence will converge towards the maximal Laypunov exponent value as we vary the number of steps N. Suppose that we calculate the maximal Lyapunov exponent as a sequence labeled by a number of steps N_i: $\lambda_1(N_i)$. In order to extract the limiting value of such a sequence in a computationally efficient way, methods to improve the convergence, such as the Richardson extrapolation [38], can be used.

B Escape time, Pesin relation and fractal structure for the 3-disk system

As we have commented in section 2, the 3-disk system lacks the extra integral of motion of the disk+ring system, and thus has a higher relative measure of the chaotic component in the phase space. We have seen that this makes it more self-averaging then the simpler disk+ring system. But in terms of purely dynamic (as opposed to statistical) quantities, the phenomenology is similar. In this appendix we show the figures analogous to figures 17–19 for the disk+ring system and find an overall similar story.

We see this first in figure 17, showing the escape rate at three levels of magnification (panels A-C), revealing the self-similar stability island structures. In panel (D) the sticky orbits (with very long escape times) are indicated, delineating the remnants of KAM tori.

Numerical check of the $\Lambda - h_{\mathrm{KS}} - \gamma$ relation for the 3-disk configuration is found in figure 18.

JHEP02(2026)157

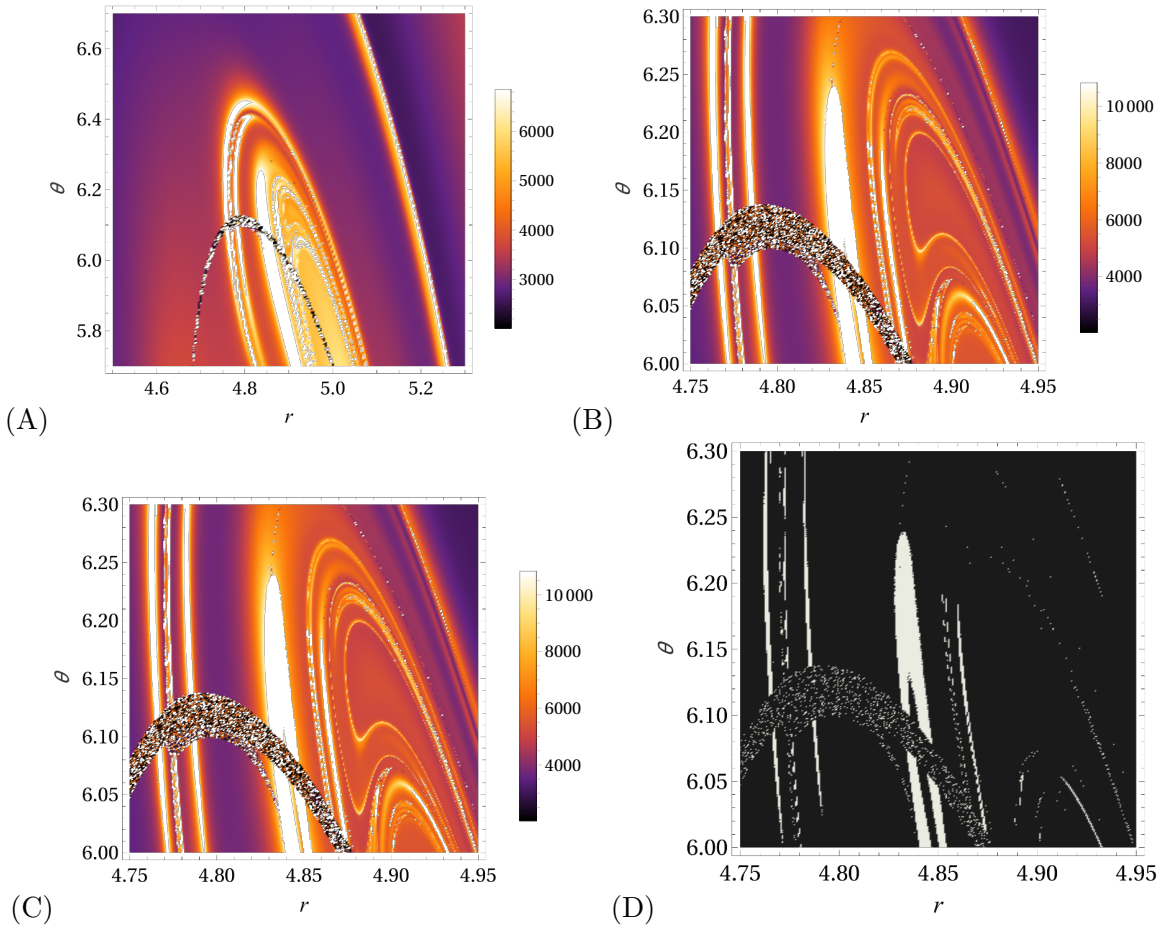

Figure 17. Escape time for a regular grid of initial conditions in (ρ, θ), with $P_\xi^{(0)} = -0.01, P_\rho^{(0)} = 0.001$ and integrals of motion $(E, J_-, J_+) = (0.1, 0.01, 0.01)$. In (A-C) every initial condition along ξ and r is color-coded for escape time, at three levels of magnification. In (D) we indicate the sticky orbits $(t_{\rm esc}/t_0 > 50000)$ at the same zoom level as in (B): these are the orbits with very long escape times in the vicinity of the remnants of KAM tori.

The details of the fractal structure can be reproduced analytically to some extent, and they are related in an interesting way to the structure of two-point functions. However, this is a complex question in its own right and we address it in a separate work. Here, we just want to emphasize the typical structure of mixed chaotic-regular phase space found in LLM geodesics.

JHEP02(2026)157

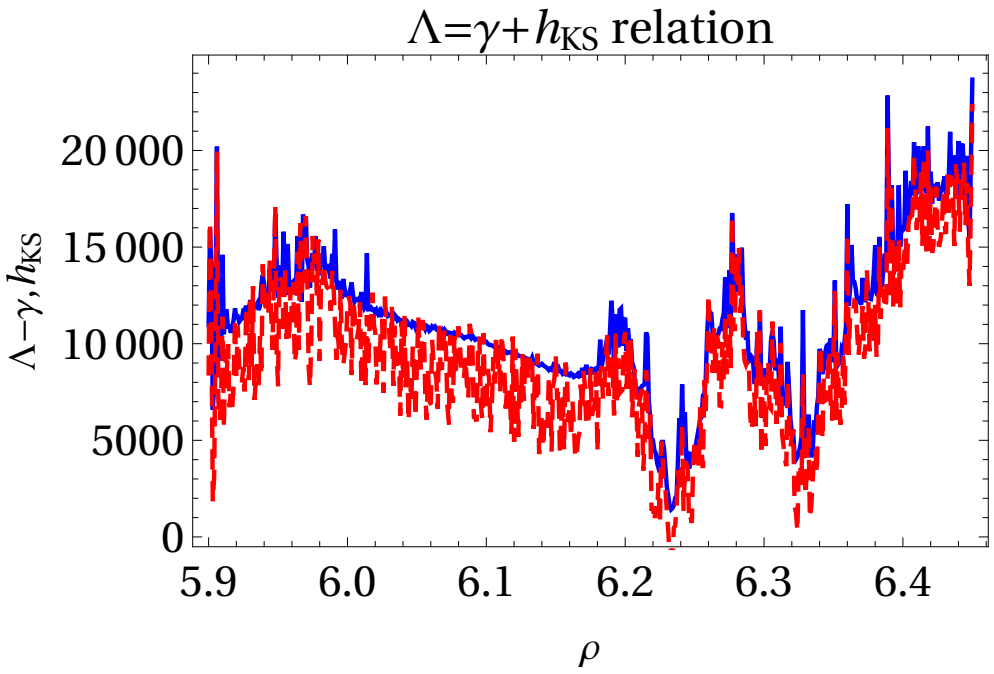

Figure 18. The numerical check of the Pesin relation (2.16) between the KS entropy $h_{\rm KS}$, escape rate $\bar{\gamma}$ and the sum of positive Lyapunov exponents Λ, for the 3-disk configuration. We plot the KS entropy (red) versus the difference $\Lambda - \bar{\gamma}$ (blue) which is expected to equal the KS entropy. While the fluctuations are large, there is obviously a strong correlation. The calculations are done for the 3-disk system with the initial conditions $\xi^{(0)} = 4.7, P_\xi^{(0)} = -0.01, \rho^{(0)} = 6.15 \pm 0.20, P_\rho^{(0)} = 0.0010 \pm 0.0001, \phi^{(0)} = \pi/8$ and integrals of motion $(E, J_-, J_+, P_\phi) = (0.1, 0.01, 0.01, 0.002)$.

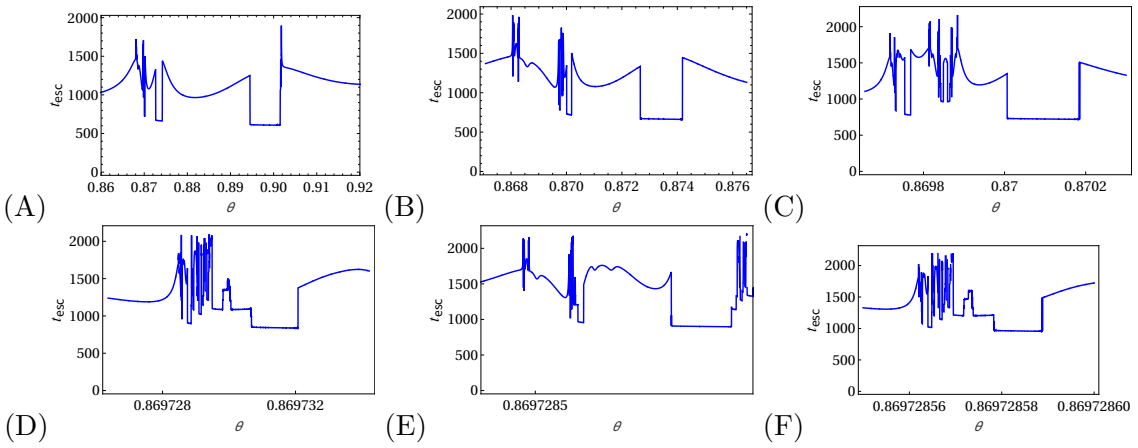

Figure 19. Escape time as a function of the angle θ at six zoom levels, showing approximately self-similar structures. The initial conditions and integrals of motion are the same as in figure 17 (what we show here are thus 1D sections of figure 17).

JHEP02(2026)157

C Explicit expression for the averaged potential with Gaussian fluctuations

As we mention in the main text, closed-form expression for the integral exists but it is too long and nonilllustrative. We give it here for completeness.

$$
\begin{aligned}
V_{\text{eff}}(r,\theta) = {} & 6r\tanh^{-1}\left(\frac{R_1}{r}\right)\left(J_-^2-J_+^2+4EP_\phi\right)-6r\tanh^{-1}\left(\frac{R_{2N+1}}{r}\right)\left(J_-^2-J_+^2+4EP_\phi\right) \\
& +\frac{(R_1-R_{2N+1})\left(2J_+^2\left((\theta^2-6)r^4+\left(3R_1R_{2N+1}\theta^2+2(\theta^2+3)R_1^2+2(\theta^2+3)R_{2N+1}^2\right)r^2\right)\right)}{12r^2\theta^2(r^2-R_1^2)\left(r^2-R_{2N+1}^2\right)} \\
& -\frac{(R_1-R_{2N+1})\left(2(\theta^2+3)R_1^2R_{2N+1}^2-3\theta^2(r^2-R_1^2)\left(r^2-R_{2N+1}^2\right)E^2\right)}{12r^2\theta^2(r^2-R_1^2)\left(r^2-R_{2N+1}^2\right)} \\
& -\frac{3\theta^2\left(4P_\phi(r^2-R_1^2)\left(r^2-R_{2N+1}^2\right)E+2J_-^2(r^4+R_1R_{2N+1}r^2)+4P_\phi^2(r^2-R_1^2)\left(r^2-R_{2N+1}^2\right)\right)}{12r^2\theta^2(r^2-R_1^2)\left(r^2-R_{2N+1}^2\right)} \\
& r<R_1
\end{aligned}
\tag{C.1}
$$

$$
\begin{aligned}
V_{\text{eff}}(r,\theta) = {} & \frac{12R_1(\Im(J_-)-i\Re(J_-))^2}{\theta^2}-6r\tanh^{-1}\left(\frac{R_1}{r}\right)\left(J_-^2-J_+^2+4EP_\phi\right) \\
& +\frac{2R_1\left(-(2r^2+R_1^2)J_-^2+6EP_\phi(R_1^2-r^2)+J_+^2(2r^2+R_1^2)\right)}{R_1^2-r^2}+\frac{12J_+^2R_{2N+1}}{\theta^2} \\
& +\left(3(R_1-R_{2N+1})E^2-12P_\phi R_{2N+1}E+6r\tanh^{-1}\left(\frac{R_{2N+1}}{r}\right)\left(J_-^2-J_+^2+4EP_\phi\right)\right) \\
& +\frac{2\left(r^2(R_1-3R_{2N+1})-R_1R_{2N+1}^2\right)J_-^2+12P_\phi^2(R_1-R_{2N+1})\left(r^2-R_{2N+1}^2\right)}{r^2-R_{2N+1}^2} \\
& +\frac{2J_+^2\left(r^2(R_1+R_{2N+1})+R_{2N+1}^2(2R_{2N+1}-R_1)\right)}{r^2-R_{2N+1}^2} \\
& R_1<r<R_{2N+1}
\end{aligned}
\tag{C.2}
$$

$$
\begin{aligned}
V_{\text{eff}}(r,\theta) = {} & -6r\tanh^{-1}\left(\frac{R_1}{r}\right)\left(J_-^2-J_+^2+4EP_\phi\right)+6r\tanh^{-1}\left(\frac{R_{2N+1}}{r}\right)\left(J_-^2-J_+^2+4EP_\phi\right) \\
& +\frac{(R_1-R_{2N+1})\left(2J_-^2\left((\theta^2-6)r^4+\left(3R_1R_{2N+1}\theta^2+2(\theta^2+3)R_1^2+2(\theta^2+3)R_{2N+1}^2\right)r^2\right)\right)}{12r^2\theta^2(r^2-R_1^2)\left(r^2-R_{2N+1}^2\right)} \\
& -\frac{(R_1-R_{2N+1})\left(\left(2(\theta^2+3)R_1^2R_{2N+1}^2\right)-3\theta^2\left((r^2-R_1^2)\left(r^2-R_{2N+1}^2\right)E^2\right)\right)}{12r^2\theta^2(r^2-R_1^2)\left(r^2-R_{2N+1}^2\right)} \\
& -\frac{3\theta^2\left(4P_\phi(r^2-R_1^2)\left(r^2-R_{2N+1}^2\right)E+2J_+^2(r^4+R_1R_{2N+1}r^2)+4P_\phi^2(r^2-R_1^2)\left(r^2-R_{2N+1}^2\right)\right)}{12r^2\theta^2(r^2-R_1^2)\left(r^2-R_{2N+1}^2\right)} \\
& r>R_{2N+1}.
\end{aligned}
\tag{C.3}
$$

JHEP02(2026)157

D Averaging over black and white regions with a uniform distribution

We will now repeat the averaging procedure for the effective potential from eqs. (3.13)–(3.26) for a uniform distribution of the radii $R_{j;0}$, with $R_j \in [R_{j;0} - \Delta, R_{j;0} + \Delta]$. The probability distribution of the radii is then

$$P(R_2, \dots R_{2N-2}) = \mathcal{N} \prod_{j=2}^{2N-1} \Theta\left(R_j - R_{j;0} + \Delta\right) \Theta\left(R_{j;0} + \Delta - R_j\right) \delta\left(\sum_{j=1}^{2N+1} R_j^2 - \frac{\mathcal{A}_0}{\pi}\right). \tag{D.1}$$

In this case, it is most convenient to solve the constraint explicitly and eliminate R_2:

$$R_2 = \sqrt{\sum_{i=3}^{2N-2} -1^{i+1} R_i^2 + R_1^2 - R_{2N;0}^2 + R_{2N+1}^2 - \frac{\mathcal{A}}{\pi}}, \tag{D.2}$$

where $\mathcal{A}$ is the (fixed) total area of gray rings, as before. Averaging the effective potential (3.11) in a manner analogous to eqs. (3.19)–(3.20) now yields much simpler integrals (it is now more convenient to use polar coordinates):

$$\langle V_{\text{eff}}(\xi)\rangle = \frac{(2\Delta)^{3-2N}}{\mathcal{N}} \frac{J_-}{\xi^2} \sum_{i=2}^{2N-1} (-1)^i \prod_{j=3}^{2N-1} \int_{R_{j;-}}^{R_{j;+}} \left(\Theta(\rho - R_{i;0}) + \Theta(R_{i;0} - \rho)\right) \; + \; (+ \; \leftrightarrow \; -), \tag{D.3}$$

where $(+ \; \leftrightarrow \; -)$ denotes the part proportional to J_+^2, and $R_{i;\pm} = R_{i;0} \pm \Delta$. The integrals are now trivial, except for the term $i = 2$ which contains the R_j-dependent function due to the solved constraint (D.2). This term evaluates to

$$\begin{aligned} \langle V_{\text{eff};2}(\xi)\rangle &\equiv \frac{(2\Delta)^{3-2N}}{\mathcal{N}} \frac{J_-}{\xi^2} \prod_{j=4}^{2N-1} \int_{R_{j;-}}^{R_{j;+}} \int_{R_{3-}}^{\tilde{R}_{3+}} dR_3 \\ \tilde{R}_{3+} &\equiv \min\left(R_{3+}, \sqrt{\sum_{i=4}^{2N-2} -1^{i+1} R_i^2 + \rho^2 - R_1^2 + R_{2N;0}^2 - R_{2N+1}^2 + \frac{\mathcal{A}}{\pi}}\right). \end{aligned} \tag{D.4}$$

This integral evaluates in terms of trigonometric functions, resulting in very long expressions. However, if we assume that $\Delta \ll R_1$, which is logical as fluctuations should be smaller than the macroscopic scale of the background, we get a tractable expression:

$$\begin{aligned} \langle V_{\text{eff}}(\xi)\rangle = \frac{1}{2\Delta\xi^2} \Bigg[&(J_+^2 - J_-^2) \sum_{i=3}^{2N-2} (-1)^i R_i + (J_+^2 + J_-^2)\Delta - \Delta^2 (J_+^2 + J_-^2)\rho\Theta(\rho - R_1)\Theta(R_{2N} - \rho) \\ &-2N\Delta(J_+^2 + J_-^2)\sqrt{\sum_{i=4}^{2N-2} -1^{i+1} R_i^2 + \rho^2 - R_1^2 + R_{2N;0}^2 - R_{2N+1}^2 + \frac{\mathcal{A}}{\pi}}\Theta(\rho - R_1)\Theta(R_{2N} - \rho)\Bigg]. \end{aligned} \tag{D.5}$$

The result is shown in figure 20. Now the averaged potential roughly corresponds to the grayscale ppotential at $g = 1/9$, instead of the correct value $g = 5/9$ for our setup. Therefore, even though we reproduce the necessary qualitative features, such as the potential well, the quantiative agreement is worse. Apparently, the microscopic dynamics of the fluctuations plays some role, and it is presumably closer to the Gaussian distribution as in most field theories.

JHEP02(2026)157

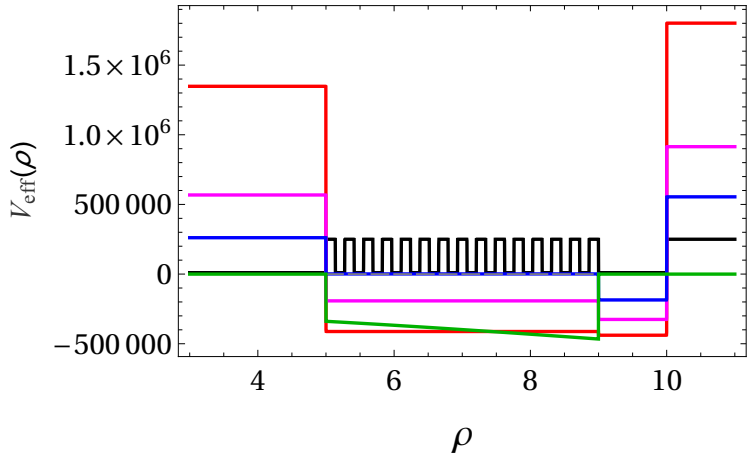

Figure 20. Near-plane effective potential $V_{\text{eff}}(\rho; \xi \mapsto 0)$ for two black disks and one 31-ring configuration (black), two black disks and one gray with decreasing nuance $g = 7/9, 5/9, 1/9$ (blue, magenta, red), and for the average over the rings (green). The integrals of motion are $(E, J_-, J_+, P_\phi) = (0.01, 0.04, 0.01, 0.1)$. The averaged (green) curve qualitatively mimics the grayscale potentials but quantitative agreement is not as good as for the Gaussian case.

Data Availability Statement. This article has no associated data or the data will not be deposited.

Code Availability Statement. This article has no associated code or the code will not be deposited.

References

[1] H. Lin, O. Lunin and J.M. Maldacena, *Bubbling AdS space and 1/2 BPS geometries*, *JHEP* **10** (2004) 025 [hep-th/0409174] [INSPIRE].

[2] D. Berenstein, *A toy model for the AdS/CFT correspondence*, *JHEP* **07** (2004) 018 [hep-th/0403110] [INSPIRE].

[3] I. Bena and N.P. Warner, *A harmonic family of dielectric flow solutions with maximal supersymmetry*, *JHEP* **12** (2004) 021 [hep-th/0406145] [INSPIRE].

[4] A.E. Mosaffa and M.M. Sheikh-Jabbari, *On classification of the bubbling geometries*, *JHEP* **04** (2006) 045 [hep-th/0602270] [INSPIRE].

[5] K. Skenderis and M. Taylor, *The fuzzball proposal for black holes*, *Phys. Rept.* **467** (2008) 117 [arXiv:0804.0552] [INSPIRE].

[6] R.C. Myers and O. Tafjord, *Superstars and giant gravitons*, *JHEP* **11** (2001) 009 [hep-th/0109127] [INSPIRE].

[7] G. Mandal, *Fermions from half-BPS supergravity*, *JHEP* **08** (2005) 052 [hep-th/0502104] [INSPIRE].

JHEP02(2026)157

[8] V. Balasubramanian et al., *Emergent classical spacetime from microstates of an incipient black hole*, *JHEP* **01** (2019) 197 [arXiv:1810.13440] [INSPIRE].

[9] P. Saad, S.H. Shenker and D. Stanford, *JT gravity as a matrix integral*, arXiv:1903.11115 [INSPIRE].

[10] A. Blommaert, *Dissecting the ensemble in JT gravity*, *JHEP* **09** (2022) 075 [arXiv:2006.13971] [INSPIRE].

[11] P. Saad, S.H. Shenker, D. Stanford and S. Yao, *Wormholes without averaging*, *JHEP* **09** (2024) 133 [arXiv:2103.16754] [INSPIRE].

[12] A. Blommaert and M. Usatyuk, *Microstructure in matrix elements*, *JHEP* **09** (2022) 070 [arXiv:2108.02210] [INSPIRE].

[13] A. Blommaert and J. Kruthoff, *Gravity without averaging*, *SciPost Phys.* **12** (2022) 073 [arXiv:2107.02178] [INSPIRE].

[14] A. Blommaert, L.V. Iliesiu and J. Kruthoff, *Gravity factorized*, *JHEP* **09** (2022) 080 [arXiv:2111.07863] [INSPIRE].

[15] V.P. Frolov, P. Krtous and D. Kubiznak, *Black holes, hidden symmetries, and complete integrability*, *Living Rev. Rel.* **20** (2017) 6 [arXiv:1705.05482] [INSPIRE].

[16] Y. Chervonyi and O. Lunin, *(Non)-integrability of geodesics in D-brane backgrounds*, *JHEP* **02** (2014) 061 [arXiv:1311.1521] [INSPIRE].

[17] I. Bena, D. Turton, R. Walker and N.P. Warner, *Integrability and black-hole microstate geometries*, *JHEP* **11** (2017) 021 [arXiv:1709.01107] [INSPIRE].

[18] M. Guica, T. Hartman, W. Song and A. Strominger, *The Kerr/CFT correspondence*, *Phys. Rev. D* **80** (2009) 124008 [arXiv:0809.4266] [INSPIRE].

[19] A. Castro, A. Maloney and A. Strominger, *Hidden conformal symmetry of the Kerr black hole*, *Phys. Rev. D* **82** (2010) 024008 [arXiv:1004.0996] [INSPIRE].

[20] M. Cvetic and F. Larsen, *Conformal symmetry for general black holes*, *JHEP* **02** (2012) 122 [arXiv:1106.3341] [INSPIRE].

[21] M. Cvetic and F. Larsen, *Conformal symmetry for black holes in four dimensions*, *JHEP* **09** (2012) 076 [arXiv:1112.4846] [INSPIRE].

[22] Y. Chen, H.W. Lin and S.H. Shenker, *BPS chaos*, *SciPost Phys.* **18** (2025) 072 [arXiv:2407.19387] [INSPIRE].

[23] J. Maldacena, S.H. Shenker and D. Stanford, *A bound on chaos*, *JHEP* **08** (2016) 106 [arXiv:1503.01409] [INSPIRE].

[24] V. Djukić and M. Čubrović, *Correlation functions for open strings and chaos*, *JHEP* **04** (2024) 025 [arXiv:2310.15697] [INSPIRE].

[25] D. Berenstein, E. Maderazo, R. Mancilla and A. Ramirez, *Chaotic LLM billiards*, *JHEP* **08** (2024) 056 [arXiv:2305.19321] [INSPIRE].

[26] D.E. Berenstein, J.M. Maldacena and H.S. Nastase, *Strings in flat space and pp waves from $N = 4$ superYang-Mills*, *JHEP* **04** (2002) 013 [hep-th/0202021] [INSPIRE].

[27] D. Berenstein and A. Holguin, *Open giant magnons on LLM geometries*, *JHEP* **01** (2021) 080 [arXiv:2010.02236] [INSPIRE].

[28] J.-P. Eckmann and D. Ruelle, *Ergodic theory of chaos and strange attractors*, *Rev. Mod. Phys.* **57** (1985) 617 [INSPIRE].

JHEP02(2026)157

[29] D. Berenstein and D. Kawai, *Smallest matrix black hole model in the classical limit*, *Phys. Rev. D* **95** (2017) 106004 [arXiv:1608.08972] [INSPIRE].

[30] Y.B. Pesin, *Lyapunov characteristic exponents and smooth ergodic theory*, *Usp. Mat. Nauk.* **32** (1977) 196.

[31] J.M. Seoane and M.A.F. Sanjuán, *New developments in classical chaotic scattering*, *Rept. Prog. Phys.* **76** (2012) 016001.

[32] M.M. Caldarelli, D. Klemm and P.J. Silva, *Chronology protection in anti-de Sitter*, *Class. Quant. Grav.* **22** (2005) 3461 [hep-th/0411203] [INSPIRE].

[33] S.S. Gubser, *Curvature singularities: the good, the bad, and the naked*, *Adv. Theor. Math. Phys.* **4** (2000) 679 [hep-th/0002160] [INSPIRE].

[34] D. Berenstein and A. Miller, *Superposition induced topology changes in quantum gravity*, *JHEP* **11** (2017) 121 [arXiv:1702.03011] [INSPIRE].

[35] E.J. Martinec and Y. Zigdon, *BPS fivebrane stars. Part II. Fluctuations*, *JHEP* **02** (2024) 034 [arXiv:2311.09157] [INSPIRE].

[36] E.J. Martinec and Y. Zigdon, *BPS fivebrane stars. Part I. Expectation values of observables*, *JHEP* **02** (2024) 033 [arXiv:2311.09155] [INSPIRE].

[37] C. Skokos, *The Lyapunov characteristic exponents and their computation*, *Lect. Notes Phys.* **790** (2010) 63 [arXiv:0811.0882] [INSPIRE].

[38] C.M. Bender and S.A. Orszag, *Advanced mathematical methods for scientists and engineers I*, Springer (1999) [DOI:10.1007/978-1-4757-3069-2] [INSPIRE].

JHEP02(2026)157

Published for SISSA by Springer

Received: November 20, 2023
Revised: February 9, 2024
Accepted: March 8, 2024
Published: April 4, 2024

Correlation functions for open strings and chaos

Vladan Đukić[a,b] **and Mihailo Čubrović**[b]

[a]*Faculty of Physics, University of Belgrade, Studentski Trg 12-16, 11000 Belgrade, Serbia*
[b]*Center for the Study of Complex Systems, Institute of Physics Belgrade, University of Belgrade, Pregrevica 118, 11080 Belgrade, Serbia*

E-mail: djukic@ipb.ac.rs, cubrovic@ipb.ac.rs

Abstract: We study the holographic interpretation of the bulk instability, i.e. the bulk Lyapunov exponent in the motion of open classical bosonic strings in AdS black hole/brane/string backgrounds. In the vicinity of homogeneous and isotropic horizons the bulk Lyapunov exponent saturates the MSS chaos bound but in fact has nothing to do with chaos as our string configurations live in an integrable sector. In the D1-D5-p black string background, the bulk Lyapunov exponent is deformed away from the MSS value both by the rotation (the infrared deformation) and the existence of an asymptotically flat region (the ultraviolet deformation). The dynamics is still integrable and has nothing to do with chaos (either in gravity or in field theory). Instead, the bulk Lyapunov scale captures the imaginary part of quasinormal mode frequencies. Therefore, the meaning of the bulk chaos is that it determines the thermal decay rate due to the coupling to the heat bath, i.e. the horizon.

Keywords: AdS-CFT Correspondence, Bosonic Strings, Black Holes, D-Branes

ArXiv ePrint: 2310.15697

https://doi.org/10.1007/JHEP04(2024)025

Contents

1 Introduction

Chaos in string theory has traversed the way from an arcane and little-noticed topic to a mainstream field, thanks to the ideas of fast scrambling and black holes as the fastest scramblers in nature [1], the Maldacena-Shenker-Stanford (MSS) maximum chaos bound for strongly coupled field theories with black hole duals [2] and the notion of out-of-time ordered correlators (OTOC) [3–5] and their applications in the physics of chaotic strongly coupled systems [6–8]. An important motor of the field is also the connection to recent progress on the black hole information problem [9–12] and the related puzzle of factorization [13–20]. In [21] it was demonstrated for the first time that the MSS scale characterizes also the time-disordered correlation functions on a string worldsheet, provided that the induced metric has a horizon and thus mimics black hole physics. The guiding idea through all these topics is of course the AdS/CFT duality, the unifying principle of many topics in string theory and gravity. Our primary interest thus lies in the dynamics in asymptotically AdS backgrounds.

Among the many questions which have opened up, there is one seemingly technical but in fact physically important subtlety. Several papers have reported the saturation of the bound $2\pi T$ for *bulk* orbits of particles [22, 23], or its slight modification/generalization for fields [22] and strings [24–30]; the systematic answer to the question of the bulk Lyapunov exponent is given in [31]. However, a very simple question arises: *why should there ever be*

JHEP04(2024)025

an MSS-like bound for bulk Lyapunov exponents? The OTOC exponent and its MSS bound $\lambda = 2\pi T$ in principle have no simple relation to the classical bulk motion and its Lyapunov exponent: the former is a property of a time-dependent correlation function in dual CFT, determined by a 4-wave scattering amplitude in the bulk, and the latter is the solution of a bulk equation of motion, for a single orbit, with no scattering and thus no OTOC-like interpretation in the bulk. This relates to a more general question: what is the CFT dual of a bulk orbit (and its Lyapunov instability exponent)? Some important work was done on this issue [32–37], and the outcome is that a bulk particle is dual to a shock wave perturbation of the dual CFT. But many details are still missing; in particular, the answer cited above holds for a geodesic with both endpoints on the AdS boundary; it is less clear what the CFT dual is for an orbit not reaching the boundary.

Paradoxically, a string in the bulk, specifically an open string, is perhaps an easier case for study. It is long known that a static or dragging string, with one endpoint in the interior and the other on the boundary, is dual to a heavy quark in the quark-gluon plasma of the supersymmetric Yang-Mills gauge theory [38, 39]. Likewise, an open string with both endpoints on the boundary represents a quark-antiquark pair [40–44], and encodes information on the confinement mechanism. It is thus a convenient framework to pose our main question: *what is the meaning of the bulk Lyapunov exponent and what does it have to do with the MSS bound?*

In this work we give a partial answer to the question and demonstrate it by a number of case studies involving bosonic open strings in various backgrounds.[1] There is, in fact, no unique answer to the question of the CFT dual to a bulk Lyapunov exponent: just as various string configurations have various field theory duals (a quark, a bound pair of quarks, an EPR pair, an accelerating quark...), likewise the Lyapunov stability of these different solutions will have different meanings. Furthermore, on the string worldsheet there are two coordinates thus we have two Lyapunov exponents, with different CFT meanings.

We also find that the MSS form of the exponent is really a red herring: in the strict infinite-coupling, infinite-N limit and with maximal symmetry, $2\pi T$ becomes a natural scale which has to appear in all fluctuation equations. As soon as we decrease symmetry (e.g. by considering a D1-D5-p bound state in the bulk that breaks rotational invariance) or include stringy effects, the bulk exponent (as well as OTOC [5] and other CFT correlation functions) undergo corrections, and do not coincide anymore (neither among themselves nor with the MSS bound). Recent work on universal near-horizon symmetries [45, 46] has shone additional light on the issue, allowing us to view the MSS scale as the fundamental property of black hole horizons, so it can appear in any CFT correlator which is sensitive to temperature T, i.e. which probes the energy scales smaller than T. The puzzle of "why $2\pi T$ pops out everywhere" is thus a fake issue: it disappears as soon as leading corrections or broken symmetries are taken into account.

The sharpest finding of our analysis is that the bulk Lyapunov exponents of a probe string in fact reproduce the quasi-normal mode (QNM) spectrum of the black hole or black

[1] While the dynamics of a superstring would be an interesting problem to study, in this work we stick solely to the bosonic sector. This is enough to understand the principles, and also to model holographically the dynamics of a heavy quark in Yang-Mills plasma.

JHEP04(2024)025

string background; in other words, they correspond to the thermal decay rate. Since this rate is also determined by the temperature times an $O(1)$ factor, we feel that this also provides an explanation for the origin of an MSS-like expression in bulk dynamics. It also clearly spells out that the relation of bulk instability scale to OTOC-ology and chaos in dual CFT is fake. In terms of the relation to QNM, our work is a stringy generalization of a similar result for geodesics [47, 48] and scalar waves [49, 50].

The plan of the paper is the following. In section 2 we study the simplest possible case: open string in AdS-Schwarzschild background, where the basic message already appears — the bulk Lyapunov exponent is $2\pi T$ but it is not related to chaos. In section 3 we demonstrate the same findings on more general background. In section 4 we address the dynamics of the string probe in the D1-D5-p and related backgrounds. Here we do a more detailed study, comparing the bulk variational equations to the retarded correlators dual to the string fluctuations, and finding that the bulk Lyapunov instability really described the quasinormal modes and hence the thermal decay rate in field theory. The final section sums up the conclusions.

2 Open string in AdS-Schwarzschild background

Our goal is to study the linear stability and fluctuations of classical solutions for the static open string stretching from the boundary to the horizon of an AdS black hole, the well-known simple holographic probe for a heavy quark in quark-gluon plasma.[2] Therefore, we write down the string action, derive the equations of motion and variational equations. Throughout the paper we consider only the bosonic sector of the string. Most of the time we will use the Polyakov action, but sometimes we will switch to the Nambu-Goto action, depending on the problem at hand.

2.1 Setup and radial fluctuations

Dynamics of a string in $D+1$-dimensional AdS-Schwarzschild spacetime with the time coordinate t, radial coordinate r, transverse spatial coordinates x_i $(i = 1, \dots D-1)$ and the horizon at r_h:

$$ds^2 \equiv G_{\mu\nu}(x)dx^\mu dx^\nu = r^2\left(-h(r)dt^2 + d\vec{x}^2\right) + \frac{dr^2}{r^2 h(r)}, \quad h(r) = 1 - \left(\frac{r_h}{r}\right)^D, \tag{2.1}$$

can be described by the Polyakov action for the string:

$$S_{\rm P} = -\frac{1}{2\pi\alpha'}\int d\tau d\sigma\ \eta^{\alpha\beta}\partial_\alpha X^\mu \partial_\beta X^\nu G_{\mu\nu}(X). \tag{2.2}$$

Here and in the rest of the paper $\alpha, \beta, \dots \in \{\tau, \sigma\}$ and $\mu, \nu, \dots \in \{t, r, \vec{x}\}$ stand for worldsheet and spacetime indices respectively. Latin indices $i, j, \dots$ count the transverse coordinates $x_1, \dots x_{D-2}$. As we know [38], the equations of motion are consistent with the following ansatz:

$$t = t(\tau), \quad R = R(\sigma), \quad X_1 = X_1(\tau, \sigma), \quad X_j = X_j(\tau),\ j = 2, \dots, D-1, \tag{2.3}$$

[2] In fact, to be precise, a heavy colored particle in super-Yang-Mills plasma.

JHEP04(2024)025

describing a string stretching from the horizon at r_h to the boundary at $r = \infty$. It is easiest to impose the flat worldsheet metric and solve for the Virasoro constraints together with the equations of motion:

$$\ddot{t}(\tau) = 0, \quad \ddot{X}_j(\tau) = 0, \ j = 2, \ldots, D-1 \tag{2.4}$$

$$\begin{aligned} &-2h^3(R)R^4(\sigma) - \left(R(\sigma)h'(R) + 2h(R)\right) R'^2(\sigma) + 2h(R)R(\sigma)R''(\sigma) + \\ &+ h^2(R)R^4(\sigma)\left[-R(\sigma)h'(R) + 2\left(X_1'^2(\tau,\sigma) + \dot{X}_1{}^2(\tau,\sigma) + \sum_{j=2}^{D-1} \dot{X}_j{}^2(\tau)\right)\right] = 0, \end{aligned} \tag{2.5}$$

$$2R'(\sigma)X_1'(\tau,\sigma) + R(\sigma)\left(X_1''(\tau,\sigma) - \ddot{X}_1(\tau,\sigma)\right) = 0, \tag{2.6}$$

$$\frac{R'^2(\sigma)}{R^4(\sigma)} + h(R)\left(-h(R)\dot{t}^2(\tau) + X_1'^2(\tau,\sigma) + \dot{X}_1{}^2(\tau,\sigma) + \sum_{j=2}^{D-1} \dot{X}_j{}^2(\tau)\right) = 0, \tag{2.7}$$

$$X_1' \cdot \dot{X}_1 = 0. \tag{2.8}$$

The equations for $t, X_2, \ldots, X_{D-1}$ (2.4) are trivially satisfied when these are functions linear in τ, thus we can set $t = \tau$ and $X_j = \text{const}$. Moreover, the second constraint (2.8) requires X_1 to depend on one variable only. For now we choose $X_1 = X_1(\sigma)$, i.e. the static open string/heavy quark (later on we will study both space- and time-dependent fluctuations). Now the remaining equation for $R(\sigma)$ (eq. (2.5)), together with the nontrivial Virasoro constraint (2.7), also decouples from $X_1(\sigma)$ and simplifies to the following form

$$4h^3(R)R^3(\sigma) + h^2(R)h'(R)R^4(\sigma) + h'(R)R'^2(\sigma) - 2h(R)R''(\sigma) = 0. \tag{2.9}$$

The same equation can be derived from the effective Lagrangian, obtained by first substituting the trivial solutions $t = \tau$ and $X_j = 0$, $\forall j \neq 1$ into the Polyakov Lagrangian, and then making use of the Virasoro constraint (2.7) to eliminate $X_1'^2$:

$$\mathcal{L}_{\text{eff}} = \frac{-h^2(R) - f(R)R'^2(\sigma) - h(R)X_1'^2(\sigma)}{\sqrt{f(R)}h(R)}. \tag{2.10}$$

This Lagrangian has the worldsheet energy as its integral of motion and is thus integrable, as we will argue more rigorously in the following section.

2.1.1 Variational equations and Lyapunov exponents

We will now write down the variational equation corresponding to the on-shell equation of motion (2.9). We will find that the solution to the variational equation is an exponential function, which defines the Lyapunov exponent the usual way. The unusual detail is the fact that both $R(\sigma)$ and its variation $\delta R(\sigma)$ depend on the *spatial* coordinate σ. Studying the spatial dependence of the worldsheet field and calling it dynamics as we do might be controversial; so is the term Lyapunov exponent for the growth exponent of the variation $\delta R(\sigma)$. The important difference between σ and τ dynamics is that the worldsheet time is unbounded and one can define asymptotic quantities as it is usually done for the Lyapunov exponent (defining it as the limit of small initial variation and long-time evolution

JHEP04(2024)025

$\lambda = \lim_{t\to\infty} \lim_{\delta x(0)\to 0} \log\left(\delta x\left(t\right)\right)/t$, for some generic coordinate x). The extent of the σ coordinate is finite and there is no analogue to $\lim_t \to \infty$. Therefore, while we talk all the time of Lyapunov exponents, we really study what is often called finite-time Lyapunov indicator in the context of time evolution, i.e. the exponent defined locally rather than asymptotically. This is however often assumed as a matter of course: the bulk Lyapunov exponent (in time) computed, e.g. in [22, 26, 47], is also the finite-time quantity.

We are mainly interested in studying the variation near the horizon. To that end, we substitute $R(\sigma) \mapsto r_0 + \varepsilon\delta R(\sigma)$ into eq. (2.9), expand it in ε small to linear order, and finally take the limit $r_0 \to r_h$.[3] This yields the near-horizon variational equation:

$$\delta R'' - D^2 r_h^2 \delta R = 0. \tag{2.11}$$

The solution is thus $\delta R \propto e^{\pm 2\lambda_L \sigma}$ with a pair of Lyapunov exponents of equal magnitude and with opposite signs, as it has to happen in a Hamiltonian system. The exponent formally coincides with the MSS bound:

$$\lambda_L = \frac{D r_h}{2} = 2\pi T. \tag{2.12}$$

The reason why we define the Lyapunov exponent with a factor of 2, i.e. through $\delta R \propto e^{\pm 2\lambda_L \sigma}$ instead of $\delta R \propto e^{\pm \lambda_L \sigma}$ is that the same expression appears also in the OTOC growth, and follows from the definition of OTOC on the thermal circle. Here, for bulk equations of motion, this argument is irrelevant (these are different quantities!) but we nevertheless want to stay consistent with the definition of the MSS bound as we want to compare the two situations.

We have shown that the exponent is $2\pi T$ regardless of the spacetime dimension or any other parameters save the temperature. While it is tempting to call this "maximal chaos in the bulk", we will soon show that this system is not chaotic at all. Therefore we should interpret λ_L not as a measure of chaos (neither in the bulk nor in CFT) but as some characteristic scale related to the near-horizon physics, that will likely correspond to relaxation time of some perturbations around a thermal horizon. Toward the end of the paper we will make this precise.

2.2 Integrability of the static open string

Here we prove that the simplest open string configuration — a static open string at the horizon of the AdS-Schwarzschild geometry — is integrable, unlike the motion of a closed winding string which is nonintegrable in the presence of a black hole [51, 52]. We emphasize that this does *not* imply integrability of the open string for generic boundary conditions.

We will preform the same type of analysis that is done in [51], exploiting the Kovacic algorithm [51, 53–56]. The algorithm can be described as follows: (1) find a family of solutions

[3] The order of limits is important because of the coordinate singularity at the horizon. If we immediately put $R(\sigma) \mapsto r_h + \varepsilon\delta R(\sigma)$ we end up with an equivalent variational equation which is however *nonlinear*: $\delta R'' - \delta R'^2/(2\delta R) - (D^2/2) r_h^2 \delta R = 0$; the nonlinearity stems from the vanishing of a term in the on-shell equation at the horizon, so that a linear expansion in ε yields an equation which is not necessarily linear in δR and its derivatives. If we try to expand the Lagrangian $\mathcal{L}_{\text{eff}}$ and then solve the equation which follows from the leading correction to $\mathcal{L}_{\text{eff}}$ (quadratic in ε), the coefficients of this equation diverge at $r = r_h$. Again, all of this is merely about the coordinate system we use; we could work in Kruskal-Szekeres coordinates and avoid the problem.

JHEP04(2024)025

to the equations of motion defining an invariant plane in the parameter space (2) write down the normal variational equation (NVE) for the invariant plane (3) solve the NVE so obtained and check whether it is expressible in terms of Liouvillian functions; these are the elementary functions (powers, exponentials, trigonometric functions and their inverses), rational functions of such elementary functions, and their integrals.[4]

We want to show the integrability of the system described by the effective Lagrangian in eq. (2.10). One obvious invariant plane is the $R - X_1$ plane for a straight string solution:

$$R(\sigma) = r_h, \;\; X_1(\sigma) = \text{const.} \equiv X_c. \tag{2.13}$$

One can see that this plane is invariant simply by observing that the canonical momentum corresponding to the off-plane motion is zero: $p'_X = \partial \mathcal{L}_{\text{eff}}/\partial X_1 = 0$. The corresponding NVE along the X_1-direction is trivial: $\delta X_1'' = 0$, yielding the conclusion that the system is integrable. We have seen that the system nevertheless exhibits an exponential growth of the in-plane variation with a positive Lyapunov exponent in the near-horizon region. By itself this is not surprising: a local instability can lead to a growing mode even in a trivially integrable system, the simplest example being the inverse chaotic oscillator [57]. This is similar to findings of [31] where it is noted that horizons are really sources of instability in the bulk. Even integrable systems can display local instability in the vicinity of thermal horizons.

We need to make one thing clear. The integrability of the static open string Lagrangian (2.10) that we have demonstrated in no way conflicts the established nonintegrability of string motion in black hole and D-brane backgrounds proved in [51, 55]. The fact that a ring string in these backgrounds is nonintegrable, as found in the aforementioned references, is enough to prove the nonintegrability of string motion in these geometries in general, and this likely holds also for open strings with sufficiently complicated boundary conditions. On the other hand, the existence of special solutions and boundary conditions which are integrable (and therefore certainly nonchaotic) is perfectly possible also in a nonintegrable system.

3 Open string in other backgrounds

In order to further corroborate the universality of the result (2.12), we will repeat exactly the same analysis for two more backgrounds: (1) a general hyperscaling-violating metric and (2) a black Dp brane. The former is quite relevant for many holographic purposes, the latter does not in general have a holography dual (as its asymptotic geometry is in general not AdS) but it does appear as a sector in various backgrounds (and of course the AdS throat of the D3 brane provides the simplest and most famous top-down AdS/CFT construction). This endeavour might look like mere stamp collecting but it has a purpose: to show that the result is not special to AdSS metric and also to show (from the Dp case) that by itself it has nothing to do with holography or AdS asymptotics — it is all about thermal horizons.

[4] One can find the reasoning behind this algorithm in the literature. In brief, the existence of such a solution is equivalent to the solvability of the identity component G^0 of the Galois group; conversely, their nonexistence is equivalent to G^0 being not solvable, and hence non-Abelian. Non-Abelian nature of G^0 tells us that no complete system of integrals of motion in involution exists, therefore the system is nonintegrable.

JHEP04(2024)025

3.1 General hyperscaling-violating background

In our first example we closely follow the idea of [31] and study bulk motion in a broad class of bulk geometries: hyperscaling-violating horizons at finite temperature, constructed in [58–61] as gravity duals of effective field-theories with scaling and long-range entanglement, thought to be ubiquitous in quantum-many body systems. In [31], it is shown that the bulk geodesics, i.e. particle orbits also have the $2\pi T$ Lyapunov exponent in a large part of the parameter space though not everywhere; here we show that static strings/holographic heavy quarks *always* yield $2\pi T$. The background metric reads

$$ds^2 = -r^{2\mathfrak{z}-\frac{2\theta}{D-2}} f(r) dt^2 + \frac{1}{f(r) r^{2+\frac{2\theta}{D-2}}} dr^2 + r^2 d\vec{x}^2, \quad f(r) = 1 - \left(\frac{r_h}{r}\right)^{D-2+\mathfrak{z}-\theta}, \tag{3.1}$$

and depends on two parameters, the Lifshitz exponent[5] $\mathfrak{z}$ that measures the anisotropy of space versus time scaling (so that Lorentz-invariant backgrounds correspond to $\mathfrak{z} = 1$) and the hyperscaling exponent θ which measures the deviation from the dimensional scalinig of free energy and roughly corresponds to long-range-entangled degrees of freedom. By definition, the temperature of the horizon at r_h is found as:

$$4\pi T = -\frac{g'_{tt}(r_h)}{\sqrt{g_{tt}(r_h) g_{rr}(r_h)}} = (D - 2 - \theta + \mathfrak{z}) r_h^{\mathfrak{z}}. \tag{3.2}$$

We can easily redo the same analysis as for the AdSS configuration, keeping the same ansatz (2.3) and the equations of motion analogous to (2.4)–(2.8). When everything is said and done, we obtain the near-horizon variational equation

$$\delta R''(\sigma) - (D - 2 - \theta + \mathfrak{z})^2 r_h^{2\mathfrak{z}} \delta R(\sigma) = 0, \tag{3.3}$$

which, according to (3.2), implies again $\lambda_L = 2\pi T$ with the ansatz $\delta R \sim \exp(2\lambda_L \sigma)$.

3.2 Dp brane and related backgrounds

3.2.1 Extremal black Dp brane

Consider first the single Dp brane geometry in 10 spacetime dimensions. To the best of our knowledge no systematic work was done on string dynamics in brane backgrounds, except for the general proofs of nonintegrability in [51, 55] and of course the near-brane limit of the D3 brane when the asymptotics becomes AdS. The metric reads

$$ds^2 = \frac{\eta_{\mu\nu} dx^\mu dx^\nu}{f^2(r)} + f^2(r) \left(dr^2 + r^2 d\Omega_k\right), \quad \mu = 0, \dots p \tag{3.4}$$

$$f(r) = \left(1 + \frac{Q}{r^n}\right)^m, \quad n = 7 - p, k = 8 - p, m = \frac{1}{4}. \tag{3.5}$$

Here, r is the radial coordinate, x^μ are the directions on the brane, while $d\Omega_k$ is the k-sphere with coordinates $\Phi_1, \dots \Phi_k$. The string configuration we consider is completely analogous

[5] We denote the Lifshitz exponent by $\mathfrak{z}$ rather than the usual z, as z will be used for the radial coordinate $z = 1/r$. Likewise ζ is taken by another coordinate to be used in section 4.

JHEP04(2024)025

to the static open string studied previously in AdS black hole backgrounds:

$$\begin{aligned} t = t(\tau), \quad & X_1 = x_1, \quad \dots \quad X_p = x_p, \\ R = R(\sigma), \quad & \Phi_1 = \phi_1, \quad \dots \quad \Phi_k = \phi_k \end{aligned} \tag{3.6}$$

Therefore, our string configuration is only nontrivial in the directions transverse to the brane, and reduced to a point on the k-sphere (i.e., in longitudinal directions). In appendix A we show that more general ansätze are possible; but for our purposes, eq. (3.6) is perfectly sufficient. For the time direction we can again choose $t(\tau) = \tau$. We have one nontrivial Virasoro constraint which, upon plugging into the equation of motion, yields:

$$R'' + \frac{2f'(R)}{f(R)^5} - \frac{(R')^2 f'(R)\left(-f(R)^4 + QR^{p-7} + 1\right)}{f(R)^5} = 0. \tag{3.7}$$

We have some analytical control over the eq. (3.7) and its variational equation for small R, i.e. near the brane, when we expand $R(\sigma) = \epsilon + \delta R(\sigma)$. The variational equation then reads

$$\delta R'' - \epsilon^{5-p}\sqrt{\frac{(7-p)(6-p)}{2Q}}\delta R = 0, \tag{3.8}$$

where $R \sim \epsilon$, i.e. the small parameter is the distance from the brane; since this limit means $\epsilon \to 0$, the bulk Lyapunov exponent vanishes. We will see the opposite situation with black Dp branes, in the presence of a thermal horizon. The solution (3.8) is obviously only sensible for $p \leq 5$ but for $p > 5$ the same conclusion is reached, only the expansion in r large (ϵ small) is different.

3.2.2 Non-extremal black Dp brane

We will now consider a non-extremal black brane, the finite-temperature generalization of the extremal solution at temperature T:[6]

$$ds^2 = -h(r)\frac{dt^2}{f^2(r)} + \frac{d\vec{x}^2}{f(r)^2} + f^2(r)\left(\frac{dr^2}{h(r)} + r^2 d\Omega_k^2\right) \tag{3.9}$$

$$f(r) = \left(1 + \frac{Q}{r^n}\right)^m, \quad h(r) = 1 - \left(\frac{r_h}{r}\right)^4, \qquad n = 7-p, \;\; k = 8-p, \;\; m = \frac{1}{4} \tag{3.10}$$

$$\frac{1}{T} = \frac{4\pi f(r_h)}{\sqrt{h'(r_h)(h(r)/f^2(r))'|_{r=r_h}}} = \frac{4\pi r_h \sqrt{1 + Qr_h^{p-7}}}{p+1}. \tag{3.11}$$

In the limit $r_h \to 0$ (equivalently, $T = 0$) the black brane becomes the previously studied extremal black brane. The coordinates are the same as in the extremal solution (3.5). The $d\Omega_k$ sector is insensitive to temperature, which can be seen from the fact that its metric is independent of the redshift function h. The effect of the thermal horizon is thus seen solely

[6] For concreteness we again assume $p \leq 5$ but, just like for the extremal brane, the generalization for $p > 5$ is easy.

JHEP04(2024)025

in the equation of motion for R (after plugging in the Virasoro constraint as usual):

$$R''-\left[\frac{f'(R)\left(-f(R)^4+QR^{p-7}+1\right)}{f(R)^5}+\frac{h'(R)}{2h(R)}\right]R'^2-\frac{h(R)\left(f(R)h'(R)-4h(R)f'(R)\right)}{2f(R)^5}=0. \tag{3.12}$$

Following the same logic as before, we find the near-horizon variational equation:

$$\delta R''-\frac{(p+1)^2}{r_h^2+Qr_h^{p-5}}\delta R=0. \tag{3.13}$$

Looking for a solution of a form $\sim\exp(2\lambda_L\sigma)$ and using eq. (3.11), we find that $\lambda_L=2\pi T$. The ubiquitous $2\pi T$ is present even if the metric is asymptotically flat, as thermal horizons generate instability, whatever the faraway asymptotics. The holographic meaning of this instability is theory-dependent, and in general does not exist when there is no AdS region.

3.2.3 From $\mathbf{AdS}_{p+2}\times\mathbb{S}^k$ throat to flat space

Following [51, 62, 63], we can consider a modification of the Dp brane geometry at zero or finite temperature to obtain a metric interpolating from an $\mathrm{AdS}_{p+2}\times\mathbb{S}^k$ throat (near-brane) to flat space in the far region; such solutions appear as solutions of supergravity and interpolate between different vacua. The expressions for the metric remain the same as before (eq. (3.5) at $T=0$ or eq. (3.10) at $T>0$) but the parameters are:

$$m=\frac{1}{n},\quad p,n,k \text{ arbitrary}. \tag{3.14}$$

One can easily check that indeed for $Q\to 0$ or equivalently $r\to r_h$ (including the case $r_h=0$ for the extremal brane) we obtain $\mathrm{AdS}_{p+2}\times\mathbb{S}^k$ and for $Q\to\infty$ or equivalently $r\to\infty$ we get flat space (in fact, its product with the k-sphere). We proceed along the same lines as before, hence we only give the end results. The variational equation reads

$$\delta R''-\left(\frac{p+1}{r_h}\right)^2\left(1+Qr_h^{p-7}\right)^{\frac{4}{p-7}}\delta R=0, \tag{3.15}$$

which yields once again $\lambda_L=2\pi T$, computing the temperature by definition, similar as in eq. (3.11). Now we can however obtain an analytic solution also in the far region, which interpolates to $\mathbb{R}\times\mathbb{R}^{p+1}\times\mathbb{S}^k$. Writing $R(\sigma)=1/\epsilon+\delta R(\sigma)$ with $\epsilon\to 0$, we get the variational equation

$$\delta R''+2(8-p)Q\epsilon^{9-p}\delta R=0, \tag{3.16}$$

yielding $\lambda_L=0$ as the coefficient of δR is positive (hence the dynamics is oscillatory rather than exponentially growing), and in addition it drops to zero as we reach infinity.

All these examples strongly suggest that the $2\pi T$ exponent (with the same value, but different meaning from the MSS bound for CFT chaos) for the unstable saddle point in bulk motion is present if and only if the geometry has a static thermal horizon, holographic or not. In the next section we will see that the presence of rotation changes the outcome. This will lead us to the general conclusion: that the bulk near-horizon Lyapunov exponent is universal for a given symmetry class of the metric. For maximally symmetric horizons (isotropic and static) the result is always $2\pi T$, which is argued in detail also in [46], on the basis of [45].

JHEP04(2024)025

3.2.4 Numerical solutions

Although the equations we solve so far are quite elementary, it is always nice to have a numerical check too. Therefore, in this subsubsection we solve the equations of motion numerically; also, this is the only way to look at the string in whole space.[7] We will see explicitly that the system is integrable and yet that the variational equations have exponentially growing solutions.

We will look at the D3 black brane, The aim is thus to solve eq. (3.12) and its variational equation for $p = 3$.[8] In order to do so, it is more convenient to use the coordinate $z = 1/r$, so that the equation of motion for the new worldsheet field $Z(\sigma)$ becomes

$$Z'' - \frac{Z'^2}{Z} - \frac{h'(Z)Z'^2}{2h(Z)} - \frac{h^2(Z)Z^3}{f^4(Z)}\left(1 - Z\left(\frac{2f'(Z)}{f(Z)} + \frac{h'(Z)}{2h(Z)}\right)\right) = 0. \tag{3.17}$$

We impose Dirichlet conditions at the brane and Neumann conditions at the other end (open strings should be attached to branes but they can float freely in the asymptotically flat outer region). Once we have the solutions $Z(\sigma)$ we substitute the solution into the variational equation:

$$\begin{aligned}\delta Z'' - \frac{(2h(Z) + Zh'(Z))\,Z'}{Zh(Z)}\delta Z' + \frac{1}{2Z^2}\Bigg[&\frac{Z'^2\left(2h^2(Z) + Z^2h'^2(Z) - h(Z)Z^2h''(Z)\right)}{h^2(Z)} \\ &- \frac{20v^2h^2(Z)Z^6f'^2(Z)}{f^6(Z)} + \frac{4v^2h(Z)Z^5\left(3f'(Z)\left(2h(Z) + Zh'(Z)\right) + h(Z)Zf''(Z)\right)}{f^5(Z)} \\ &- \frac{v^2Z^4\left(6h^2(Z) + Z^2h'^2(Z) + h(Z)Z\left(8h'(Z) + Zh''(Z)\right)\right)}{f^4(Z)}\Bigg]\delta Z = 0.\end{aligned} \tag{3.18}$$

For δZ the meaningful boundary condition is the fixed (and small) difference between the on-shell trajectory and its clone at the brane ($\delta Z(\sigma = 0) = \epsilon$) and the Neumann condition at infinity (since the strings float freely so does the difference between to string profiles). The outcome is given in figure 1. Along with the radial profiles of the string for different temperatures, we plot the near-horizon values of the numerically computed Lyapunov exponent $\lambda_L^{(n)} = \log\left(\delta Z\left(\sigma_0\right)/\epsilon\right)/2$, where σ_0 is some near-brane cutoff (we want the Lyapunov exponent near the brane thus σ_0 should cut off the far-from-brane part).[9] The numerics is reasonably close to the analytic result, providing an additional confirmation.

4 Open string in D1-D5-p black string background

So far we have explored the bulk instability of open strings in black hole and black brane backgrounds and we have found the saturation of a fake MSS bound — fake as it is unrelated to chaos (the configuration we consider is even integrable, though a more involved setup likely

[7] Remember we have no analytic control at intermediate distances, far from both the brane/horizon and the infinity/AdS boundary (depending on the geometry).

[8] The value $p = 3$ is chosen as the D3 brane is particularly relevant for applications, having also the AdS throat, but the numerics works the same way for any p.

[9] Of course, we have checked that the results do not strongly depend on σ_0.

JHEP04(2024)025

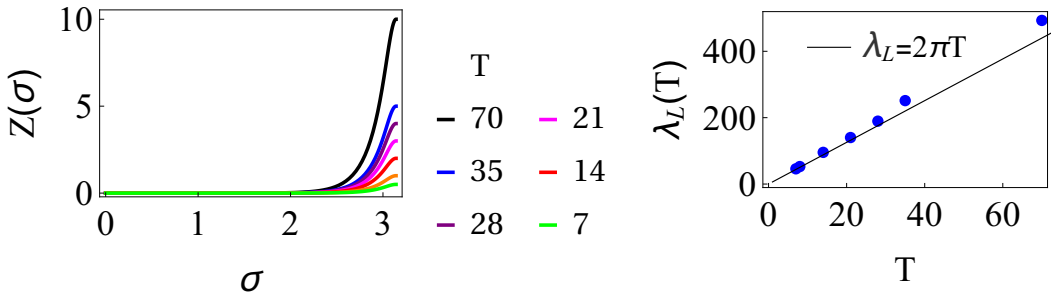

Figure 1. Radial profile $Z(\sigma)$ (A) and the numerical Lyapunov exponent $\lambda_L^{(n)} = \log\left(\delta Z\left(\sigma_0\right)/\epsilon\right)/2$ (B) for the static open string in thermal black brane background, for a range of temperatures T. We take $\sigma_0 = 0.2$ for the cutoff but values between 0.1 and 0.5 yield similar results. We compare the numerical result for the Lyapunov exponents to the analytic estimate (i.e., the chaos bound) and find reasonable agreement.

would not be such). Now we will interpret this finding and relate it to the thermal correlators and quasi-normal modes in a theory which is particularly interesting as we know something not only about the (super)gravity solution and the dual large-N field theory, but also about the microscopics: the D1-D5-p black string [64–69]. This setup is celebrated for being the first black hole solution in string theory for which the entropy was computed by counting the microscopic degrees of freedom, obtaining for a horizon area A the famous Bekenstein-Hawking result $S = A/4$ [65]. Another famous result is the calculation of the greybody factor in [64], the logical macroscopic extension of the entropy calculation. To remind, the greybody factor is obtained in [64] as the absorption cross section for a wavepacket in the black string background. In holographic setups, where the relevant near-horizon dynamics is dual to a two-dimensional CFT, the absorption cross section can be obtained from the imaginary part of the retarded Green's function.

Our idea here is twofold. First, we study the Lyapunov stability in D1-D5-p background — this will yield some surprises as the geometry has a global rotation with angular velocity Ω; so far we have only studied static geometries. Second, we will relate the Lyapunov exponent to the retarded propagator in dual field theory and pinpoint what it tells us about the meaning of bulk instability.

4.1 Holography of the D1-D5-p system: a reminder

The background describing the D1-D5-p black string reads

$$ds^2 = \frac{1}{\sqrt{f(r)}}\left(-dt^2 + dx_5^2 + \frac{r_0^2}{r^2}\left(\cosh\Sigma dt + \sinh\Sigma dx_5\right)^2\right) + \\ + \sqrt{f(r)}\left(\frac{dr^2}{h(r)} + r^2\left(d\psi^2 + \sin^2\psi\left(d\theta^2 + \sin^2\theta d\phi^2\right)\right)\right), \tag{4.1}$$

$$f(r) = \left(1 + \frac{r_1^2}{r^2}\right)\left(1 + \frac{r_5^2}{r^2}\right), \quad h(r) = 1 - \frac{r_0^2}{r^2}. \tag{4.2}$$

As usual, t and r are the time and radial coordinate respectively, ψ, θ and ϕ are the angles on the 3-sphere, and x_i $(i = 1, \ldots 5)$ are the Cartesian coordinates in the plane. This is a classical

JHEP04(2024)025

solution of ten-dimensional type IIB supergravity compactified on $T^5 \cong T^4 \times \mathbb{S}^1$ [64, 70]. It is charged under the Ramond-Ramond field of the corresponding theory; since D1 and D5 branes are magnetically dual to each other we get electric and magnetic charges that are related to the radii r_1 and r_5, respectively.[10] There is also an additional charge associated to the p-momentum along D1-brane, i.e. the Kaluza-Klein (KK) mode on $\mathbb{S}^1$, related to factors of $r_0^2 \cosh^2 \Sigma$ in the metric (4.1)–(4.2). In the dilute gas regime these three charges satisfy [64]:

$$r_0, r_0 \sinh \Sigma \ll r_1, r_5. \tag{4.3}$$

The solution is anisotropic and rotating for $\Sigma \neq 0$ as we see from the presence of non-vanishing tx_5-component in the metric (4.1), implying that we now have the left and right temperature:

$$T_L = \frac{r_0 e^{\Sigma}}{2\pi r_1 r_5}, \qquad T_R = \frac{r_0 e^{-\Sigma}}{2\pi r_1 r_5}. \tag{4.4}$$

We may further define the "average" (Hawking) temperature T as $1/T = (1/T_L + 1/T_R)/2$. This temperature and entropy are given by

$$\frac{1}{T} = \frac{2\pi r_1 r_5 \cosh \Sigma}{r_0}, \qquad S = \frac{2\pi^2 r_1 r_5 r_0 \cosh \Sigma}{4}. \tag{4.5}$$

We will need a few more features of this solution. The first is that in the extremal case ($T, S \propto r_0 = 0$), also known as the extremal D1-D5 bound state system, the near-horizon geometry becomes $\mathrm{AdS}_3 \times \mathbb{S}^3$. We can show this by performing the coordinate transformation $t \to t/\varepsilon L,\ r \to \varepsilon L r,\ x_5 \to x_5/\varepsilon L$ in the metric (4.1), where $L^2 = r_1 r_5$: in the limit $\varepsilon \to 0$ we recover the $\mathrm{AdS}_3 \times \mathbb{S}^3$ geometry

$$ds^2_{\mathrm{NHE}} \approx \frac{r^2}{L^2}\left(-dt^2 + dx_5^2\right) + L^2 \frac{dr^2}{r^2} + L^2 d\Omega_3^2. \tag{4.6}$$

On the other hand in the near-extremal case ($r_0 \to 0,\ \Sigma \to \infty$), the p-momentum survives and we still have the full D1-D5-p system, with a near-horizon geometry of the rotating Banados-Teitelboim-Zanelli (BTZ) black hole:

$$ds^2_{\mathrm{NHNE}} \approx \frac{r^2}{L^2}\left(-dt^2 + dx_5^2\right) + L^2 \frac{dr^2}{r^2 - r_0^2} + \frac{r_0^2}{L^2}\left(\cosh \Sigma dt + \sinh \Sigma dx_5\right)^2 + L^2 d\Omega_3^2. \tag{4.7}$$

The procedure to derive this is the same as in the extremal case, except that now we also need to take $r_0 \to \varepsilon L r_0$. In order to translate the metric (4.7) into the standard coordinates for BTZ black holes we have to perform an additional coordinate transformation:

$$r^2 = w^2 - w_-^2, \quad w_+ = r_0 \cosh \Sigma, \quad w_- = r_0 \sinh \Sigma. \tag{4.8}$$

For convenience we will write down the metric of the rotating BTZ in these coordinates:

$$ds^2_{\mathrm{BTZ}} = -\frac{(w^2 - w_+^2)(w^2 - w_-^2)}{L^2 w^2} dt^2 + \frac{L^2 w^2 dw^2}{(w^2 - w_+^2)(w^2 - w_-^2)} + \frac{w^2}{L^2}\left(\frac{w_+ w_-}{w^2} dt + dx_5\right)^2. \tag{4.9}$$

The angular velocity is given by $\Omega = w_-/L w_+ = \tanh \Sigma / L$.

[10] One can think of these charges also as representing the number of copies in the stack of D1 branes compactified on $\mathbb{S}^1$ along the x_5 direction, and in the stack of D5 branes wrapping the whole $T^4 \times \mathbb{S}^1$ manifold.

JHEP04(2024)025

From the above it is clear that the dual CFT lives in 1+1 spacetime dimension and encodes the physics of the $AdS_3 \times \mathbb{S}^3$ sector: in the holographic regime the large-r flat asymptotics of the geometry (4.1) have to decouple. The classical gravity solution of course corresponds to the strongly coupled regime in CFT, however some direct comparisons were made (and count among the famous early tests of AdS/CFT) in the weakly-coupled regime where the CFT is approachable from field theory side [67, 69, 71, 72] and some basic results from gravity side (like thermodynamics) still hold for reasons of continuity. In this regime the CFT has an orbifold point [71, 72] which acts as UV deformation, driving the theory toward a weakly coupled regime. This is seen in gravity as the deformation of the metric away from the near-brane region (AdS_3 or BTZ). Therefore, we understand, at least to some extent, the UV physics and the meaning of the UV deformation of the theory.

4.2 Radial fluctuations

We consider a static open string in D1-D5-p background stretching from interior to the boundary just like in previous examples. In particular, we postulate the following string configuration

$$\begin{aligned} &t(\tau,\sigma)=\tau, \qquad R(\tau,\sigma)\equiv R(\sigma),\\ &\Psi(\tau,\sigma)\equiv\psi(\tau), \quad \Theta(\tau,\sigma)\equiv\pi/2, \quad \Phi(\tau,\sigma)\equiv\phi(\tau), \quad X_5(\tau,\sigma)\equiv X_5(\sigma). \end{aligned} \tag{4.10}$$

The τ-dependent degrees of freedom $\{\Psi,\Phi\}$ decouple. The remaining fields R and X_5 also decouple from each other, since we can combine the equation of motion for R with the nontrivial Virasoro constraint

$$\frac{f(R)R'^2(\sigma)}{h(R)}+X_5'^2(\sigma)+\frac{r_0^2\left(v^2\cosh^2\Sigma+\sinh^2\Sigma X_5'^2(\sigma)\right)}{R^2(\sigma)}=1 \tag{4.11}$$

to obtain the following equation

$$\begin{aligned} &2fh^2\left(-2r_0^2\cosh^2\Sigma+R^2\right)+f'h^2R\left(-r_0^2\cosh^2\Sigma+R^2\right)+\\ &+f^2R^2\left(-\left(2h+Rh'\right)R'^2+2hRR''\right)=0. \end{aligned} \tag{4.12}$$

The effective Lagrangian for the coordinates R and X_5 takes the form

$$\mathcal{L}=\frac{1}{\sqrt{f(R)}}\left[\left(-1+\frac{r_0^2\cosh^2\Sigma}{R^2}\right)-\frac{f(R)R'^2}{h(R)}-\left(1+\frac{r_0^2\sinh^2\Sigma}{R^2}\right)X_5'^2\right], \tag{4.13}$$

and reproduces eq. (4.12) when combined with the Virasoro constraint (4.11).

We will assume that we are in the dilute gas regime, like in [64], defined by $r_0, r_0\sinh\Sigma \ll r_1, r_5$. This boils down to the condition $T \ll 1/r_1, 1/r_5$. As usual, we can solve the equation analytically in two distinct regions: (1) near-horizon region $r \sim r_0, r_0\sinh\Sigma \ll r_1, r_5$ and (2) far region $r_0, r_0\sinh\Sigma \ll r \sim r_1, r_5$.

Expectedly, the system described by the Lagrangian (4.13) is integrable. Applying the NVE methods, we can choose the invariant plane to be $\{t=\tau, R=r_0, \Psi=0, \Theta=\pi/2, \Phi=0, X_5=\text{const.}\}$. Since X_5 is a cyclic coordinate in (4.13), its conjugate momentum

JHEP04(2024)025

is constant: $p'_{X_5} = \partial\mathcal{L}/\partial X_5 = 0$. Therefore, the $R - X_5$ plane is indeed invariant under the evolution of the system (along σ). The normal variational equation therefore corresponds to the variations in the X_5-direction, yielding $\delta X_5'' = 0$. Just like the open string dynamics on the Schwarzschild horizon, this system is integrable.[11] In both cases, the extra integrals of motion are simply the transverse momenta.

We solve the variational equation of the radial coordinate in (4.12) obtained by perturbing the horizon solution $R(\sigma) = r_0$ as $R \sim r_0 + \delta R(\sigma)$:

$$\delta R'' - \frac{2\mathfrak{a}^4}{r_0^6 f^2(r_0)}\delta R = 0, \tag{4.14}$$

$$\mathfrak{a}^4 \equiv r_0^2(r_1^2 + r_5^2) + 2r_1^2 r_5^2 + r_0^2\left(2r_0^2 + r_1^2 + r_5^2\right)\cosh 2\Sigma \tag{4.15}$$

Plugging in the expression for f, we find the exponent of the asymptotic growth of the solution, determined as before by $\sim e^{2\lambda_L \sigma}$:

$$\lambda_L = \frac{r_0}{r_1 r_5}\sqrt{1 + \frac{r_0^2(r_1^2 + r_5^2)}{2r_1^2 r_5^2}\cosh(2\Sigma)}. \tag{4.16}$$

The above expression[12] can be written in terms of the temperatures (4.4)–(4.5) as:

$$\lambda_L = 2\pi T\cosh\Sigma\sqrt{1+\pi^2\left(r_1^2+r_2^2\right)\left(T_L^2+T_R^2\right)} = 2\pi T\cosh\Sigma\left(1+\frac{\pi^2}{2}\left(r_1^2+r_5^2\right)\left(T_L^2+T_R^2\right)+\ldots\right). \tag{4.17}$$

The second equality (expansion in $r_0^2/\sqrt{r_1^2 + r_5^2}$) is the dilute-gas approximation. Importantly, the Lyapunov exponent *does not repeat the universal* $2\pi T$ *("fake MSS") result.* It depends on r_1 and r_5 in addition to T, and its temperature dependence is a nonlinear function. But the leading term in the expansion has a simple form:

$$\lambda_L^{(0)} \approx \frac{r_0}{r_1 r_5} = 2\pi T\cosh\Sigma. \tag{4.18}$$

Therefore, *the Lyapunov exponent in the dilute-gas regime "comes close" to the static value but differs by a factor of* $\cosh\Sigma$ *which equals unity when* $\Sigma = 0$*, i.e. when there is no rotation.* In absence of rotation we return to the $2\pi T$ exponent in the dilute-gas regime.

We can translate our result into the standard variables for rotating BTZ solutions. Since in standard coordinates for BTZ black holes we have $\Omega = w_-/Lw_+$, using eq. (4.8) it follows that $L\Omega = \tanh\Sigma$. Therefore, using the identity $\cosh\Sigma = 1/\sqrt{1-\tanh^2\Sigma}$, we get

$$\lambda_L^{(0)} = \frac{2\pi T}{\sqrt{1 - L^2\Omega^2}}, \quad L\Omega \in [0, 1). \tag{4.19}$$

We could express this result in terms of the left and right temperature $T_{L,R}$, making use of the relation $2/T = 1/T_L + 1/T_R \;\Rightarrow\; T = 2T_L T_R/(T_L + T_R)$. However, we do not get

[11] Again, a more general open string setup would not necessarily be integrable — one has to perform the Kovacic analysis for every boundary condition (i.e. effective Lagrangian) separately.

[12] One may worry whether this expression remains finite in the near-extremal limit where we take $\Sigma \to \infty$. We should pay attention to the fact that there is a factor of r_0 hiding inside the temperature T. In the near-extremal limit we also take a limit $r_0 \to 0$, while keeping $r_0\cosh\Sigma$ fixed.

JHEP04(2024)025

a particularly simple or more intuitive form than (4.19), which in fact nicely shows how a nonzero rotation rate Ω deforms us away from the universal $2\pi T$ scaling.

This result should be compared to the ones found in [73, 74], where chaos in dual CFT was studied by calculating the OTOC correlators of rotating BTZ black holes for a scalar field and for a probe string respectively. The calculation done in [73] obtains two different Lyapunov exponents $\lambda_L^{\pm} = 2\pi T/(1 \mp L\Omega)$ in the presence of rotation, one of which is above the MSS bound and the other one bellow it, presuming that $\Omega \neq 0$. Our result (4.19) turns out to be exactly equal to the geometric mean of $\{\lambda_L^+, \lambda_L^-\}$, implying that $\lambda_L^- < \lambda_L < \lambda_L^+$. Both results show that when an additional scale (angular velocity) appears there is no single "degenerate" exponent anymore, but different response functions receive different corrections.

We note in passing that our near-horizon analysis yields a single Lyapunov exponent, rather than a Lyapunov spectrum with two (in general different) exponents as one would expect in this background (and as [73] finds in the rotating BTZ case) — rotation breaks isotropy so the two directions normal to the invariant plane should be inequivalent. The reason that we nevertheless only see a single exponent could be that the quanta of p-momentum in D1-D5-p are only left-moving, thus we only see the Lyapunov exponent associated with the temperature of the left-moving modes.

The opposite limit when $r \gg r_0, r_0 \cosh \Sigma$ and $r \gg r_1, r_5$, is treated in the same way as the asymptotically flat limit of the interpolating geometry in subsubsection 3.2.3: we have noted that we can think of the six-dimensional black string as an interpolation between $AdS_3 \times \mathbb{S}^3$ and Minkowski spacetime. The far region corresponds to the latter, hence it must have zero Lyapunov exponent.

Unlike the examples from previous sections, we have now found some unexpected aspects of the bulk Lyapunov exponent: dependence on the rotation rate and the complex temperature dependence away from the dilute-gas limit.[13] Now we will relate it to the retarded propagator of a CFT quasiparticle interacting with the thermal ensemble,[14] the natural dual object to consider.

4.3 Transverse fluctuations

Now we want to study the retarded Green's function for transverse fluctuations, which describes thermal motion of quasiparticles in D1-D5 field theory, the more intuitive object to consider compared to the radial fluctuation. In this case, it is convenient to switch to the Nambu-Goto formalism and work in the static gauge. A similar calculation was already done in a slightly different setup [75], where the authors study the bulk dynamics of a fundamental string in an extremal and near-extremal Reissner-Nordström (RN) black hole background. Of course, the D1-D5 background will give very different physics.

[13] There is of course no rigorous reason for the bulk exponent to obey the MSS bound in all cases as it is a different object, and comparing to [73] we have seen that even though the OTOC exponent also changes in the presence of rotation the values are different. But still, the fact that (4.17)–(4.18) differ from the results like [73] suggests there is a difference in underlying physics.

[14] In the context of D1-D5 CFT it does not make much sense to talk about quarks as the symmetries of the theory differ from $\mathcal{N} = 4$ SYM.

JHEP04(2024)025

The ansatz is now:

$$t(\tau,\sigma)=\tau\equiv t,\quad R(\tau,\sigma)=\sigma\equiv r,$$
$$\Psi(\tau,\sigma)\equiv\psi(t),\quad \Theta(\tau,\sigma)\equiv\pi/2,\quad \Phi(\tau,\sigma)\equiv\phi(t),\quad X_5(\tau,\sigma)\equiv X(t,r). \tag{4.20}$$

We expand $X(t,r)$ in Fourier modes

$$X(t,r)=\int\frac{d\omega}{2\pi}e^{-i\omega t}X_\omega(r), \tag{4.21}$$

and the relevant equation of motion obtained by varying the Nambu-Goto action reads

$$X''_\omega(r)+\left(\frac{r_0^2\left(-3r^2+r_0^2+(r^2-r_0^2)\cosh^2(2\Sigma)\right)}{r\left(r^2-r_0^2\right)\left(-2r^2+r_0^2+r_0^2\cosh^2(2\Sigma)\right)}-\frac{f'(r)}{f(r)}+\frac{h'(r)}{2h(r)}\right)X'_\omega(r)$$
$$-\frac{2r^2\omega^2 f(r)}{\left(-2r^2+r_0^2+r_0^2\cosh^2(2\Sigma)\right)h(r)}X_\omega(r)=0. \tag{4.22}$$

In the special case when there is no rotation ($\Sigma=0$) this equation simplifies to

$$X''_\omega(r)+\left(\frac{r_0^2}{r^3h(r)}-\frac{f'(r)}{f(r)}+\frac{h'(r)}{2h(r)}\right)X'_\omega(r)+\frac{\omega^2 f(r)}{h^2(r)}X_\omega(r)=0. \tag{4.23}$$

We will first solve the special case with no rotation; it will give us some useful prior intuition for the general case. Since the problem can be divided into two regions, we will again employ the matching procedure in order to gain some analytic control of the equation.

4.3.1 Static AdS: extremal case

Consider first the near-horizon region of the extremal black string, i.e. at temperature $T=0$ on the field theory side. In this case the IR geometry is given by eqs. (4.6). The relevant equation of motion for string fluctuations along the x_5-direction in this regime is

$$X''_\omega(r)+\frac{4}{r}X'_\omega(r)+\left(\frac{L^2\omega}{r^2}\right)^2X_\omega(r)=0, \tag{4.24}$$

with general solutions of the form

$$X_\omega(r)=\mathcal{A}\left(1-\frac{iL^2\omega}{r}\right)e^{\frac{iL^2\omega}{r}}+\mathcal{B}\frac{1}{2L^4\omega^2 r}\left(1-\frac{ir}{L^2\omega}\right)e^{-\frac{iL^2\omega}{r}}. \tag{4.25}$$

Imposing the infalling boundary condition (appropriate for the retarded propagator) at the horizon requires $\mathcal{B}=0$. Expanding this solution in the matching region $r_0\ll r\ll L$, we get

$$X_\omega(r)=\mathcal{A}\left(1+\frac{(L^2\omega)^2}{r^2}\right). \tag{4.26}$$

From this we can calculate the retarded Green's function at $T=0$ in the IR region $r_0/r,\omega L\ll 1\ll L/r$:

$$\mathcal{G}_R^{(T=0)}=L^4\omega^2\Rightarrow\Im\mathcal{G}_R^{(T=0)}=0. \tag{4.27}$$

JHEP04(2024)025

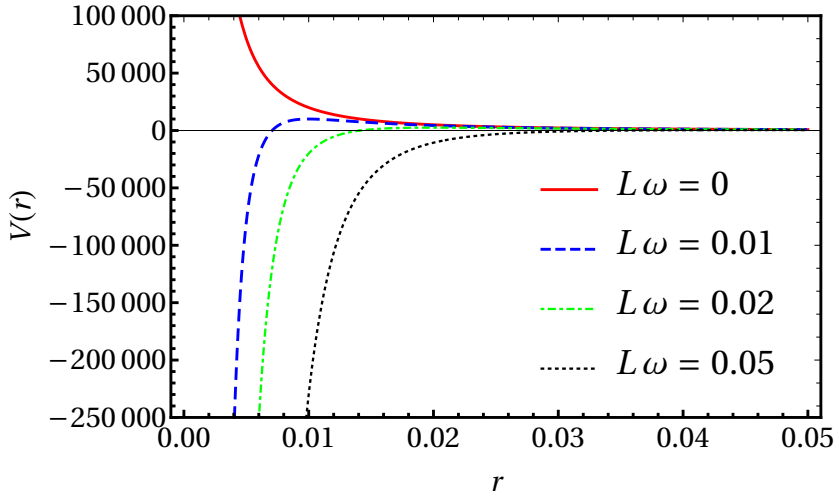

Figure 2. The effective Schrödinger potential (4.28) for the extremal D1-D5 geometry with $L = 1$, for four values of the frequency ω. The static case $\omega = 0$ (red full line) is qualitatively different because the potential is strongly repulsive: there is no absorption because plan waves coming from infinity are reflected away. For $\omega > 0$ (blue, green, black dotted lines) the potential is strongly attractive, diverging as $1/r^4$ at the origin $r = 0$. This again implies zero absorption cross section as there are no solutions behaving as plane waves at infinity.

Therefore, we get a vanishing absorption cross-section in the presence of the horizon, i.e. $\Im\mathcal{G}_R^{(T=0)} = 0$. So we need to understand why the extremal horizon does not absorb anything even though it is a horizon (with finite area and finite greybody factor). From the bulk viewpoint, one way to see the reason is to rewrite the fluctuation equation (4.24) in the Schrödinger form:

$$\partial_r^2 \widetilde{X}_\omega(r) - V_{\text{eff}}(r)\widetilde{X}_\omega(r) = 0, \quad V_{\text{eff}}(r) = \frac{2r^2 - L^4\omega^2}{r^4}. \tag{4.28}$$

The effective potential is shown in figure 2 for various values of ω. For $\omega = 0$ a zero imaginary part could be expected — for $\omega = 0$ the effective potential is positive and (quadratically) divergent at the horizon, thus there is no absorption, i.e. all incoming waves are reflected backward.

The nonstatic case $\omega \neq 0$ is qualitatively different — it has the expected negative divergence (infinite well) at the extremal horizon $r \to 0$, as we see from eq. (4.28) and figure 2. However, it is known that the scattering problem for attractive central potentials diverging as $1/r^s$ for $s > 2$ is not well-defined [76]: such potentials always lead to a wave "falling toward the center" and the solution to the Schrödinger equation in this case is always localized around zero — there is no absorption because the infalling plane wave at infinity is not a consistent boundary condition. We will see in the following section that we can infer this result for the retarded Green's function in the extremal case by considering the limit $\omega \ll T$ of the thermal correlator obtained in a near-extremal case.

4.3.2 Static BTZ: near-extremal case

At low but finite temperatures or equivalently in the near-extremal case we would be interested in the dynamics of the open string in the metric given by eq. (4.7). Therefore, we look for

JHEP04(2024)025

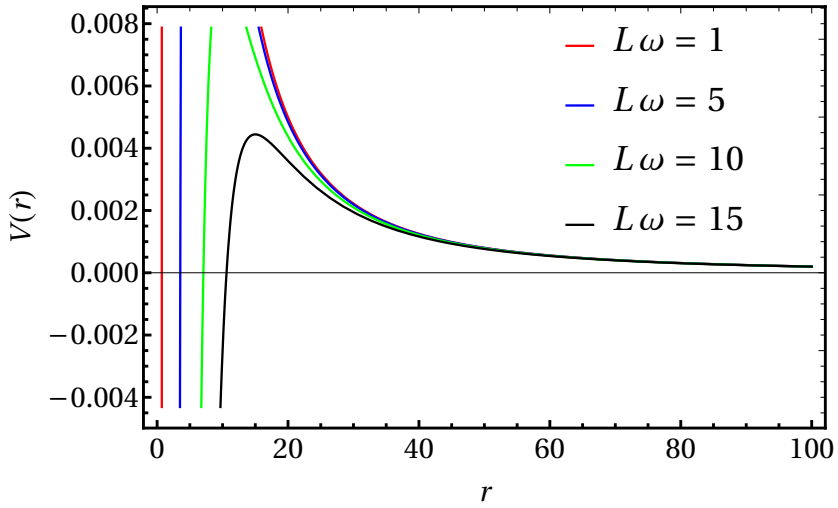

Figure 3. The effective Schrödinger potential (4.30) for a near-extremal D1-D5-p system with the parameters $r_0 = 0.1,\ L = 1$, for $L\omega = 1, 5, 10, 15$ (red, blue, green, black). Already from the expression in eq. (4.30) it is obvious that in the near-extremal case nothing special happens in the static limit $\omega = 0$. For all frequencies, the potential has the form typical of near-horizon effective potentials [68, 70], where a high but finite potential barrier is followed by the infinite well at the horizon $r = r_0$.

the solution of open string equations in BTZ×$\mathbb{S}^3$ geometry but (in this subsection) still with no rotation ($\Sigma = 0$). The relevant equation can be written in a compact form reminiscent of the relativistic wave equation in curved background:

$$\frac{h(r)}{r^4}\frac{d}{dr}\left(h(r)r^4\frac{dX_\omega(r)}{dr}\right) + \frac{L^4\omega^2}{r^4}X_\omega(r) = 0. \tag{4.29}$$

It is again instructive to look at the Schrödinger form of the equation, obtained by plugging in $X_\omega(r) = h^{-1/2}(r)r^{-2}\Psi(r)$ into eq. (4.29):

$$\left(\frac{d^2}{dr^2} - V_{\text{eff}}(r)\right)\Psi(r) = 0, \quad V_{\text{eff}}(r) = \frac{2r^2 - 3r_0^2 - L^4\omega^2}{\left(r^2 - r_0^2\right)^2}. \tag{4.30}$$

The second term inside the brackets is the effective Schrödinger potential, plotted in figure 3.

Proceeding further toward the analytic solution to eq. (4.29) it is convenient to transform the radial variable as

$$\zeta \equiv \frac{r_0^2}{r^2}. \tag{4.31}$$

In order to reduce eq. (4.29) to a hypergeometric differential equation,[15] we will make a further coordinate transformation $\zeta \mapsto 1 - \xi$. The equation now reads

$$X''_\omega(\xi) - \frac{1}{2\xi}\frac{2-\xi}{1-\xi}X'_\omega(\xi) + \frac{1}{\xi^2(1-\xi)}\left(\frac{L^2\omega}{2r_0}\right)^2 X_\omega(\xi) = 0. \tag{4.32}$$

[15]Since eq. (4.29) has three regular singular points at $r = 0,\ r_0$ and ∞, we can be sure that it can be written in the form of the hypergeometric differential equation.

JHEP04(2024)025

We can solve this equation at the horizon $\xi = 0$, by making the substitution $y = -\log \xi$ in eq. (4.32). The solution at the horizon takes the form $X_\omega \sim e^{\pm i\alpha y} = \xi^{\pm i\alpha}$, with $\alpha = L^2\omega/2r_0$. The boundary condition at the horizon requires the outgoing modes to vanish, yielding

$$X_\omega(\xi) = \widetilde{\mathcal{A}}\, \xi^{-i\alpha}. \tag{4.33}$$

In order to get the full near-horizon solution, we plug the ansatz $X_\omega(\xi) = \xi^{-i\alpha} F(\xi)$ into eq. (4.32), yielding

$$\xi(1-\xi)\frac{d^2F}{d\xi^2} + \left[1 - 2i\alpha - \left(1 - i\alpha - \frac{1}{2} - i\alpha\right)\xi\right]\frac{dF}{d\xi} - (-i\alpha)\left(-\frac{1}{2} - i\alpha\right)F(\xi) = 0. \tag{4.34}$$

We recognize eq. (4.34) as the hypergeometric equation with parameters

$$a = -i\alpha, \quad b = -\frac{1}{2} - i\alpha, \quad c = 1 - 2i\alpha. \tag{4.35}$$

The corresponding regular solution reads

$$F(\xi) = \widetilde{\mathcal{A}}\; {}_2F_1\left(a, b, c; \xi\right) + \widetilde{\mathcal{B}}\; \xi^{2i\alpha}\; {}_2F_1\left(a + 1 - c, b + 1 - c, 2 - c; \xi\right). \tag{4.36}$$

We impose the infalling boundary condition (4.33) at the horizon, implying that $\widetilde{\mathcal{B}} = 0$, thus the near-horizon solution becomes

$$X_\omega(\xi) = \widetilde{\mathcal{A}}\; \xi^{-i\alpha}\; {}_2F_1\left(a, b, c; \xi\right). \tag{4.37}$$

We can now use the following identity to express solution (4.37) in terms of functions depending on ζ, instead of $\xi = 1 - \zeta$:

$$\begin{aligned} {}_2F_1\left(a, b, c; \xi\right) = {} & \frac{\Gamma(c)\Gamma(c-a-b)}{\Gamma(c-a)\Gamma(c-b)}\; {}_2F_1\left(a, b, 1 + a + b - c; \zeta\right) + \\ & + \frac{\Gamma(c)\Gamma(a+b-c)}{\Gamma(a)\Gamma(b)} \zeta^{c-a-b}\; {}_2F_1\left(c - a, c - b, 1 + c - a - b; \zeta\right). \end{aligned} \tag{4.38}$$

The matching region $r_0 \ll r$ corresponds to $\zeta \ll 1$, so we expand eq. (4.38) in small ζ:

$${}_2F_1\left(a, b, c; \xi\right) \approx \frac{\Gamma(c)\Gamma(c-a-b)}{\Gamma(c-a)\Gamma(c-b)} + \frac{\Gamma(c)\Gamma(a+b-c)}{\Gamma(a)\Gamma(b)} \zeta^{c-a-b}. \tag{4.39}$$

We observe that the full solution in the matching region is of the form

$$X_\omega(r) \propto \widetilde{\mathcal{S}}\; r^{-d+\Delta} + \widetilde{\mathcal{F}}\; r^{-\Delta}, \quad d = \Delta = 3, \tag{4.40}$$

which allows us to read off the retarded Green's function as the ratio $\widetilde{\mathcal{F}}/\widetilde{\mathcal{S}}$:

$$\mathcal{G}_R^{(T)}(\omega) \propto \frac{\Gamma(c-a)\Gamma(c-b)}{\Gamma(a)\Gamma(b)} = \frac{\Gamma\left(1 - i\frac{\omega}{2\lambda_L}\right)\Gamma\left(\frac{3}{2} - i\frac{\omega}{2\lambda_L}\right)}{\Gamma\left(-i\frac{\omega}{2\lambda_L}\right)\Gamma\left(-\frac{1}{2} - i\frac{\omega}{2\lambda_L}\right)}. \tag{4.41}$$

We can take the imaginary part of (4.41) to get the absorption cross-section:

$$\sigma_{\text{abs}} = \Im\mathcal{G}_R^{(T)}(\omega) \propto \frac{\alpha}{4} + \alpha^3, \quad \alpha = \frac{\omega}{2\lambda_L}, \quad \lambda_L = 2\pi T. \tag{4.42}$$

This is the central result of our calculation — the IR propagator and the absorption cross section for a heavy quasiparticle excitation. Let us think what this result means:

JHEP04(2024)025

1. The only energy scale in the Green's function is the temperature. This is in line with the problem of drift of a heavy quark through neutral $\mathcal{N} = 4$ super-Yang-Mills (SYM) plasma, dual to a dragging string in AdSS background [38, 39, 77] and many subsequent works in the same setup [78–82]: in this case the quasiparticle does not see the charges of the D1-D5-p system.[16] This can be ascribed to the fact that the additional charges of the D1-D5-p system are global and the quasiparticle is neutral with respect to them.

2. The form of the propagator (eq. (4.41)) could be expected from the BTZ asymptotics of the near-extremal geometry [83], as it has the form of conformal quantum mechanics, i.e. 0+1-dimensional CFT [84] (we know that in the near-horizon region of the BTZ geometry the transverse spatial coordinate decouples and the geometry becomes $\mathrm{AdS}_2 \times \mathbb{S}$, so that AdS_2 gives the 0+1-dimensional CFT).

3. The imaginary part behaving as $\sim \omega + \omega^3$ suggests that in addition to the usual drag force $f \propto \dot{x}$ we also have a third-order term $\tilde{f} \propto dx^3/dt^3$. This is in fact expected — all odd-power terms[17] in velocity are allowed symmetry-wise and the leading-order holographic Green function already captures the first two terms.

4. This result could not be reproduced neither from the static limit ($\omega = 0$) nor from the extremal limit $T = 0$ — these two limits are singular, which is expected for the static limit but somewhat strange for the extremal limit.

As a sanity check we consider the high-frequency limit $\omega \gg T$ where one should recover the result for the extremal case.[18] In this limit we can compare our calculation to the pure CFT result for the two-point correlation function. We consider a two-point correlation function in a $2+1$-dimensional CFT for an operator with scaling dimension Δ: this behaves as $\langle \mathcal{O}_\Delta(t)\mathcal{O}_\Delta(0)\rangle \sim |t|^{-2\Delta}$, i.e. $\sim \omega^{2\Delta-d}$, where d is the spacetime dimensionality. For an operator with a scaling dimension $\Delta = 3$ living in $d = 3$ spacetime dimensions, one should indeed expect $\sim \omega^3$ power-law behavior of the thermal correlator in the high-frequency limit.

4.3.3 Rotating BTZ: near-extremal case

Now we study the rotating BTZ black hole. Compared to the static case, it is considerably more difficult for calculations. Conceptually, it is also distinct for having different left and right temperature. Now we cannot write an analytic solution in the whole throat, all the way to the AdS boundary (i.e., the throat of the D1-D5-p geometry, before the far-region flat asymptotics kick in), akin to eq. (4.37). Instead, we can only treat the near-horizon limit, when $r \to r_h$ or equivalently $\zeta \to 1$ (for ζ as defined in eq. (4.31)).

[16] At least, this is the case in our current setup with no drift; it would be interesting to check if this conclusion remains in force in presence of drift.

[17] Even-power terms (like $\dot{x}^2$) are not expected as their sign is independent of the sign of velocity, i.e. a proper drag force (opposing the motion) would have to look like $-\dot{x}^2 \mathrm{sgn}\dot{x}$ but that implies the breaking of some discrete symmetry which we do not have.

[18] In this limit we consider wavelengths well below T^{-1} ($\omega^{-1} \ll T^{-1}$) that are insensitive to thermal fluctuations and thus resemble the behavior for the extremal background geometry.

JHEP04(2024)025

The equation of motion for the transverse fluctuations (4.22) can be slightly rewritten as

$$\left(1-\frac{r_0^2}{r^2}\right)\left(1-\frac{r_0^2+r_n^2}{r^2}\right)X_\omega''(r)+\frac{4}{r}\left[1-\frac{3}{2}\left(1-\frac{r_0^2}{3r^2}\right)-\frac{5}{4}\left(1-\frac{2}{5}\frac{r_0^2}{r^2}\right)\right]X_\omega(r)+\frac{L^4\omega^2}{r^4}X_\omega(r)=0. \tag{4.43}$$

Now we perform the same change of variables as before, $y=-\log\xi=-\log\left(1-r_0^2/r^2\right)$, so that $y\to\infty$ at the horizon. Expanding the coefficients to order ξ^0 for ξ small or equivalently to order $1=(e^{-y})^0$ for y large, we get the near-horizon limit of (4.43):

$$\left(1+\frac{2r_n^2}{r_0^2}-e^y\frac{r_n^2}{r_0^2}\right)X_\omega''(r)+e^y\frac{r_n^2}{2r_0^2}X_\omega'(r)+\frac{L^4\omega}{4r_0^2}X_\omega(r)=0. \tag{4.44}$$

The solution that satisfies the infalling boundary condition at the horizon is

$$X_\omega(y)\sim e^{i\delta y}\ {}_2F_1\left(i\delta,-\frac{1}{2}+i\delta,1+2i\delta;\frac{e^y r_n^2}{r_0^2+2r_n^2}\right),\quad \delta=\frac{L^2\omega}{2\sqrt{r_0^2+2r_n^2}}. \tag{4.45}$$

Another way to understand the fact that in the presence of rotation the solution of this type cannot exist without imposing some approximations is that hypergeometric functions are the representations of $\mathrm{SL}(2,\mathbb{R})$ which is broken by rotation.

In order to obtain the IR propagator (now we cannot obtain analytically the propagator for general ω values), we expand the above solution in the region far from the horizon, for $r\gg r_0$, that is for y small. Using the identity (4.39) this yields

$${}_2F_1\left(i\delta,-\frac{1}{2}+i\delta,1+2i\delta;\frac{e^y r_n^2}{r_0^2+2r_n^2}\right)\sim\frac{\Gamma\left(\frac{3}{2}\right)\Gamma(1+2i\delta)}{\Gamma(1+i\delta)\Gamma\left(\frac{3}{2}+i\delta\right)}+\frac{\Gamma\left(1+2i\delta\right)\Gamma\left(-\frac{3}{2}\right)}{\Gamma(i\delta)\Gamma\left(-\frac{1}{2}+i\delta\right)}\left(\frac{r_0}{r}\right)^3. \tag{4.46}$$

Identifying the leading term and subleading term as the source and response respectively we compute the retarded Green's function in the rotating case:

$$\mathcal{G}_R^{(T)}(\omega)\sim\frac{\Gamma(1-i\delta)\Gamma\left(\frac{3}{2}-i\delta\right)}{\Gamma(-i\delta)\Gamma\left(-\frac{1}{2}-i\delta\right)} \tag{4.47}$$

It has the same form as the one that we have obtained in previous section in the absence of rotation (4.41), but with a different λ_L scale compared to eq. (4.18):

$$\lambda_L^{(\mathrm{mod})}=2\pi T\cosh\Sigma\sqrt{1+\frac{2r_n^2}{r_0^2}}=\lambda_L^{(0)}\sqrt{\cosh(2\Sigma)},\quad \delta=\frac{\omega}{2\lambda_L^{(\mathrm{mod})}}. \tag{4.48}$$

We can interpret this as a modification of energy in the presence of a rotating horizon, i.e. the Lense-Thirring effect.

4.4 Quasinormal modes and their decay scale

So far, we have found that breaking a global symmetry in IR (introducing rotation) in general influences the bulk instability scale differently from the way it influences the exponent of the field-theory OTOC. We have likewise seen that UV deformations (full brane geometry

JHEP04(2024)025

deforming the AdS throat) also change the instability scale away from $2\pi T$. It remains unclear however what exactly the bulk scale is from the CFT viewpoint, and to understand this we will relate the bulk instability exponent to the quasinormal mode frequencies. For simplicity we will consider the non-rotating case but all the results that we obtain still hold also in the presence of rotation with $\lambda_L \to \lambda_L^{(\mathrm{mod})}$.

Let us first remember that the poles in the retarded Green's function are related to transport properties of a thermal field theory. On the gravity side, they correspond to a spectrum of quasinormal modes [68, 70]. More specifically, the relaxation times in field theory are given by the imaginary part of the QNM spectrum in the bulk [85, 86]. Since our retarded Green's function (4.41) is singular at an infinite number of points in the complex plane, due to the presence of the gamma functions in the numerator, we can extract the whole QNM spectrum from it. Singular points are given by $c-a=-n$ or $c-b=-n$, for $n\in\mathbb{Z}^+$ (a set of non-negative integers), thus $\omega_n=-2i(n+1)\lambda_L$ or $\omega_n=-2i(n+3/2)\lambda_L$. The union of the two sets yields the following spectrum:

$$\omega_{\mathfrak{n}}=-2i(\mathfrak{n}+1)\lambda_L,\quad \mathfrak{n}=0,\frac{1}{2},1,\frac{3}{2},\cdots \tag{4.49}$$

or equivalently

$$\omega_{\mathfrak{m}}=-i(\mathfrak{m}+1)\lambda_L,\quad \mathfrak{m}=1,2,3,\cdots . \tag{4.50}$$

We write the solution in these two obviously equivalent ways in order to facilitate the comparison with the literature.[19]

Another way to derive the QNM spectrum is by definition, as the eigenfrequencies of the equations of motion with infalling boundary conditions at the horizon and Dirichlet boundary conditions at the boundary. The latter require the solution at AdS boundary to vanish.[20] The equivalence of the two approaches should be obvious, since the same set of requirements that force the solution (4.39) to vanish at infinity also describes the poles of the retarded Green's function (4.41). This gives us a more intuitive picture of QNM: they tell us how a local near-horizon instability decays. Therefore, we can think of the inverse of the Lyapunov exponent λ_L^{-1} as some characteristic timescale for the decay of perturbations along the open string, that has nothing to do with chaos.

The result summarized in eqs. (4.49)–(4.50) is qualitatively the same as the one obtained in [85] for scalar perturbations in a nonrotating BTZ black hole background, except that the spectrum (4.50) also includes half-integer values of $\mathfrak{n}$ (which is simply due to different objects being considered: strings vs. scalar field). Similar scaling of the QNM spectrum with the Lyapunov exponent of some special orbit is known from two classic papers concerning *asymptotically planar* black holes:

[19] The form (4.50) is simpler and more natural but (4.49) has the same form as the scalar QNM solution [85] that we want to benchmark against.

[20] In this context we again ignore the asymptotically flat region of the D1-D5-p geometry and only consider its interior and AdS throat, just as we did when solving the string equations of motion. In an asymptotically Minkowski spacetime we would require outgoing boundary condition at infinity, very different from the situation in AdS. This will be important in what follows.

JHEP04(2024)025

1. In [47], the imaginary part of the QNM frequencies is determined by the instability of geodesic motion, i.e. the Lyapunov exponent of a massless particle *on the photon sphere*, which acts as an unstable fixed point. This is obtained in the eikonal approximation when $\Re\omega \gg \Im\omega$.[21]

2. In the opposite, high-overtone or overdamped regime, when $\mathfrak{n} \gg 1$ and thus $\Re\omega \ll \Im\omega$, [50] find that $\Im\omega$ is proportional to the surface gravity at the horizon, which equals precisely $2\pi T$.

Our results are clearly obtained in the high-overtone regime since our Green's functions satisfy $\Im\mathcal{G}_R^{(T)} \gg \Re\mathcal{G}_R^{(T)}$. Therefore, our result essentially generalizes [50] for an open string in AdS. Yet, the coefficient itself is obtained as the Lyapunov exponent of an unstable fixed point, and in that sense generalizes also [47] from the eikonal (photon-sphere dominated) regime to the high-overtone (horizon-dominated) regime.

We have thus shown that both "easy" regimes ($l \gg 1$ and $\mathfrak{n} \gg 1$) can be understood from classical unstable saddle points, but of course the eikonal regime sees the scattering near the photon sphere while the overdamped regime (our case) sees the horizon. In this sense, earlier results on the universal $2\pi T$ exponent for geodesics and fields near-horizon [31], bringing the conclusion about the horizon as the "nest of chaos", are not in collision with the studies of the instability on the photon sphere [47, 87, 88] — only that they correspond to different regimes. It is somewhat surprising that for a special string configuration these results are obtained in asymptotically AdS backgrounds, as it is well known and discussed already in [47, 50] that for a geodesic the argument does not easily generalize to AdS asymptotics.

Finally, we should also comment on the field theory interpretation of the quasinormal modes spectrum that we have just found in the bulk. We already mentioned that an open string in the bulk stretched from the boundary to the thermal AdSS horizon corresponds to a heavy quark in thermal plasma of super-Yang-Mills quarks and gluons. Perturbations along the string describe thermal perturbations in the plasma. Similar holds in the D1-D5 CFT except that the elementary excitations now cannot be called quarks. We can summarize the findings above by noting that a Lyapunov exponent is really related to the QNM frequencies, which describe how local near-horizon instabilities on the string decay. Decay rates of those instabilities are given by the spectrum of quasinormal modes, so on the field theory side they describe how the thermal fluctuations in plasma die off. Thus, they predict the thermalization timescale in the dual CFT.

5 Discussion and conclusions

The initial motivation for this work was a rather technical question: what is the meaning of bulk chaos in particle and string motion in AdS spaces, and why it typically saturates the same universal chaos bound as OTOC in field theory. We were led to the study of open strings (rather than ring strings or particle geodesics) largely by reasons of calculational simplicity and direct CFT interpretation: a string with one end on the boundary and the

[21] Here $\Re\omega$ denotes the orbital frequency (oscillations) and $\Im\omega$ is the Lyapunov exponent for the unstable geodesic orbit (damping).

JHEP04(2024)025

other in the interior describes the motion of a heavy quark in quark-gluon plasma. The holographic interpretation is less obvious for other string configurations, and for geodesics it corresponds to a rather special, high-conformal-dimension limit.

As usual, the chase is almost better than the catch. We have found a number of surprising properties of bulk dynamics, first and foremost the horizon as an unstable saddle point and the "fake nest of chaos" with local instability rate exactly equal to $2\pi T$ in the static case but different from it in the rotating black string geometry. But the holographic interpretation is equally interesting: the universal MSS-like exponent is a red herring, the artifact of the large-N limit in field theory, i.e. classical bulk dynamics, when temperature is the only scale, unless some additional symmetry is explicitly broken in IR. This happens in the D1-D5-p black string, where the rotation breaks the symmetry between left- and right-moving modes. Just like in [89], the rotating system deforms away from the universal $2\pi T$ exponent, and this shows directly in the correlation functions. We also note that away from the dilute gas approximation there are additional higher-order temperature corrections to the Lyapunov exponent — this is the effect of the UV deformation.

We have found the connection between the near-horizon Lyapunov exponent and the spectrum of quasinormal modes in the high-overtone regime. This gives us an important hint about the meaning of the bulk Lyapunov exponent: it is an instability scale associated to the decay of fluctuations along the string due to thermal dissipation, and has nothing to do with bulk chaos. This resembles two classic results on quasinormal modes of asymptotically flat black holes: in the eikonal regime the Lyapunov exponent on the photon sphere determines the quasinormal mode [47], whereas in the overdamped regime (our case) the imaginary part of the quasinormal mode equals the horizon surface gravity [50]. We have essentially shown that for near-horizon string orbits the bulk Lyapunov exponent equals the surface gravity (which generalizes even for a rotating horizon).

Motivated by this connection, one could try to extend some other known results on geodesic instabilities to the orbits of extended objects like strings. Of primary interest is the instability on the photon sphere which, apart from the well-known connection with quasinormal modes, holds the key to several other properties both in asymptotically flat and in global AdS spaces [90, 91]. However, our setup needs to be substantially modified to study the photon sphere, which arises as the locus of unstable saddle points for null geodesics *arriving from infinity*. An open string in our configuration does not even have a saddle point on the photon sphere, i.e. one cannot even define the Lyapunov exponent on the photon sphere unambiguously. Therefore, instead of having a static string, we would need to scatter an open string along a null geodesic. In that case one would expect the minimal allowed value for the impact parameter to be of order of the photon sphere size (analogous study for massless particles is performed in [48]). Such a setup is particularly suitable for the study of fuzzballs and microstate geometries, since they have no sharp length/energy scale analogous to a horizon [87, 92]. We would then be probing another branch of the QNMs spectrum, associated to stringy instabilities around the photon sphere.

One might find it surprising that our open string lives in an integrable sector. This is likely a consequence of the highly symmetric and simple boundary conditions for which we prove integrability: a static string at the horizon. It is known that a ring string is nonintegrable in thermal backgrounds, and also in generic Dp-brane backgrounds (although some very special cases can be integrable, even at finite temperature, see e.g. [93, 94]). A

JHEP04(2024)025

more generic open string configuration is likely also nonintegrable. Essentially, since *different boundary conditions for string motion result in a different effective Lagrangian, the Liouville integrability has to be checked separately for every configuration.* While *physically* we like to think of "string motion in a given background", mathematically the system is integrable if the Euler-Lagrange equations satisfy certain conditions — and for a string the form of these equations depends on the string ansatz. Therefore, while a single example is enough to prove general nonintegrability, proving integrability in the most general case requires more powerful tools than the Kovacic algorithm. We do not do that: we merely focus on a single case which turns out to be integrable.

From our results it is clear that the study chaos and scrambling in gauge/string duality (i.e., beyond classical gravity) is a separate topic, not much touched upon in this work. Fluctuations of a static straight string stretched from boundary to boundary of a maximally extended (static and neutral) BTZ black hole are known to lead to the exact MSS value for the worldsheet OTOC [21]; for a dragging string, butterfly velocity also enters the picture, as the leading correction to the drag force [95]. Given the high symmetry of these systems, this is not surprising; when the symmetry is decreased or corrections added to the classical string solution the value will be modified but there is no reason to believe that the solutions and the OTOC exponents will be modified in the same way as the bulk exponents, i.e. quasinormal modes in our setup. Worldsheet scrambling for a rotating BTZ black hole was studied in [74] and indeed, while the OTOC exponent is modified from the MSS value, it is not the same as the bulk exponent that we find here. Of course, strings can also model spatiotemporal chaos if we allows both worldsheet coordinates to fluctuate as in [96].

Finally, the issue of gauge choice might be worth commenting. Our choice to work in the conformal gauge instead of static gauge most of the time is somewhat unusual. The static gauge equates the time and radial coordinate with the worldsheet coordinates τ and σ and thus immediately kills the unphysical (gauge-dependent) degrees of freedom. But the conformal gauge has several advantages for us: (*i*) it simplifies many calculations (*ii*) it allows us to look at the fluctuations along the holographic RG flow (the radial direction) (*iii*) it does not fully fix the reparametrization invariance on the worldsheet, leaving the $\mathrm{SL}(2,\mathbb{R})$ group of global coordinate transformations, but as argued in [45, 46, 97] this group provides a nice way to understand the appearance of a universal scale and its disappearance when we determine the boundary conditions for the transverse fluctuations that fully fix the gauge on the worldsheet. This approach was exploited in full depth in [97] to study quantum chaos, i.e. OTOC on the worldsheet of the open string.

5.1 Note added: quasi-normal modes, variational equations and the spectral form factor

At the end we want to comment on another connection between our calculation and the quasi-normal modes of the black hole (or black string) background. After finishing the first version of the paper we became aware of the work [98] where it is shown that the partition function and the spectral form factor of a holographic theory at finite temperature can be understood as a product over the QNM frequencies ω_{QNM} of the bulk black hole. Specifically, for a bosonic system at temperature T, one-loop partition function is found in [98] to be

$$Z = \mathrm{Tr} e^{-i\hat{\tilde{K}}T} = \prod_{\omega_{\mathrm{QNM}}} \left(1 - e^{-i\omega_{\mathrm{QNM}}T}\right)^{-1}. \tag{5.1}$$

JHEP04(2024)025

Here, $\hat{\tilde{K}}$ is the time-shift operator which acts as a boost near the horizon (where $g_{tt} \to 0$), in a complexified metric where the radial coordinate is shifted as $r \mapsto r - i\epsilon$. From (5.1), it is obvious that ω_{QNM} are just the eigenvalues of $\hat{\tilde{K}}$. But Lyapunov exponents are nothing but the eigenvalues of the Jacobian matrix of the equations of motion — in other words, they are the eigenvalues of the shift operator but now the shift is along the tangential directions in phase space. In a given background however, e.g. in a near-horizon region like the BTZ region of a near-extremal black string, one can choose the gauge so that the Jacobian *locally* (but not everywhere) coincides with the time-shift operator $\hat{K}$; the complexification to $\hat{\tilde{K}}$ then just imposes the analytic behavior at the horizon, as one normally does when computing correlation functions such as G_R from subsection 4.3.

The above discussion is obviously not rigorous. It would be interesting to formulate it in strict terms and see how much one can learn from such a viewpoint.

Acknowledgments

We are grateful to Andrei Parnachev, Jorge Russo, David Berenstein, Filip Herček and Juan Pedraza for stimulating discussions. Work at the Institute of Physics is funded by the Ministry of Education, Science and Technological Development and by the Science Fund of the Republic of Serbia. M. Č. would like to acknowledge the Mainz Institute for Theoretical Physics (MITP) of the Cluster of Excellence PRISMA+ (Project ID 39083149) for hospitality and partial support during the completion of this work.

A Slightly generalized ansatz for the Dp-brane background

Here we comment on the ansatz for the string configuration in Dp-brane backgrounds in subsection 3.2. We can have nontrivial dynamics of the string also on the k-sphere provided we impose some additional constraints which are necessary to preserve the separation of variables. For example, we can replace the ansatz from eq. (3.6) by

$$\begin{aligned} &t = t(\tau), \quad X_1 = x_1, \quad \dots \quad X_{10-k} = x_{10-k}, \\ &R = R(\sigma), \quad \Phi_1 = \Phi_1(\tau), \quad \Phi_2 = \Phi_2(\tau), \quad \Phi_3 = \phi_3, \quad \dots \quad \Phi_k = \phi_k \end{aligned} \tag{A.1}$$

Choosing $t(\tau) = \tau$ as usual, we are left with a constraint (in addition to the Virasoro constraint) coming from the above ansatz, i.e. the assumption that R only depends on σ:

$$\dot{\Phi}_1^2 + \sin\Phi_1^2 \dot{\Phi}_2^2 \equiv \ell^2, \tag{A.2}$$

where ℓ^2 is the conserved squared angular momentum on the k-sphere. The constraints decouple the dynamics of R from Φ^1 and Φ^2, so the equation of motion for R remains the same as eq. (3.7) and for Φ_1 we obtain:

$$\ddot{\Phi}_1 + \left(\dot{\Phi}_1^2 - w^2\right) \cot\Phi_1 = 0. \tag{A.3}$$

Therefore, it is possible to go for more general dynamics than in the main text, which might be of interest for some applications but is completely peripheral for our main interest in this paper.

References

[1] Y. Sekino and L. Susskind, *Fast Scramblers*, *JHEP* **10** (2008) 065 [arXiv:0808.2096] [INSPIRE].

[2] J. Maldacena, S.H. Shenker and D. Stanford, *A bound on chaos*, *JHEP* **08** (2016) 106 [arXiv:1503.01409] [INSPIRE].

[3] S.H. Shenker and D. Stanford, *Black holes and the butterfly effect*, *JHEP* **03** (2014) 067 [arXiv:1306.0622] [INSPIRE].

[4] D.A. Roberts, D. Stanford and L. Susskind, *Localized shocks*, *JHEP* **03** (2015) 051 [arXiv:1409.8180] [INSPIRE].

[5] S.H. Shenker and D. Stanford, *Stringy effects in scrambling*, *JHEP* **05** (2015) 132 [arXiv:1412.6087] [INSPIRE].

[6] J. Maldacena and D. Stanford, *Remarks on the Sachdev-Ye-Kitaev model*, *Phys. Rev. D* **94** (2016) 106002 [arXiv:1604.07818] [INSPIRE].

[7] E. Marcus and S. Vandoren, *A new class of SYK-like models with maximal chaos*, *JHEP* **01** (2019) 166 [arXiv:1808.01190] [INSPIRE].

[8] A.M. García-García, B. Loureiro, A. Romero-Bermúdez and M. Tezuka, *Chaotic-Integrable Transition in the Sachdev-Ye-Kitaev Model*, *Phys. Rev. Lett.* **120** (2018) 241603 [arXiv:1707.02197] [INSPIRE].

[9] N. Lashkari et al., *Towards the Fast Scrambling Conjecture*, *JHEP* **04** (2013) 022 [arXiv:1111.6580] [INSPIRE].

[10] A. Almheiri et al., *The entropy of Hawking radiation*, *Rev. Mod. Phys.* **93** (2021) 035002 [arXiv:2006.06872] [INSPIRE].

[11] G. Penington, S.H. Shenker, D. Stanford and Z. Yang, *Replica wormholes and the black hole interior*, *JHEP* **03** (2022) 205 [arXiv:1911.11977] [INSPIRE].

[12] A. Almheiri et al., *Replica Wormholes and the Entropy of Hawking Radiation*, *JHEP* **05** (2020) 013 [arXiv:1911.12333] [INSPIRE].

[13] D. Stanford, *More quantum noise from wormholes*, arXiv:2008.08570 [INSPIRE].

[14] P. Saad, S.H. Shenker, D. Stanford and S. Yao, *Wormholes without averaging*, arXiv:2103.16754 [INSPIRE].

[15] P. Saad, S. Shenker and S. Yao, *Comments on wormholes and factorization*, arXiv:2107.13130 [INSPIRE].

[16] J. Pollack, M. Rozali, J. Sully and D. Wakeham, *Eigenstate Thermalization and Disorder Averaging in Gravity*, *Phys. Rev. Lett.* **125** (2020) 021601 [arXiv:2002.02971] [INSPIRE].

[17] B. Mukhametzhanov, *Factorization and complex couplings in SYK and in Matrix Models*, *JHEP* **04** (2023) 122 [arXiv:2110.06221] [INSPIRE].

[18] F.S. Nogueira et al., *Geometric phases distinguish entangled states in wormhole quantum mechanics*, *Phys. Rev. D* **105** (2022) L081903 [arXiv:2109.06190] [INSPIRE].

JHEP04(2024)025

[19] M. Čubrović, *Replicas, averaging and factorization in the IIB matrix model*, *JHEP* **09** (2022) 136 [arXiv:2203.10697] [INSPIRE].

[20] A. Blommaert, L.V. Iliesiu and J. Kruthoff, *Gravity factorized*, *JHEP* **09** (2022) 080 [arXiv:2111.07863] [INSPIRE].

[21] J. de Boer, E. Llabrés, J.F. Pedraza and D. Vegh, *Chaotic strings in AdS/CFT*, *Phys. Rev. Lett.* **120** (2018) 201604 [arXiv:1709.01052] [INSPIRE].

[22] K. Hashimoto and N. Tanahashi, *Universality in Chaos of Particle Motion near Black Hole Horizon*, *Phys. Rev. D* **95** (2017) 024007 [arXiv:1610.06070] [INSPIRE].

[23] S. Dalui and B.R. Majhi, *Near horizon local instability and quantum thermality*, *Phys. Rev. D* **102** (2020) 124047 [arXiv:2007.14312] [INSPIRE].

[24] C. Núñez, J.M. Penín, D. Roychowdhury and J. Van Gorsel, *The non-Integrability of Strings in Massive Type IIA and their Holographic duals*, *JHEP* **06** (2018) 078 [arXiv:1802.04269] [INSPIRE].

[25] C. Núñez, D. Roychowdhury and D.C. Thompson, *Integrability and non-integrability in $\mathcal{N} = 2$ SCFTs and their holographic backgrounds*, *JHEP* **07** (2018) 044 [arXiv:1804.08621] [INSPIRE].

[26] M. Čubrović, *The bound on chaos for closed strings in Anti-de Sitter black hole backgrounds*, *JHEP* **12** (2019) 150 [arXiv:1904.06295] [INSPIRE].

[27] D.-Z. Ma, D. Zhang, G. Fu and J.-P. Wu, *Chaotic dynamics of string around charged black brane with hyperscaling violation*, *JHEP* **01** (2020) 103 [arXiv:1911.09913] [INSPIRE].

[28] D. Roychowdhury, *Non-integrability for $\mathcal{N} = 1$ SCFTs in 5d*, *Phys. Rev. D* **104** (2021) 086010 [arXiv:2106.10646] [INSPIRE].

[29] C. Yu, D. Chen, B. Mu and Y. He, *Violating the chaos bound in five-dimensional, charged, rotating Einstein-Maxwell-Chern-Simons black holes*, *Nucl. Phys. B* **987** (2023) 116093 [INSPIRE].

[30] P. Dutta, K.L. Panigrahi and B. Singh, *Circular string in a black p-brane leading to chaos*, *JHEP* **10** (2023) 189 [arXiv:2307.12350] [INSPIRE].

[31] D. Giataganas, *Chaotic Motion near Black Hole and Cosmological Horizons*, *Fortsch. Phys.* **70** (2022) 2200001 [arXiv:2112.02081] [INSPIRE].

[32] T. Dray and G. 't Hooft, *The Gravitational Shock Wave of a Massless Particle*, *Nucl. Phys. B* **253** (1985) 173 [INSPIRE].

[33] T. Dray and G. 't Hooft, *The Effect of Spherical Shells of Matter on the Schwarzschild Black Hole*, *Commun. Math. Phys.* **99** (1985) 613 [INSPIRE].

[34] P. Kraus, F. Larsen and S.P. Trivedi, *The Coulomb branch of gauge theory from rotating branes*, *JHEP* **03** (1999) 003 [hep-th/9811120] [INSPIRE].

[35] V. Balasubramanian and S.F. Ross, *Holographic particle detection*, *Phys. Rev. D* **61** (2000) 044007 [hep-th/9906226] [INSPIRE].

[36] J. Louko, D. Marolf and S.F. Ross, *On geodesic propagators and black hole holography*, *Phys. Rev. D* **62** (2000) 044041 [hep-th/0002111] [INSPIRE].

[37] J.G. Russo, *Anomalous dimensions in gauge theories from rotating strings in $AdS_5 \times S^5$*, *JHEP* **06** (2002) 038 [hep-th/0205244] [INSPIRE].

[38] C.P. Herzog et al., *Energy loss of a heavy quark moving through $N = 4$ supersymmetric Yang-Mills plasma*, *JHEP* **07** (2006) 013 [hep-th/0605158] [INSPIRE].

JHEP04(2024)025

[39] S.S. Gubser, *Drag force in AdS/CFT*, *Phys. Rev. D* **74** (2006) 126005 [hep-th/0605182] [INSPIRE].

[40] J.M. Maldacena, *Wilson loops in large N field theories*, *Phys. Rev. Lett.* **80** (1998) 4859 [hep-th/9803002] [INSPIRE].

[41] S.-J. Rey, S. Theisen and J.-T. Yee, *Wilson-Polyakov loop at finite temperature in large N gauge theory and anti-de Sitter supergravity*, *Nucl. Phys. B* **527** (1998) 171 [hep-th/9803135] [INSPIRE].

[42] A. Brandhuber, N. Itzhaki, J. Sonnenschein and S. Yankielowicz, *Wilson loops in the large N limit at finite temperature*, *Phys. Lett. B* **434** (1998) 36 [hep-th/9803137] [INSPIRE].

[43] S.-J. Rey and J.-T. Yee, *Macroscopic strings as heavy quarks in large N gauge theory and anti-de Sitter supergravity*, *Eur. Phys. J. C* **22** (2001) 379 [hep-th/9803001] [INSPIRE].

[44] K. Hashimoto, K. Murata and N. Tanahashi, *Chaos of Wilson Loop from String Motion near Black Hole Horizon*, *Phys. Rev. D* **98** (2018) 086007 [arXiv:1803.06756] [INSPIRE].

[45] H.W. Lin, J. Maldacena and Y. Zhao, *Symmetries Near the Horizon*, *JHEP* **08** (2019) 049 [arXiv:1904.12820] [INSPIRE].

[46] H.W. Lin and D. Stanford, *A symmetry algebra in double-scaled SYK*, *SciPost Phys.* **15** (2023) 234 [arXiv:2307.15725] [INSPIRE].

[47] V. Cardoso et al., *Geodesic stability, Lyapunov exponents and quasinormal modes*, *Phys. Rev. D* **79** (2009) 064016 [arXiv:0812.1806] [INSPIRE].

[48] M. Bianchi, A. Grillo and J.F. Morales, *Chaos at the rim of black hole and fuzzball shadows*, *JHEP* **05** (2020) 078 [arXiv:2002.05574] [INSPIRE].

[49] P. Hintz and A. Vasy, *Analysis of linear waves near the Cauchy horizon of cosmological black holes*, *J. Math. Phys.* **58** (2017) 081509 [arXiv:1512.08004] [INSPIRE].

[50] L. Motl and A. Neitzke, *Asymptotic black hole quasinormal frequencies*, *Adv. Theor. Math. Phys.* **7** (2003) 307 [hep-th/0301173] [INSPIRE].

[51] A. Stepanchuk and A.A. Tseytlin, *On (non)integrability of classical strings in p-brane backgrounds*, *J. Phys. A* **46** (2013) 125401 [arXiv:1211.3727] [INSPIRE].

[52] L.A. Pando Zayas and C.A. Terrero-Escalante, *Chaos in the Gauge/Gravity Correspondence*, *JHEP* **09** (2010) 094 [arXiv:1007.0277] [INSPIRE].

[53] V.E. Korepin, N.M. Bogoliubov and A.G. Izergin, *Quantum Inverse Scattering Method and Correlation Functions*, Cambridge University Press, Cambridge (1993) [DOI:10.1017/CBO9780511628832] [INSPIRE].

[54] J. Ruiz, *Differential Galois Theory and Non-Integrability of Hamiltonian Systems*, Springer Basel (1999) [DOI:10.1007/978-3-0348-8718-2].

[55] Y. Chervonyi and O. Lunin, *(Non)-Integrability of Geodesics in D-brane Backgrounds*, *JHEP* **02** (2014) 061 [arXiv:1311.1521] [INSPIRE].

[56] P. Basu and L.A. Pando Zayas, *Analytic Non-integrability in String Theory*, *Phys. Rev. D* **84** (2011) 046006 [arXiv:1105.2540] [INSPIRE].

[57] K. Hashimoto, K.-B. Huh, K.-Y. Kim and R. Watanabe, *Exponential growth of out-of-time-order correlator without chaos: inverted harmonic oscillator*, *JHEP* **11** (2020) 068 [arXiv:2007.04746] [INSPIRE].

JHEP04(2024)025

[58] K. Goldstein, S. Kachru, S. Prakash and S.P. Trivedi, *Holography of Charged Dilaton Black Holes*, *JHEP* **08** (2010) 078 [arXiv:0911.3586] [INSPIRE].

[59] C. Charmousis et al., *Effective Holographic Theories for low-temperature condensed matter systems*, *JHEP* **11** (2010) 151 [arXiv:1005.4690] [INSPIRE].

[60] B. Gouteraux and E. Kiritsis, *Generalized Holographic Quantum Criticality at Finite Density*, *JHEP* **12** (2011) 036 [arXiv:1107.2116] [INSPIRE].

[61] B. Gouteraux and E. Kiritsis, *Quantum critical lines in holographic phases with (un)broken symmetry*, *JHEP* **04** (2013) 053 [arXiv:1212.2625] [INSPIRE].

[62] G.W. Gibbons and P.K. Townsend, *Vacuum interpolation in supergravity via super p-branes*, *Phys. Rev. Lett.* **71** (1993) 3754 [hep-th/9307049] [INSPIRE].

[63] H.J. Boonstra, B. Peeters and K. Skenderis, *Duality and asymptotic geometries*, *Phys. Lett. B* **411** (1997) 59 [hep-th/9706192] [INSPIRE].

[64] J.M. Maldacena and A. Strominger, *Black hole grey body factors and d-brane spectroscopy*, *Phys. Rev. D* **55** (1997) 861 [hep-th/9609026] [INSPIRE].

[65] A. Strominger and C. Vafa, *Microscopic origin of the Bekenstein-Hawking entropy*, *Phys. Lett. B* **379** (1996) 99 [hep-th/9601029] [INSPIRE].

[66] J.M. Maldacena, *The large N limit of superconformal field theories and supergravity*, *Adv. Theor. Math. Phys.* **2** (1998) 231 [hep-th/9711200] [INSPIRE].

[67] N. Seiberg and E. Witten, *The D1/D5 system and singular CFT*, *JHEP* **04** (1999) 017 [hep-th/9903224] [INSPIRE].

[68] O. Aharony et al., *Large N field theories, string theory and gravity*, *Phys. Rept.* **323** (2000) 183 [hep-th/9905111] [INSPIRE].

[69] O. Lunin and S.D. Mathur, *A toy black hole S-matrix in the D1-D5 CFT*, *JHEP* **02** (2013) 083 [arXiv:1211.5830] [INSPIRE].

[70] E. Kiritsis, *String theory in a nutshell*, Princeton University Press, U.S.A. (2019) [DOI:10.2307/j.ctvcm4hd1].

[71] O. Lunin and S.D. Mathur, *Correlation functions for M^N/S_N orbifolds*, *Commun. Math. Phys.* **219** (2001) 399 [hep-th/0006196] [INSPIRE].

[72] O. Lunin and S.D. Mathur, *Three point functions for M^N/S_N orbifolds with $N = 4$ supersymmetry*, *Commun. Math. Phys.* **227** (2002) 385 [hep-th/0103169] [INSPIRE].

[73] V. Jahnke, K.-Y. Kim and J. Yoon, *On the Chaos Bound in Rotating Black Holes*, *JHEP* **05** (2019) 037 [arXiv:1903.09086] [INSPIRE].

[74] A. Banerjee, A. Kundu and R.R. Poojary, *Rotating black holes in AdS spacetime, extremality, and chaos*, *Phys. Rev. D* **102** (2020) 106013 [arXiv:1912.12996] [INSPIRE].

[75] P. Banerjee, *Holographic Brownian motion at finite density*, *Phys. Rev. D* **94** (2016) 126008 [arXiv:1512.05853] [INSPIRE].

[76] L.D. Landau and E.M. Lifshits, *Quantum Mechanics: Non-Relativistic Theory*, Butterworth-Heinemann, Oxford (1991) [INSPIRE].

[77] S.S. Gubser, *Momentum fluctuations of heavy quarks in the gauge-string duality*, *Nucl. Phys. B* **790** (2008) 175 [hep-th/0612143] [INSPIRE].

[78] D. Giataganas and H. Soltanpanahi, *Universal Properties of the Langevin Diffusion Coefficients*, *Phys. Rev. D* **89** (2014) 026011 [arXiv:1310.6725] [INSPIRE].

JHEP04(2024)025

[79] D. Giataganas, *Stochastic Motion of Heavy Quarks in Holography: A Theory-Independent Treatment*, *PoS* **CORFU2017** (2018) 032 [arXiv:1805.09011] [INSPIRE].

[80] J. Casalderrey-Solana and D. Teaney, *Transverse Momentum Broadening of a Fast Quark in a $N = 4$ Yang Mills Plasma*, *JHEP* **04** (2007) 039 [hep-th/0701123] [INSPIRE].

[81] J. Casalderrey-Solana, K.-Y. Kim and D. Teaney, *Stochastic String Motion Above and Below the World Sheet Horizon*, *JHEP* **12** (2009) 066 [arXiv:0908.1470] [INSPIRE].

[82] A.N. Atmaja, J. de Boer and M. Shigemori, *Holographic Brownian Motion and Time Scales in Strongly Coupled Plasmas*, *Nucl. Phys. B* **880** (2014) 23 [arXiv:1002.2429] [INSPIRE].

[83] M. Blake, R.A. Davison and D. Vegh, *Horizon constraints on holographic Green's functions*, *JHEP* **01** (2020) 077 [arXiv:1904.12883] [INSPIRE].

[84] T. Faulkner, H. Liu, J. McGreevy and D. Vegh, *Emergent quantum criticality, Fermi surfaces, and AdS_2*, *Phys. Rev. D* **83** (2011) 125002 [arXiv:0907.2694] [INSPIRE].

[85] V. Cardoso and J.P.S. Lemos, *Scalar, electromagnetic and Weyl perturbations of BTZ black holes: Quasinormal modes*, *Phys. Rev. D* **63** (2001) 124015 [gr-qc/0101052] [INSPIRE].

[86] E. Berti, V. Cardoso and A.O. Starinets, *Quasinormal modes of black holes and black branes*, *Class. Quant. Grav.* **26** (2009) 163001 [arXiv:0905.2975] [INSPIRE].

[87] M. Bianchi, D. Consoli, A. Grillo and J.F. Morales, *Light rings of five-dimensional geometries*, *JHEP* **03** (2021) 210 [arXiv:2011.04344] [INSPIRE].

[88] M. Bianchi, M. Firrotta, J. Sonnenschein and D. Weissman, *Measure for Chaotic Scattering Amplitudes*, *Phys. Rev. Lett.* **129** (2022) 261601 [arXiv:2207.13112] [INSPIRE].

[89] B. Craps, S. Khetrapal and C. Rabideau, *Chaos in CFT dual to rotating BTZ*, *JHEP* **11** (2021) 105 [arXiv:2107.13874] [INSPIRE].

[90] K. Hashimoto, K. Sugiura, K. Sugiyama and T. Yoda, *Photon sphere and quasinormal modes in AdS/CFT*, *JHEP* **10** (2023) 149 [arXiv:2307.00237] [INSPIRE].

[91] M. Riojas and H.-Y. Sun, *The Photon Sphere and the AdS/CFT Correspondence*, arXiv:2307.06415 [INSPIRE].

[92] M. Bianchi and G. Di Russo, *Turning black holes and D-branes inside out of their photon spheres*, *Phys. Rev. D* **105** (2022) 126007 [arXiv:2110.09579] [INSPIRE].

[93] D. Roychowdhury, *Analytic integrability for holographic duals with $J\overline{T}$ deformations*, *JHEP* **09** (2020) 053 [arXiv:2005.04457] [INSPIRE].

[94] J. Pal, S. Roychowdhury, A. Lala and D. Roychowdhury, *Integrability and non-integrability for marginal deformations of 4d $\mathcal{N} = 2$ SCFTs*, *JHEP* **10** (2023) 173 [arXiv:2307.12079] [INSPIRE].

[95] D.S. Ageev, *Chaotic nature of holographic QCD*, *Phys. Rev. D* **104** (2021) 126013 [arXiv:2105.04589] [INSPIRE].

[96] T. Ishii, R. Kitaku, K. Murata and C.-M. Yoo, *Turbulence on open string worldsheets under non-integrable boundary conditions*, *JHEP* **02** (2024) 149 [arXiv:2310.19317] [INSPIRE].

[97] S. Giombi, S. Komatsu and B. Offertaler, *Chaos and the reparametrization mode on the AdS_2 string*, *JHEP* **09** (2023) 023 [arXiv:2212.14842] [INSPIRE].

[98] Y. Chen, V. Ivo and J. Maldacena, *Comments on the double cone wormhole*, arXiv:2310.11617 [INSPIRE].

Published for SISSA by Springer

Received: *April 26, 2022*
Accepted: *July 30, 2022*
Published: *August 22, 2022*

Emerging Fermi liquids from regulated quantum electron stars

Nicolas Chagnet,[a] **Vladan Đukić,**[b,c] **Mihailo Čubrović**[b] **and Koenraad Schalm**[a]

[a] *Institute Lorentz for Theoretical Physics, Δ-ITP, Leiden University, Niels Bohrweg 2, Leiden, The Netherlands*
[b] *Center for the Study of Complex Systems, Institute of Physics Belgrade, University of Belgrade, Pregrevica 118, 11080 Belgrade, Serbia*
[c] *Department of Physics, University of Belgrade, Studentski Trg 12-16, 11000 Belgrade, Serbia*

E-mail: chagnet@lorentz.leidenuniv.nl, vdjukicns@gmail.com, cubrovic@ipb.ac.rs, kschalm@lorentz.leidenuniv.nl

Abstract: We construct a fully quantum zero-temperature electron star in a soft-wall regulated anti-de-Sitter Einstein-Maxwell-Dirac theory that is thermodynamically stable compared to the Reissner-Nordström black hole. The soft wall only acts on the effective mass of the fermionic degrees of freedom, and allows for a controlled fully backreacted solution. The star is holographically dual to an RG flow where a gapped Fermi liquid starts to emerge from a UV CFT, but decouples again once the effective energy scale becomes lower than the gap of the fermionic degrees of freedom. The RG flow then returns to a non-trivial strongly coupled relativistic fixed point with a holographic dual. Our regulated quantum electron star is thus the fermionic analogue of the Horowitz-Roberts-Gubser-Rocha AdS-to-AdS domain wall solution for the holographic superconductor.

Keywords: AdS-CFT Correspondence, Holography and Condensed Matter Physics (AdS/CMT), Gauge-Gravity Correspondence, Renormalization Group

ArXiv ePrint: 2204.10092

https://doi.org/10.1007/JHEP08(2022)222

JHEP08(2022)222

Contents

JHEP08(2022)222

1 Introduction

Strongly correlated electrons at finite density remain a deep and interesting puzzle, encountered in various quantum-many body systems, from condensed matter to heavy ion physics to astrophysics. Apart from some special cases, Fermi liquids are the only interacting fermionic systems at finite density where we have good control. A breakthrough was provided by the application of AdS/CFT to finite density large N-matrix fermionic systems. This allowed new strongly coupled IR fixed points characterized by an emergent Lifshitz scaling with dynamical critical exponent z to be discovered.[1] Though many of such results were found in bottom-up holographic models where only bosonic operators are tracked, there is reason to believe that any holographic finite density systems must also have microscopic fermionic degrees of freedom. Indeed a number of these holographically discovered fixed points have now been independently confirmed as Sachdev-Ye-Kitaev-like large N quantum spin-liquid fermionic ground states, where the additional microscopic description allows valuable extra insights into the workings of these novel states of matter.

[1] At finite N these fixed points may be not be true IR fixed points but intermediate scale attractors in the RG flow.

In holography these new ground states are qualitatively understood to arise as a deconfined phase of an underlying microscopic theory with the confined phase corresponding to a conventional Fermi liquid; see [1]. A dozen years ago this was a hotly debated topic and it was found that the prototypical deconfined state, characterized by the AdS_2, $z = \infty$ near horizon dynamics of AdS Reissner-Nordstrom (RN) black holes and an associated multitude N of non-Fermi-liquid Fermi surfaces [2–4] in the Thomas-Fermi limit of $N \to \infty$ indeed transitions at low temperatures to a charged Tolman-Oppenheimer-Volkov electron star [5–9]. These states are partially confined-partially deconfined in that they still have a finite z Lifshitz horizon; for a review and the transport responses of these states, see [10, 11].

However, away from the Thomas-Fermi limit a holographic description of a direct single Fermi-surface deconfined non-Fermi-liquid-to-confined Fermi-liquid $T = 0$ quantum phase transition has so far not yet been found. In the bulk, this problem corresponds to solving an Einstein-Maxwell-Dirac system in a self-consistent way, accounting for the backreaction of fermions on geometry, but keeping the number of Fermi surfaces finite or specifically keeping only one. The distinct puzzle here is that the signal of the putative instability towards confinement at low temperature — a log-oscillatory response in the single fermion spectral function [4] — occurs at a distinct point in parameter space from the one where the first stable Fermi surface is located (figure 1). In [12] an electron star model is introduced where N is finite but still very large; this hinted at a first order rather than a continuous transition. Approaching the question from the other side, a holographic description of confined single Fermi surface Fermi-liquid was constructed in [13] by enforcing confinement through a hard wall IR cut-off [13]. This confirmed that confinement-deconfinement is the correct viewpoint of the quantum phase transition, but did not yet include the gravitational backreaction. The most comprehensive study to date is the attempt at quantum electron star model of [14, 15] which regulates the system by putting it on a sphere and then tries to carefully remove this regularization procedure for a self-consistent solution of the Einstein-Maxwell-Dirac equations in the asymptotic AdS background.

The simple hard-wall solution of [13] already illustrates the fundamental problem. In the presence of an occupied Fermi surface the gravitational backreaction is uncontrolled, see [14, 15]. These subsequent papers then address this by a second cut-off for the backreaction, and then attempt to remove both cut-offs in a precarious balancing act. In the present paper we address this in a different way. We construct a fully gravitionally backreacted single-Fermi surface solution confined through a soft rather than a hard wall. From the gravitational point of view this soft wall determines the deep interior boundary conditions of the fermionic wave functions instead of the horizon geometry. As illustrated in detail in [14, 15] at the technical level the puzzle is that with the vanishing of the horizon (signalling deconfinement) at the quantum phase transition, not only must one find a new self-consistent (confining) IR geometry, but also an associated set of self-consistent boundary conditions for the fermion wave-function.

Because the confining boundary conditions suppress the fermion wave function in the IR, there is also no associated backreaction in the deep IR, which remains AdS. This confined regulated quantum electron star (rQES) is therefore the fermionic analogue of the Horowitz-Roberts-Gubser-Rocha AdS_4-to-AdS_4 groundstate/domain wall for holographic

JHEP08(2022)222

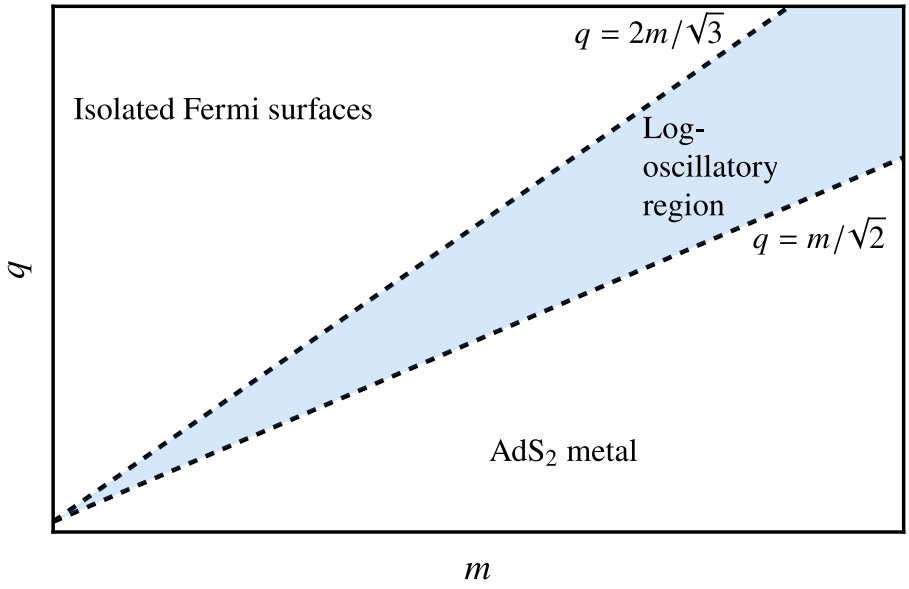

Figure 1. A schematic representation of the phase diagram of holographic fermions, where q and m are the charge and the mass (related to the scaling dimension in field theory $\Delta = 3/2 + m$) of the bulk fermion respectively. Along the line $q = m/\sqrt{2}$, determined by the Schwinger pair production threshold, the quantum phase transition ought to happen between the Reissner-Nordström black hole describing the strange metal phase and the quantum electron star solution (no black hole) corresponding to a metallic phase. However, this line is not identical to boundary of the regime where the Reissner-Nordström system supports stable Fermi surfaces as probed through the Reissner-Nordström spectral functions. The electron star (fluid) model requires taking the limit $q, m \to 0$ where both critical lines become indistinguishable. To understand the transition at finite q, m is the motivation for our approach. Adapted from [4].

superconductors [16, 17]. This solution (just like our soft wall confining electron star solution) describes a system that flows from a conformal pure AdS UV to an intermediate ordered holographic superconductor (Fermi liquid) state with a gap in the sense that below that gap it returns to the renormalized conformal theory and low energy excitations cannot disturb the ordered state. As is well-known the generic holographic superconductor ground state is not AdS_4-to-AdS_4 but of the Lifshitz type [18]. It is the technical difficulties described above that guided us to first construct this Horowitz-Roberts-Gubser-Rocha type solution. We leave the full Lifshitz quantum electron star for future work. One natural way to construct the latter is that, rather than trying to remove the soft-wall regulator, one can also make it dynamical, similar to the electron star study in [19].

We do confirm that within the class of non-dynamical soft-wall solutions this gapped confined holographic Fermi liquid is the thermodynamically preferred state over the deconfined Reissner-Nordström metallic state for appropriate charge and mass of the fermion. Because we are not yet able to remove the regulator we do not yet solve the puzzle of figure 1 directly.

The outline of the paper is the following. In section 2 we present the gravity setup and the regulated quantum electron star (rQES) solution. In section 3, we present the

JHEP08(2022)222

properties of our rQES solution, i.e. the gapped confined Fermi liquid: we show it is the thermodynamically preferred solution in a certain range of parameters, and demonstrate the existence of the infinitely long-lived quasiparticle peaks in the spectrum of the boundary theory. In section 4, we present some considerations about removing the confining soft wall. Section 5 sums up the conclusions together with some musings on further directions of work and the physical meaning of our results.

2 A confined quantum electron star: set-up

The minimal bottom-up gravity dual of a strongly correlated electron system is the Einstein-Maxwell-Dirac system [2–4]. The new element of our setup is the phenomenological soft-wall-like regulator inspired by bottom-up AdS/QCD [20]. The regulator is a fixed non-dynamic scalar field, which neither backreacts on the metric itself nor does it feel the backreaction by the fermions. This is again in line with AdS/QCD models. Therefore, the geometry starts as pure AdS in the UV, in the interior it is influenced by the gauge and matter fields and deviates from AdS, and in far IR all matter fields are exponentially damped by the confining potential. However, in contrast to most hard/soft-wall models we will let the potential only damp the matter sector and not the gravitational sector. The action of the system is:

$$S = \int \mathrm{d}^4x\sqrt{-g}\left[\frac{L^2}{2\kappa^2}\left(R+6\right) - \frac{L^2}{4}F_{\mu\nu}F^{\mu\nu} + L^3\mathcal{L}_f[\Psi,\Phi]\right] \tag{2.1}$$

where κ is the gravitational coupling constant; and L is set to $L=1$ in the remainder. The Dirac Lagrangian is:

$$\mathcal{L}_f = \bar{\Psi}\left[e_A^\mu\Gamma^A\left(\partial_\mu + \frac{1}{4}\omega_\mu^{BC}\Gamma_{BC} - iqA_\mu\right) - \left(m + \hat{M}\Phi\right)\right]\Psi \tag{2.2}$$

where $\bar{\Psi} = i\Psi^\dagger\Gamma^0$, e_A^μ is the vierbein, Γ^A are the gamma matrices in four dimensions, and ω_μ^{AB} is the spin connection. The regulator is fully encoded in an effective mass contribution $\hat{M}(z)\Phi(z)$ for the Dirac field, with $\Phi(z)$ a non-dynamical scalar field whose profile we shall choose later. Inspired by [21], we will consider two types of the confining potential:

$$\hat{M} = \begin{cases} -e_3^z\Gamma^3\,, & \text{the potential preserves chirality}\,, \\ z\mathbb{1}_4\,, & \text{the potential breaks chirality}\,. \end{cases} \tag{2.3}$$

Here z, both as index and a variable, refers to the radial coordinate of the AdS space. We will assume a radially symmetric metric which is asymptotically AdS_{d+1} with $d=3$, parametrized as:

$$\mathrm{d}s^2 = -\frac{f(z)h(z)}{z^2}\mathrm{d}t^2 + \frac{\mathrm{d}x_i\mathrm{d}x^i}{z^2} + \frac{\mathrm{d}z^2}{z^2 f(z)}\,. \tag{2.4}$$

The radial coordinate is defined for $z \geq 0$, where $z=0$ is the location of AdS boundary (UV). Development of a horizon at finite z is in principle signified by the appearance of a zero of the function f: $f(z_H)=0$. At zero temperature (the only case we consider), the space extends to infinity, $0 \leq z \leq \infty$.

JHEP08(2022)222

Our choice to let the wall only confine the fermion-matter sector (together with the absence of backreaction by the confining scalar) implies that at finite chemical potential but zero bulk fermion density, the thermodynamically preferred solution is the regular charged (RN) black hole, though pure AdS with a constant electrostatic potential is also a solution.

For a certain value of the charge q of the fermion, it will be thermodynamically preferred to store all charge in an occupied bulk fermionic state, i.e. nonzero bulk density $n_c \equiv \langle \Psi^\dagger \Psi \rangle$, rather than a Reissner-Nordström black hole. Now the precise radial profile of the scalar $\Phi(z)$ becomes important. The original AdS/QCD papers used a quadratic scalar, behaving in the IR as $\Phi \sim z^2$ [22], which ensures confinement while still being smooth. Another form found in the literature is a profile which flattens out to a constant in the IR [23]. At the same time the UV completion of the scalar field has to ensure that its contribution to the Dirac equation decays quickly enough for small z to reproduce the equation of motion in pure AdS in the limit $z \to 0$. The forms that satisfy all the requirements and which we find numerically convenient are

$$\begin{aligned} \Phi(z) &= \lambda z^2, && \text{quadratic scalar} \\ \Phi(z) &= \lambda \frac{z^\alpha}{z_0^\alpha + z^\alpha}, && \text{flat scalar.} \end{aligned} \tag{2.5}$$

The amplitude of the scalar (i.e. the measure of the "hardness" of the wall) is parametrized by λ, and z_0 is the scale at which the scalar begins to flatten (in the second, flat scalar model). The choice of α is merely that of computational convenience and we choose $\alpha = 4$. Similarly, we will consistently choose $z_0 = 2$ throughout the rest of this paper.

2.1 Einstein-Maxwell-Dirac equations

From the action we obtain the Maxwell equation and two convenient linear combinations of the tt and zz components of the Einstein equations. With the ansatz that only $A_t \neq 0$, and that all functions only depend on z, compatible with homogeneity and isotropy, they reduce to

$$\begin{aligned} A_t''(z) - \frac{h'(z)}{2h(z)} A_t'(z) &= \sqrt{h(z)} n(z)\,, \\ 1 + \frac{z}{3} f'(z) - f(z) &= \frac{z^2}{3 f(z) h(z)} \rho(z) + \frac{z^4}{12 h(z)} A_t'(z)^2\,, \\ h'(z) &= -z h(z) p(z) - \frac{z}{f(z)^2} \rho(z)\,. \end{aligned} \tag{2.6}$$

Compatible with the symmetries the current vanishes $J^i = 0$, the charge density J^0 is denoted as $J^0 = n(z)/\sqrt{-g} = z^4 n(z)/\sqrt{h(z)}$, and the stress tensor is parametrized as

$$(T_f)_{\mu\nu} = \mathrm{diag}(\rho(z), p_\perp(z), p_\perp(z), p(z)), \tag{2.7}$$

where $p_\perp(z)$ is the pressure in the transverse x, y directions.

The ii components of the Einstein equations are both equal to

$$\begin{aligned} & z h(z) \left[-z^3 A_t'(z)^2 + \left(3 z f'(z) - 4 f(z)\right) h'(z) + 2 z f(z) h''(z) \right] + \\ & \quad + 2 h(z)^2 \left[z \left(z f''(z) - 4 f'(z) - 2\beta z p_\perp(z) \right) + 6 f(z) - 6 \right] - z^2 f(z) h'(z)^2 = 0\,. \end{aligned}$$

They are not independent, however. Denoting the Einstein field equations as $E_{\mu\nu} \equiv G_{\mu\nu} - T_{\mu\nu}$ and the Maxwell equation as $E_M \equiv \nabla_\mu F^{\mu\nu} - J^\nu$, one can show that[2]

$$E_{xx} = \hat{L} \cdot E - \frac{1}{2z} \nabla_\mu T^{\mu\nu} \,, \tag{2.8}$$

where $\hat{L} \cdot E \equiv A_1 \partial_z E_{tt} + A_2 \partial_z E_{zz} + A_3 E_M + A_4 f'(z) E_{tt} + E_{zz} \left(A_5 f'(z) + A_6 h'(z) + A_7 \right)$ is a linear combination of both $\{E_{tt}, E_{zz}, E_M\}$ and their derivatives and $T^{\mu\nu}$ is the total stress-energy tensor associated with the matter content of the theory. The stress-tensor is covariantly conserved if the matter sector is on-shell, i.e. obeys its equations of motion. Thus

$$E_{xx}^{\text{on-shell}} = \nabla_\mu T^{\mu\nu} = 0 \tag{2.9}$$

It is therefore sufficient to solve the three equations (2.6) together with the matter sector.

The charge, energy and pressure densities $n(z), \rho(z), p(z)$ are determined by the occupied fermionic states in the AdS bulk space. Importantly, we will compute them *solely from microscopic considerations*: we do *not* assume anything like a fluid limit or a specific form of the equation of state. We compute them from the Dirac Lagrangian, within the one-loop Hartree correction to the background. This is discussed in detail in the next subsection.

We will now proceed to derive the equation of motion for the Dirac field. From (2.2), the equation reads:

$$e_A^\mu \Gamma^A \left(\partial_\mu + \frac{1}{4} \omega_\mu^{BC} \Gamma_{BC} - iqA_\mu \right) \Psi = \left(m + \hat{M}(z) \Phi \right) \Psi \,. \tag{2.10}$$

It is known that the spin connection in this type of metric can be eliminated by rescaling the fermion [2, 24]:

$$\Psi = (-g^{zz} \det g_{\mu\nu})^{-\frac{1}{4}} \tilde{\psi} = \left(\frac{f(z)h(z)}{z^{2d}} \right)^{-\frac{1}{4}} \tilde{\psi} \equiv a(z) \tilde{\psi}. \tag{2.11}$$

In addition, it is convenient to eliminate any singular terms from the fermionic wavefunction. Since our solutions are smooth in the interior as we shall see, the only singularity is the branch cut in the UV behaving as z^m. We thus rescale one more time

$$\tilde{\psi} = z^m \psi \equiv b(z) \psi. \tag{2.12}$$

In most cases we will use the rescaled form and write the equations for ψ. So far this is all independent of the gamma matrix representation. In order to simplify the equations of motion, we now employ the representation

$$\Gamma^\mu = \begin{pmatrix} 0 & \gamma^\mu \\ \gamma^\mu & 0 \end{pmatrix}, \quad \Gamma^3 = \begin{pmatrix} 1 & 0 \\ 0 & -1 \end{pmatrix}, \tag{2.13}$$

with $\mu \in \{0, 1, 2\}$, $\gamma^0 = i\sigma^2, \gamma^1 = \sigma^1, \gamma^2 = \sigma^3$ and $\sigma^{1,2,3}$ are the usual Pauli matrices. Homogeneity and isotropy along the t, x, y directions allow us to take the energy ω and momentum $k \equiv k_x$ as good quantum numbers, so the Dirac bispinor is expressed as

$$\psi = e^{-i\omega t + ikx} \left(\psi_1(z), \chi_1(z), -i\chi_2(z), i\psi_2(z) \right)^T . \tag{2.14}$$

[2] This is essentially $\nabla_\mu G^{\mu\nu} = \nabla_\mu T^{\mu\nu}$.

JHEP08(2022)222

As in [13, 24], this yields two (equivalent) decoupled systems for the two independent components, for $\psi_{1,2}$ and $\chi_{1,2}$, corresponding to the spin degeneracy of our system. We will focus on the ψ_i components for which the Dirac equation reads

$$\begin{aligned}\left[\partial_z+\varepsilon_+\Phi+\frac{m}{z}\left(1-\frac{1}{\sqrt{f(z)}}\right)\right]\psi_1(z)-\left[\frac{k}{\sqrt{f(z)}}+\frac{\omega+qA_t}{f(z)\sqrt{h(z)}}\right]\psi_2(z)=0\\ \left[\partial_z+\varepsilon_-\Phi+\frac{m}{z}\left(1+\frac{1}{\sqrt{f(z)}}\right)\right]\psi_2(z)+\left[\frac{\omega+qA_t}{f(z)\sqrt{h(z)}}-\frac{k}{\sqrt{f(z)}}\right]\psi_1(z)=0\,.\end{aligned} \tag{2.15}$$

where $\varepsilon_+=\varepsilon_-=1$ corresponds to the chiral-preserving potential and $\varepsilon_+=-\varepsilon_-=-1/\sqrt{f(z)}$ corresponds to the chiral-breaking potential.

2.2 Fermion densities and backreaction

The fermionic densities and pressures are obtained microscopically, from the Dirac Lagrangian (2.2):

$$\begin{aligned}\rho&=\langle\Psi^\dagger e_0^t\Gamma^0(-i\omega-iqA_t)\Psi\rangle\,,\\ n&=-\langle\Psi^\dagger\Psi\rangle\,.\end{aligned} \tag{2.16}$$

The components of the pressure $p_\perp, p$ are likewise formally equal to

$$\begin{aligned}p_\perp&=\langle\bar\Psi i e_1^x k_x\Gamma^1\Psi\rangle,\\ p&=\langle\bar\Psi e_3^z\Gamma^3\partial_z\Psi\rangle.\end{aligned} \tag{2.17}$$

The expectation value $\langle\ldots\rangle$ in (2.16)–(2.17) is the quantum-mechanical expectation value, i.e. one solves the Dirac equation with appropriate boundary conditions (see below) and sums over the quantum numbers in the appropriate range. The quantum numbers are the radial modes ℓ, and momenta k_x, k_y in the x, y-directions which determine the on-shell energy in terms of a dispersion relation $\omega=E_\ell(k)$. The role of the confining potential is essential here: it quantizes the radial number ℓ. Each discrete radial mode corresponds to a separate Fermi surface [2–4, 8, 9, 13]. As emphasized in the Introduction, we seek a state where only a single Fermi surface is occupied. This must be the lowest radial mode. Note that despite occupying a single mode, this mode still contains a thermodynamically large number of states counted by the x, y-momenta. Each radial mode is thus a fluid of fermions.

We will ignore the subtleties of the zero-point energy and the Dirac sea; in principle these are absorbed in a renormalization of the cosmological constant and the AdS radius; see however [14, 15] for a more detailed treatment. Then, in terms of the solutions to the Dirac equation, formally the expressions for the density are

$$\begin{aligned}n(z)&=\frac{2q}{z^3\sqrt{f(z)}}a(z)^2b(z)^2\sum_{k,\ell}\Theta\left(-E_\ell(k)\right)\ \left(\psi^\dagger_{1;\ell,k}(z)\psi_{1;\ell,k}(z)+\psi^\dagger_{2;\ell,k}(z)\psi_{2;\ell,k}(z)\right)\\ \rho(z)&=a(z)^2b(z)^2e_0^t(z)\left(-i\omega-iqA_t(z)\right)\sum_{k,\ell}\Theta\left(-E_\ell(k)\right)\left(\psi^\dagger_{1;\ell,k}(z)\psi_{1;\ell,k}(z)+\psi^\dagger_{2;\ell,k}(z)\psi_{2;\ell,k}(z)\right)\\ p(z)&=a(z)^2b(z)^2e_3^z(z)\sum_{k,\ell}\Theta\left(-E_\ell(k)\right)\left(\psi^\dagger_{1;\ell,k}\partial_z\psi_{2;\ell,k}-\psi^\dagger_{2;\ell,k}\partial_z\psi_{1;\ell,k}\right)\end{aligned} \tag{2.18}$$

JHEP08(2022)222

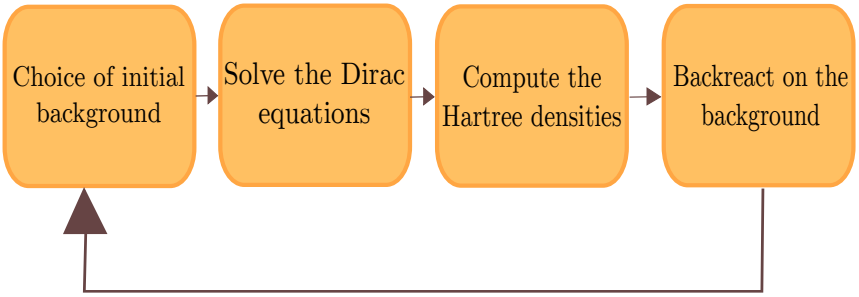

Figure 2. Iteration algorithm used to compute the rQES solution.

where the step-function $\Theta(x)$ selects the positive energy states. Note that due to the antisymmetry of the two spin components, the derivatives of the scaling factors $a(z), b(z)$ cancel out in the expression for p.

2.2.1 The self-consistent Hartree calculation

We solve the system (2.6), (2.15) in the one-loop Hartree approximation. As a reminder, the Hartree correction is the local single-particle diagram (vacuum bubble), ignoring anti-particles, i.e. ignoring the contribution from the Dirac sea. We do not take into account the Fock correction. In flat space, the Hartree correction is trivial [25]: in terms of the causal fermionic propagator G_R it equals $\lim_{t\to 0-}\int \mathrm{d}\omega \mathrm{d}^2k\ G_R(\omega,k)e^{-i\omega t} = \delta\mu$,[3] merely renormalizing the chemical potential. In curved space however, the local chemical potential is $\mu_{\mathrm{loc}}(z) = A_t(z)\sqrt{-g^{tt}(z)}$, with a nontrivial radial profile, thus the correction $\delta\mu(z)$ is also variable along z and therefore it can have nontrivial physical effects.

The Hartree approximation then proceeds by computing this one-loop Hartree correction self-consistently. One starts with an ansatz for the background, solves the Dirac equation in this background, computes the one-loop Hartree densities in the assumption that they are small, updates the background and iterates to convergence as in figure 2.

2.3 Boundary conditions on the Einstein-Maxwell sector

The Einstein-Maxwell equations (2.6) require four boundary conditions in total (two for $A_t(z)$ and one for each of the metric functions $f(z), h(z)$). The UV boundary conditions are

$$\begin{aligned} A_t(z_{\mathrm{UV}}) &= \mu\,, && \text{the chemical potential.} \\ f(z_{\mathrm{UV}}) = h(z_{\mathrm{UV}}) &= 1\,, && \mathrm{AdS}_4 \text{ asymptotics.} \end{aligned} \tag{2.19}$$

The fourth boundary condition we impose is given by our demand that we seek a state where *all* the charge is contained in occupied fermionic states.[4] The confining potential ensures that the fermionic wavefunctions are localized at a finite value in the radial direction.

[3] The infinitesimal time separation $t \to 0-$ is really the point-splitting regularization, as the integral of G_R at coincident points in spacetime generally diverges; the sign of t is dictated by the contour choice for the retarded propagator [25].

[4] There could be interpolating solutions with both a charged horizon and a charge in occupied fermionic states. We will not seek for those here as the presence of the charged Reissner-Nordstrom like horizons should imply the continued presence of log-oscillatory instabilities.

JHEP08(2022)222

Thus by construction the charge density will vanish in the deep AdS interior. From this follows that the fourth boundary condition is $\partial_z A_t(z_{\rm IR}) = 0$. Formally $z_{\rm IR} = \infty$; in our numerical computation it will be finite but large, and we have checked that our results do not depend on its value.

In practice, we solve the boundary value problem by shooting from the IR. We impose directly the condition $\partial_z A_t(z_{\rm IR}) = 0$ as well as the condition $\partial_z f(z_{\rm IR}) = 0$. The latter indirectly encodes our demand that we seek a $T = 0$ solution; recall that for a black hole solution $\partial_z f(z_{\rm horizon}) \sim T$. Then we use the free value $A_t(z_{\rm IR})$ and $h(z_{\rm IR})$ to shoot for $A_t(z_{\rm UV}) = \mu,\ h(z_{\rm UV}) = 1$ at the boundary. From the equation of motion for $f(z)$ one obtains automatically that $f(z_{\rm IR}) = 1$ once we fall on the right branch; for the same reason one can also use $f(z_{\rm IR}) = 1$ as an IR boundary condition if one demands in addition that there is no energy density or electric field in the deep interior.

2.4 Boundary conditions for the fermions

The UV boundary conditions for the appropriate solutions to the Dirac equation are straightforward. Near the AdS boundary the rescaled field behaves as

$$\begin{aligned}\psi_1(z \to 0) &\sim A_\ell(\omega,k)\frac{\omega - k - \mu q}{2m-1} z^{1-2m} + B_\ell(\omega,k) + \dots,\\ \psi_2(z \to 0) &\sim A_\ell(\omega,k)\ z^{-2m} + B_\ell(\omega,k)\frac{\omega + k - \mu q}{2m+1} z + \dots .\end{aligned} \tag{2.20}$$

On-shell solutions are normalizable, i.e. $A_\ell(\omega,k) = 0$. This agrees with the AdS/CFT dictionary, where a finite $A_\ell(\omega,k)$ would imply an external source for the fermions for a specific band ℓ and energy ω, k. Demanding normalizability $A_\ell(\omega,k) = 0$ instead, implicitly translates in a dispersion relation $\omega(k) = E_\ell(k)$.

The IR boundary conditions for the fermions require a more detailed discussion. Firstly, for the fermionic wavefunctions, the amplitude is set by normalization of each wavefunction to unity. For each radial mode ℓ this implies

$$\int dz \sqrt{-g} |\psi_{i;\ell,k}(z)|^2 < \infty. \tag{2.21}$$

For finite temperature backgrounds this is usually not an issue as the horizon is parametrically at finite distance and finite IR boundary conditions, together with the UV-condition that the un-normalizable fall-off vanish, guarantees a finite integral. For the $T = 0$ background we consider here, the interior is parametrically at infinite distance and finiteness of the integral can only follow from bounded behavior of the wavefunction. Since the spin components are not independent, it is sufficient to demand $\psi_{1;\ell}(z \to \infty) \to 0$, i.e., the leading component should vanish in the interior.

It is well known in AdS/CFT that it is then the simultaneous requirement of a UV and an IR boundary condition that determines the spectrum of the small excitations. This spectrum can still be continuous or discrete; we address this directly below. Formally, however, the normalization together with two boundary conditions make the system overconstrained and one must search for accidental solutions. We again do so by shooting from the interior to search for parameters where the UV conditions are also satisfied.

JHEP08(2022)222

The shooting condition we use is the ratio ψ_2/ψ_1, which still leaves the freedom to normalize the norm (2.21) to unity, and which we do after the solution is found.

2.4.1 Effective potentials and confinement

Pure $T = 0$ AdS — representing a deconfined phase of the strongly coupled boundary theory — has a continuum spectrum of normal modes computed in the way described above. The system must be considered in a different phase or have its IR dynamics modified by a confining potential to discretize the spectrum; this spectrum may still be ungapped or gapped. We will now demonstrate that the chiral-breaking soft-confining potential supports a discrete Fermi surface, i.e. a tower of bound states at discrete energies, for momenta up to some k_F, the Fermi momentum. The spectrum is also gapped. A convenient way to see the effect of this potential is to transform the Dirac equation to the Schrödinger form [4, 9, 10]:

$$\begin{aligned} \chi_{\text{Sch}}(z) &= e^{\frac{1}{2}\int_0^z \mathrm{d}u\, \mathcal{P}(u)}\,, \\ \left[\partial_z^2 - V(z)\right]\chi_{\text{Sch}}(z) &= 0\,, \\ V(z) &= \frac{1}{2}\mathcal{P}'(z) + \frac{1}{4}\mathcal{P}(z)^2 - \mathcal{Q}(z)\,, \end{aligned} \tag{2.22}$$

where the coupled equations (2.15) were decoupled into two second order equations, each taking the form

$$\psi''(z) + \mathcal{P}(z)\psi'(z) + \mathcal{Q}(z)\psi(z) = 0\,, \tag{2.23}$$

with the indices 1,2 on $\psi, \chi_{\text{Sch}}(z), V$ omitted.

In principle, the Schrödinger potential is itself a function of the background spacetime and electrostatic potential $f(z), h(z), A_t(z)$ and can be fully determined only by calculating numerically the full solution. However, we can give a qualitative estimate whether it is confining or not by studying its asymptotics. Since the bulk remains asymptotically AdS_4, we have $V(z \to 0) \sim \frac{1}{z^2}$. In pure AdS_4 the IR behavior would be $V_{\text{AdS-IR}}(z \to \infty) = -(\omega + \mu q)^2 + k^2 + m(m+1)/z^2 + \mathcal{O}(1/z^3)$ (figure 3).[5] This now gets modified by the confining potential due to the scalar $\Phi(z)$. Making the ansatz that the confining potential in the deep IR for $z \to \infty$ suppresses exponentially all sources in the Einstein and Maxwell equations for large z, i.e. the geometry in the deep IR is again an (emergent) AdS_4 geometry, the leading order IR behavior of the potential is then schematically

$$V_{\text{AdS-IR}} = V(z \to \infty) + (\varepsilon_- - \varepsilon_+)\left[-\frac{\phi'(z)}{2z} + \frac{\phi(z)(4m+2) + (\varepsilon_- - \varepsilon_+)\phi(z)^2}{4z^2} + \right] + \mathcal{O}(1/z^3)\,. \tag{2.24}$$

Note that the chiral-preserving solution $\varepsilon_+ = \varepsilon_- = 1$ leads to a vanishing contribution and therefore does not lead to fermionic bound states. In contrast the chiral-breaking solution $\varepsilon_+ = -\varepsilon_- = -1/\sqrt{f(z)} = -1 + \mathcal{O}(1/z)$ in an AdS_4 IR does lead to a potentially bounding potential depending on the choice of $\Phi(z)$. For this reason, we will work solely with the chiral-breaking scalar field.

[5] We are interested in $k^2 < (\omega + \mu q)^2$ since the potential is otherwise confining even in AdS_4 with no regulator, as discussed in [26]. We will discuss this later.

JHEP08(2022)222

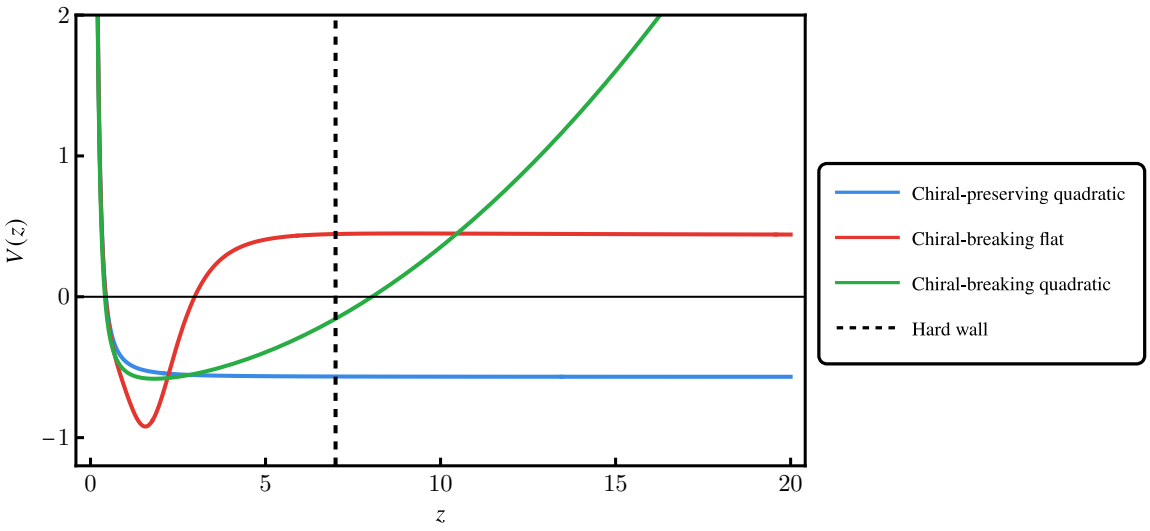

Figure 3. Comparison of the Schrödinger potentials for $\psi_1(z)$ for the two types of confining potential: chiral-breaking quadratic (green), chiral-breaking flat (red) and chiral-preserving quadratic (blue). The dashed black line indicates the truncation of spacetime which happens in the hard wall model of [13] at $z = 7$. Only the chiral-breaking potential and the hard wall allow for bound states. Parameters are $\{m, \mu q, k, \omega\} = \{0.1, 1.05, 0, -0.027\}$. The scalar parameters are $\lambda = 0.1$ for the two quadratic scalars and $\lambda = 1$ for the flat scalar.

Figure 3 shows the behavior of the Schrödinger potential for the various profiles of the scalar field and regulation schemes. With a chiral-breaking regulator, we indeed see that the infrared behavior of the potential is dominated by the large z behavior of each profile. The final choice of which scalar field profile to use is determined by the convergence of the iteration scheme. We numerically found the quadratic profile to be unstable while the flat profile leads to an emergent AdS_4 in the infrared. Specifically for the chiral-breaking confining potential with flat asymptotics the Schrödinger potential in the deep IR becomes

$$V(z \to z_{\rm IR}) = -\omega_{\rm IR}^2 + \lambda_{\rm IR}^2 + k_{\rm IR}^2 + \mathcal{O}(1/z) \equiv V_{\rm IR} + \mathcal{O}(1/z)\,, \tag{2.25}$$

where we have used that $f(z), h(z), A_t(z)$ become constant in the emergent AdS_4 IR and we have defined $\omega_{\rm IR} \equiv \dfrac{\omega + qA_t(z_{\rm IR})}{f(z_{\rm IR})\sqrt{h(z_{\rm IR})}}$, $\lambda_{\rm IR} \equiv \dfrac{\lambda}{\sqrt{f(z_{\rm IR})}}$ and $k_{\rm IR} \equiv \dfrac{k}{\sqrt{f(z_{\rm IR})}}$.

In the IR limit, the Schrödinger equation becomes

$$\left[\partial_z^2 - V_{\rm IR}\right] \chi_{\rm Sch}(z) = 0\,, \tag{2.26}$$

which is solved by

$$\chi_{\rm Sch}(z) = \chi_{\rm Sch+}(z) e^{\sqrt{V_{\rm IR}} z} + \chi_{\rm Sch-}(z) e^{-\sqrt{V_{\rm IR}} z}\,. \tag{2.27}$$

We see from (2.27) that, for frequencies such that $V_{\rm IR} > 0$, the solutions have a growing and a decaying branch. The decaying branch clearly confines the wavefunction. This is the one we shall choose. This leads to the following IR form for our original Dirac fermion

JHEP08(2022)222

components

$$\psi^{\rm IR}_{1,2}(z) = c^{\rm IR}_{1,2}(z) e^{-\sqrt{V_{\rm IR}} z}\,, \tag{2.28}$$

where the ratio of the coefficients is fixed by the Dirac equation (2.15):

$$\frac{\psi^{\rm IR}_2(z)}{\psi^{\rm IR}_1(z)} = \frac{c^{\rm IR}_2(z)}{c^{\rm IR}_1(z)} = \frac{1}{\omega_{\rm IR} + k_{\rm IR}} \left[\frac{m}{z} \left(\frac{1}{\sqrt{f_{\rm IR}}} - 1 \right) + \sqrt{V_{\rm IR}} + \lambda_{\rm IR} \right] \tag{2.29}$$

and the normalization of the wavefunction to unity sets the remaining overall scale.

With these IR boundary conditions the equations (2.15) are solved by shooting from $z_{\rm IR}$ to $z_{\rm UV}$.

The confinement imposed by both IR and UV boundary conditions leads to a discrete and gapped spectrum which defines a band structure (see figure 6 later). The fall-off of the wavefunction both at the AdS boundary and the interior also implies an absence of any backreaction in those regions. Once backreaction is included the resulting solutions will therefore be AdS_4-to-AdS_4 domain wall solutions, as we will show in the next section.

As a last remark, equation (2.25) gives us a simple way to view the effect of the chiral-breaking flat potential. As has been pointed out in [4, 26], in AdS_4 with constant electrostatic potential where $\lambda = 0$, the potential is deconfining for modes with $|\omega_{\rm IR}| > |k_{\rm IR}|$ and confining for modes such that $|\omega_{\rm IR}| < |k_{\rm IR}|$. The addition of a *flat* profile means that now modes with $|k_{\rm IR}| \leq |\omega_{\rm IR}| < \sqrt{k^2_{\rm IR} + \lambda^2_{\rm IR}}$, which previously were not bound states, also become confined. This allows the existence of a window $\omega_-(k) < \omega < \omega_+(k)$, with $\omega_\pm(k) \equiv q A_t(z_{\rm IR}) \pm \sqrt{k^2_{\rm IR} + \lambda^2_{\rm IR}}$ where a discrete set of (gapped) modes can be populated.

3 Regulated quantum electron star: thermodynamics and spectrum

Now that the problem is well-posed, we can follow the algorithm in figure 2 and construct a fully backreacted regulator-confined $T = 0$ quantum electron star. Choosing the chirality-breaking flat regulator the resulting solution is shown in figure 4. This is by construction an AdS_4-to-AdS_4 domain wall solution. Just like the analogous domain wall solutions for the holographic superconductor [16–18], it has a UV AdS_4 and an IR AdS_4 with the *same* radius but different effective speed of light. This can be checked by considering the diffeomorphism-invariant ratios $v_{\rm IR}/v_{\rm UV}$ and $L_{\rm IR}/L_{\rm UV}$ which are equal to

$$\frac{L_{\rm IR}}{L_{\rm UV}} = \sqrt{\frac{R(z \to z_{\rm UV})}{R(z \to z_{\rm IR})}} = 1\,, \quad \frac{v_{\rm IR}}{v_{\rm UV}} \equiv \frac{v(z \to z_{\rm IR})}{v(z \to z_{\rm UV})} = \sqrt{\frac{h(z \to z_{\rm IR})}{h(z \to z_{\rm UV})}} < 1 \text{ in our solution}\,. \tag{3.1}$$

Here $R(z)$ is the Ricci scalar and $v(z) = \sqrt{h(z)}$ is deduced from the null vector $\frac{\rm d}{{\rm d}t} X^\mu(z)$ where $X^\mu(z) \equiv \{t, 0, v(z)t, 0\}$ is a x-directed trajectory. Therefore, our solution obeys the c-theorem since the effective speed of light in the dual field theory is lower in the IR than in the UV, as discussed in detail in [17].

In accordance with our discussion in the Introduction, the chemical potential is chosen such that only the lowest radial mode of the fermionic wavefunction is occupied. The

JHEP08(2022)222

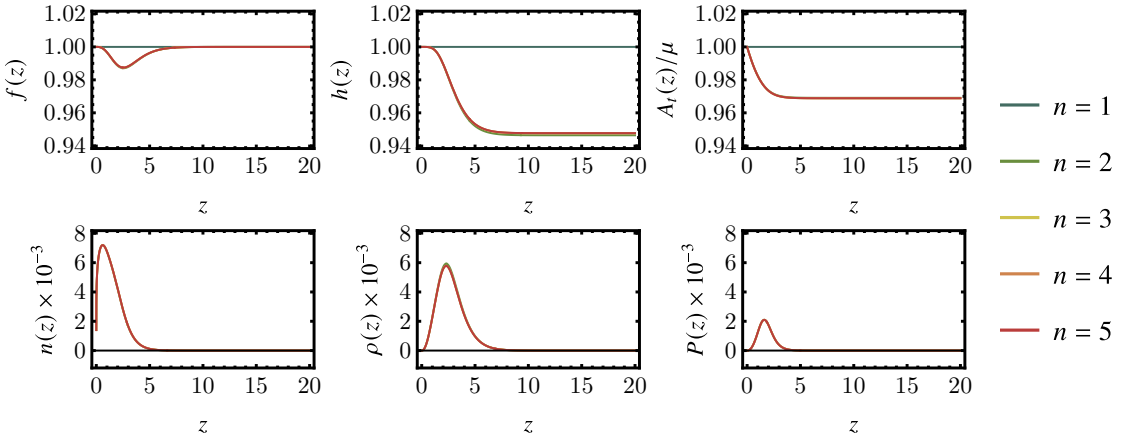

Figure 4. Iterative backreactions on the background fields ($f(z)$, $h(z)$, $A_t(z)$) and their associated currents $(n(z), \rho(z), P(z))$ with the same parameters as in figure 5. In total 5 iterations are performed, denoted by the color scale from green (first iteration) to red (last iteration). For these values $\{m, \mu q, \lambda\} = \{0.1, 0.9, 1\}$ only the first iteration differs significantly from the final solution, and the other curves are visually barely distinguishable from each other; for higher q convergence rapidly becomes slower.

associated matter content shows that a localized distribution of fermions in the mid-infrared region is characterized by a stable finite density of fermions with total charge $Q = -A_t'(z \to 0)$.

With the chirality-breaking flat potential the convergence is in fact quite fast at low density. The Hartree algorithm provides a discrete sequence of fields $(f^{(n)}, h^{(n)}, A_t^{(n)})$ as we iterate from $n = 1, 2, \ldots$. We can introduce a criterion for the convergence of the solution using the IR parameters used for shooting

$$\epsilon_n = \sqrt{f^{(n)}(z_{\rm IR})^2 + A_t^{(n)}(z_{\rm IR})^2 + h^{(n)}(z_{\rm IR})^2}\,. \tag{3.2}$$

Convergence is obtained if $(\Delta\epsilon)_n \equiv \epsilon_n - \epsilon_{n-1} \xrightarrow{n\to\infty} 0$. For a small occupation number/charge figure 5 shows that the solution already stabilizes after three iterations; for large occupation numbers the convergence rapidly becomes much slower. We have checked that the solution is not sensitive to the choice of the numerical cutoffs $\{z_{\rm UV}, z_{\rm IR}\}$.

3.1 Thermodynamics

For a large q/m ratio we expect that the quantum electron star at a given chemical potential μ is the thermodynamically preferred solution over the extremal Reissner-Nordström solution. In order to study the thermodynamics of the regulated quantum electron star, we need to compute its free energy. It consists of two parts. There is a direct saddle point contribution from the regularized Euclidean action:

$$S_E = \int \mathrm{d}^4x\sqrt{g_E}\left[\frac{1}{2\kappa^2}(R+6) - \frac{1}{4}F^2\right] + \oint_{z=\epsilon} \mathrm{d}^3x\sqrt{h}(-2K + 2\gamma)\,, \tag{3.3}$$

where g_E is the Euclidean metric, h is the induced metric on a hypersurface normal to a radial (z) slice, pointing outwards, K is the trace of the extrinsic curvature and $\gamma = 2$ is

JHEP08(2022)222

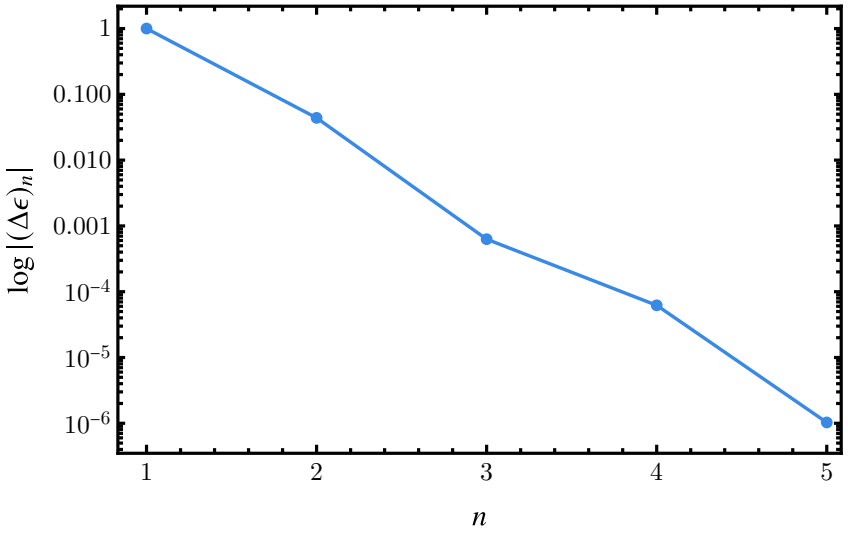

Figure 5. Convergence in terms of the logarithm of the difference in the IR between the n-th and $n+1$-st iteration $\log|(\Delta\epsilon)_n|$ for a rQES with $\{m, \mu q, \lambda\} = \{0.1, 0.9, 1\}$. The convergence is exponentially fast and the agreement is very good already around the 3^{rd} iteration.

required to make the AdS free energy vanish. The imaginary time at temperature T is compactified with the radius $\beta = 1/T$, the integral in the x–y plane produces the (infinite) volume Vol_2, and the radial integration is performed to some UV cutoff ϵ, yielding

$$S_E = \beta \text{Vol}_2 \int \mathrm{d}z \sqrt{g_E} \left[\frac{1}{2\kappa^2} (R+6) - \frac{1}{4} F^2 \right] + \beta \text{Vol}_2 \sqrt{h(\epsilon)} (-2K(\epsilon) + 2\gamma) \,. \tag{3.4}$$

This accounts for the contribution of the bosonic fields. The Dirac action vanishes on-shell and therefore does not contribute to this part. It does have a one-loop contribution to the free energy density

$$f \equiv \frac{S_E}{\beta \text{Vol}_2} + f_{\text{Dirac}} \,. \tag{3.5}$$

Here f_{Dirac} represents the fermionic contribution. Following [13, 24, 27, 28], at $T = 0$ we can simply sum the energies along the filled band of fermions (above the Dirac sea). This is the internal energy shifted by the chemical potential. For our normal modes, this leads to the expression

$$f_{\text{Dirac}} = \sum_\ell \int \frac{k \mathrm{d}k}{2\pi} \, \Theta(-E_\ell(k)) \Theta(E_\ell(k) - \mu q) E_\ell(k) = \int \frac{k \mathrm{d}k}{2\pi} \, \Theta(-E_1(k)) E_1(k)$$

where in the last line we have made explicit that we choose our chemical potential such that only states of the lowest electronic radial mode $E_{\ell=1}$ will be occupied. One must first choose the potential strength λ such that the Schrödinger potential supports at least one normalizable mode. At the same time, it is only these normalizable modes that can be populated. If there is only one band in the window of existence of normalizable modes $[\omega_-(k), \omega_+(k)]$, i.e.,$E_{\ell=1}(k) < \omega_+(k) < E_{\ell=2}(k)$, then increasing the chemical potential beyond that upper limit will not populate further normalizable modes. Our rQES is in this sense not plagued by the usual large-N Fermi surfaces artifact.

JHEP08(2022)222

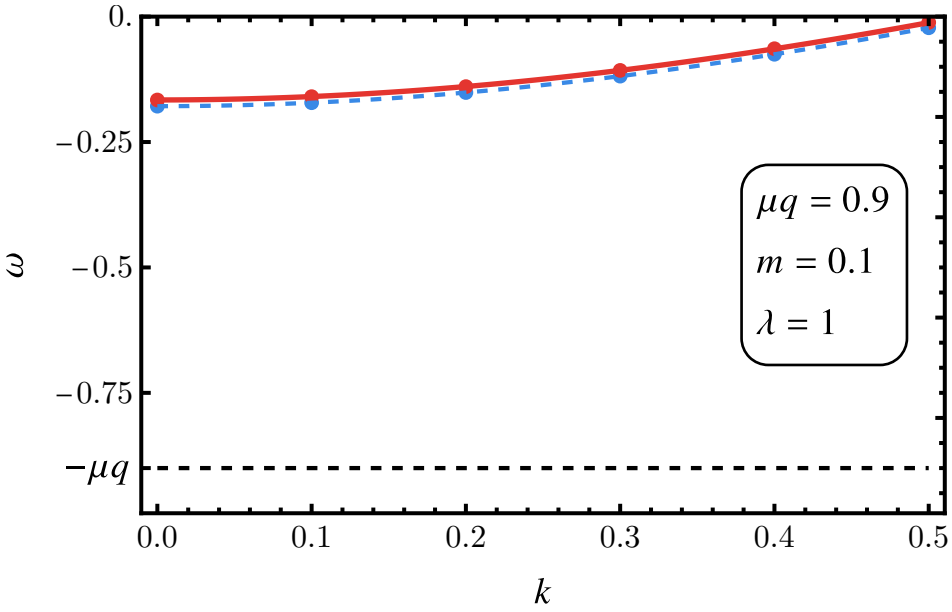

Figure 6. First electronic band for $\{m, \mu q, \lambda\} = \{0.1, 0.9, 1\}$, for the AdS_4 background with constant electrostatic potential (blue) and the backreacted solution (red). The lines are a fit to the form (3.6).

It is furthermore quite easy to show that both before and after accounting for backreaction the band structure follows a similar form as in pure AdS_4 [13]

$$E_\ell(k) = -E_0 + \sqrt{k^2 + k_0^2}\,, \tag{3.6}$$

where $k_F \equiv \sqrt{E_0^2 - k_0^2}$ and the parameters E_0, k_0 are most easily found by fitting from the numerical dispersion curves, as in figure 6.

Note that f_{Dirac} is negative semi-definite. This does not mean, however, that the occupied state is automatically thermodynamically preferred. The backreaction also changes the bosonic saddle point contribution compared to its original AdS_4 value $f(AdS_4) = 0$. Adding both contributions we compare to the RN free energy

$$f\,(\text{RN}) = -\frac{4 + z_h^2\mu^2}{4z_h^3} = -\frac{\mu^3}{6\sqrt{3}} \text{ at } T = 0\,. \tag{3.7}$$

Because the regulator does not act on the background sector, the Reissner-Nordström free energy is unaffected by it.

Figure 7 shows the free energy of the rQES as a function of the charge μq for a fixed mass m and confining potential strength λ. As q increases, the rQES grows, so we need to compute more and more modes. This becomes more and more time consuming. By constructing an interpolating curve based on low q rQES solutions (using the points until $\mu q \simeq 1.2$), we can estimate where the solution becomes thermodynamically preferred and verify this with a fewer number of large q datapoints ($\mu q = 1.4$ and $\mu q = 1.58$). We see that at $\mu q = \mu q_c \simeq 1.56$, the rQES becomes thermodynamically preferable over the RN background.

JHEP08(2022)222

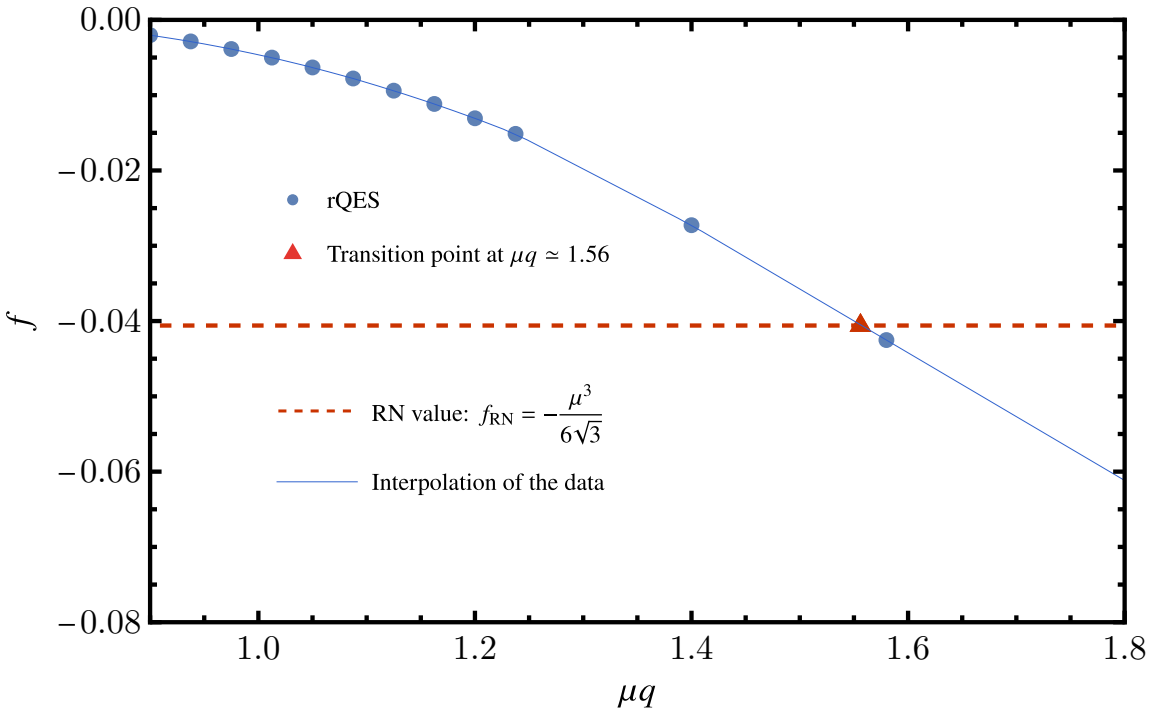

Figure 7. Plot of the free energy density for rQES at $\{\mu, m, \lambda\} = \{0.75, 0.1, 1\}$ as a function of the fermionic charge μq (blue dots) and the reference RN black hole free energy (red dashed line); the thin blue line and the red triangle are to guide the eye to the transition point. Since RN has no fermions its free energy curve is flat, i.e. does not depend on the fermion charge. The first-order phase transition from RN to rQES happens at the intersection of the two lines. Since the calculations for larger μq values are costly, we only compute two points for $\mu q > 1.5$ and interpolate.

In figure 8(a), we show that this transition point evolves linearly with the fermion mass m for fixed q and λ. Based on this finding, we can sketch a thermodynamic phase diagram for our model in figure 8(b). The critical charge satisfies an approximate relation $q_c(m;\lambda) \approx c_0(\lambda) + c_1(\lambda)\frac{m}{\mu}$ with c_0 and c_1 dependent on λ. It is tempting to compare this to the confounding phase diagram based on RN holography alone. For pure RN holography it is surmised [29] that the superradiant instability of the RN black hole toward an electron star (seen in the spectrum as log-periodic oscillations) sets in at $q = \sqrt{3}m$. This should correspond to the limit $\lambda \to 0$. As λ decreases we therefore expect the phase-boundary to pivot anti-clockwise. This comparison should be done with care, because the smaller λ becomes, the harder it is to observe bands that can be occupied — see the section on removing the regulator below. Another way to see this is that the effective Schrödinger potential in the extremal RN black hole for $\omega = k = 0$ (the onset of instability) has no linear term in m: $V_{\rm RN} \sim -4q^2 + 2m^2$. Hence we cannot extrapolate freely to $\lambda = 0$.

3.2 Spectrum of the rQES

To confirm our results, we consider the fermionic spectral function on rQES backgrounds. As a reminder, the spectral function is defined as the trace of the imaginary part of the retarded propagator: $A(\omega, k) = \mathrm{Im}\,\mathrm{Tr}\,G_R(\omega, k)$. In holography the type of propagator is defined by

JHEP08(2022)222

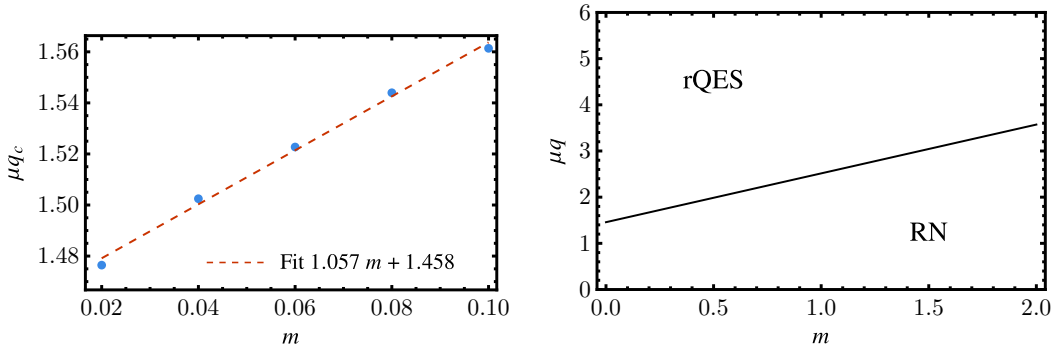

Figure 8. (a) Transition point μq_c as a function of m and its linear fit, for $\lambda = 1$. (b) Sketch of the phase diagram of the rQES. The black line indicates a first order transition between the regulated Reissner-Nordström and the rQES, occuring when their free energies cross.

the boundary conditions in the interior. Therefore the only difference with computing the normalizable Dirac solutions is the choice of appropriate boundary conditions.

Considering that we have an emergent AdS_4 geometry in the IR, we can use the known prescription for infalling boundary conditions in pure AdS, i.e. the presence of a Poincaré horizon [30]. Accounting for the confining potential, these are

$$\psi_1(z\to\infty) = \begin{cases} e^{-z\sqrt{\boldsymbol{k}_{\rm IR}^2}}\,, & \text{if} \quad \omega_{\rm IR}^2 < k_{\rm IR}^2+\lambda_{\rm IR}^2\,, \\ e^{iz\sqrt{-\boldsymbol{k}_{\rm IR}^2}}\,, & \text{if} \quad {\rm Re}[\omega_{\rm IR}] > \sqrt{k_{\rm IR}^2+\lambda_{\rm IR}^2}\,, \\ e^{-iz\sqrt{-\boldsymbol{k}_{\rm IR}^2}}\,, & \text{if} \quad {\rm Re}[\omega_{\rm IR}] < -\sqrt{k_{\rm IR}^2+\lambda_{\rm IR}^2}\,, \end{cases} \tag{3.8}$$

where $\omega_{\rm IR}, k_{\rm IR}, \lambda_{\rm IR}$ were defined by (2.25), $\boldsymbol{k}_{\rm IR} = \left(\omega_{\rm IR}, \sqrt{k_{\rm IR}^2+\lambda_{\rm IR}^2}, 0\right)$ and $\boldsymbol{k}_{\rm IR}^2 = -\omega_{\rm IR}^2 + k_{\rm IR}^2 + \lambda_{\rm IR}^2 = V_{\rm IR}$. As we saw with the normal modes, the IR boundary condition for ψ_2 can be obtained using the Dirac equation and the boundary condition for ψ_1. After imposing these boundary conditions, the retarded propagator is then computed as

$$G_R(\omega,k) = B/A = \lim_{z\to 0} z^{-2m}\frac{\psi_1(z)}{\psi_2(z)}\,, \tag{3.9}$$

where A and B are the coefficients in the UV expansion of the spinor (2.20).

Inside the gap ($\omega_{\rm IR}^2 < k_{\rm IR}^2 + \lambda_{\rm IR}^2$) the IR boundary conditions are the same for the probe fermions as for the bulk normalizable modes – the wavefunction should fall off for $z\to\infty$, which yields $A = 0$ for the normal mode frequencies $\omega = E_\ell(k)$. Therefore, the propagator will present a pole along the bands of the background. Moreover, since the fermionic wavefunctions and thus also the Green's functions are real inside the domain where bound states exist, the spectral function will vanish there. Thus, we expect to see ${\rm Im}\, G_R(\omega,k) = 0$ for $\omega \in [\omega_-(k), \omega_+(k)]$, except when $\omega = E_\ell(k)$ where a pole should appear.

This general structure of the spectral function including the gap for $\omega_- \le \omega \le \omega_+$ can be seen in figure 9. The data here and in the remainder of this section is computed for $\{\mu, q, m, \lambda\} = \{3/4, 1.2, 1/10, 1\}$. Inside the gap (white area), the spectral weight of

JHEP08(2022)222

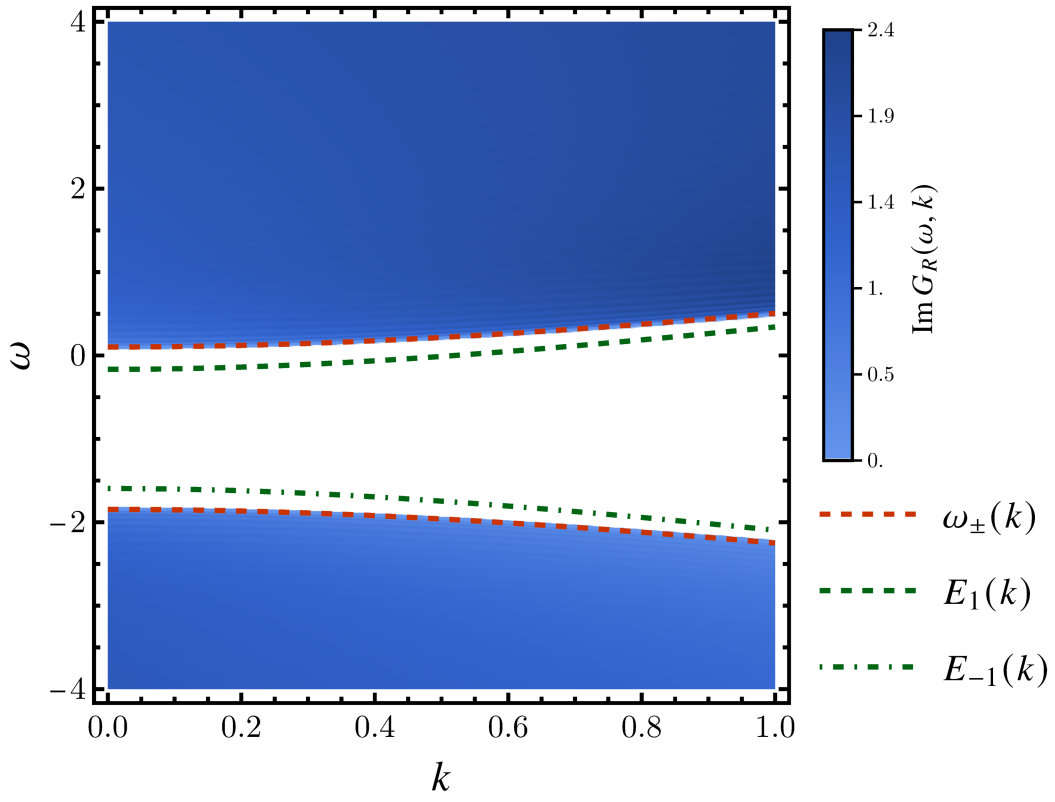

Figure 9. Spectral function $\mathrm{Im}\, G_R(\omega, k)$ for $\{m, \mu q, \lambda\} = \{0.1, 0.9, 1\}$. The gap appears in white and is well delimited by $\omega_\pm(k)$ (red dashed lines). The normal mode bands have been superimposed to show the infinitely long-lived modes, see figure 10. Outside the gap, there is no particle (normal mode) but a continuum shaped by the remnant of the UV conformal branch cuts. Since the regulator and the chemical potential explicitly break conformality, we do not reproduce the pure AdS Lorentz-invariant spectrum for any finite value of ω and k.

excitations is indeed zero to numerical accuracy except at the positions of the normal modes of the background fermions. The latter are computed directly from the solution of the background Dirac equation (green lines in figure 9), as they cannot be seen numerically in the spectral function because they are infinitely long-living modes which show in the spectrum as Dirac delta peaks. Being infinitely narrow on the real axis, they can only be detected in the complex-ω plane. Representing schematically the normal mode located at $\omega_\star$ by $\mathrm{Im}G(\omega = \mathrm{Re}(\omega)) = Z\delta(\omega - \omega_\star)$ where Z is the peak weight (wavefunction renormalization), we have, for complex ω:

$$\mathrm{Im}\, G_R(\omega, k) = -Z \frac{\mathrm{Im}\,\omega - \mathrm{Im}\,\omega_\star}{(\mathrm{Re}\,\omega - \mathrm{Re}\,\omega_\star)^2 + (\mathrm{Im}\,\omega - \mathrm{Im}\,\omega_\star)^2}\,. \tag{3.10}$$

When $\mathrm{Re}\,\omega = \mathrm{Re}\,\omega_\star$, this simplifies to

$$\mathrm{Im}\, G_R(\omega, k) = -\frac{Z}{\mathrm{Im}\,\omega - \mathrm{Im}\,\omega_\star}\,. \tag{3.11}$$

We check this picture against the numerics first in figure 10(A), where the absolute value of the spectral function in complex frequency plane shows the typical structure of a string of

JHEP08(2022)222

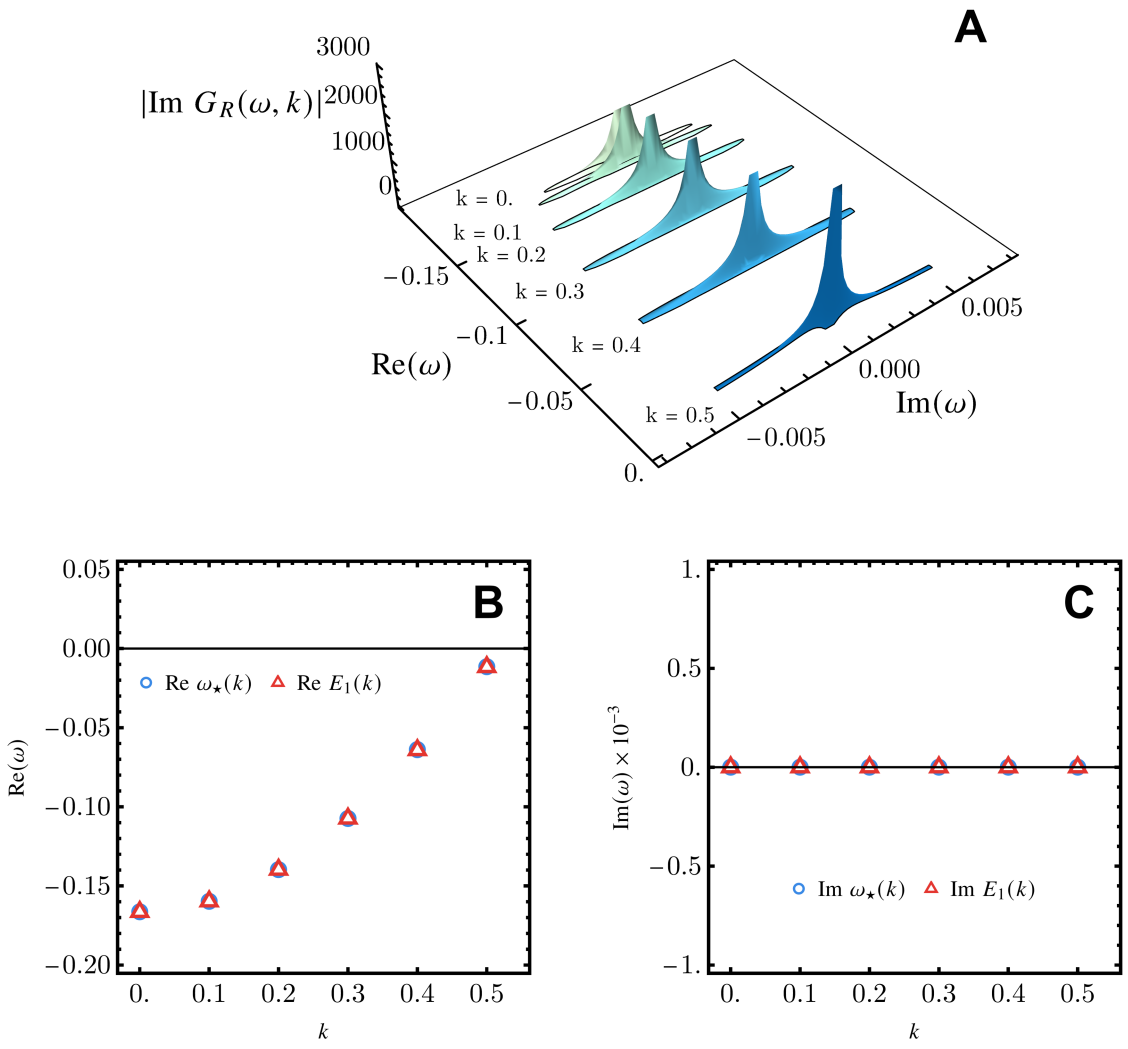

Figure 10. (A) Absolute value of the fermionic spectral function for different values of momentum. The plot is cropped for values below 100 to highlight the quasiparticle peaks. (B and C) Comparison of the poles in the spectrum (blue circles), identified in (A), to the first electron band of the background (red triangles). The real parts (B) of both sets agree perfectly; the imaginary parts (C) are both zero to high accuracy. All this data is computed for $\{m, \mu q, \lambda\} = \{0.1, 0.9, 1\}$.

poles (for various momentum values) lying on the real axis. The relation (3.11) is then used to identify the dispersion relation of the pole $\omega_\star(k)$ by fitting $\mathrm{Im}\, G_R(\omega, k)$. We find, with no big surprise, a perfect agreement with the normal mode excitations $E_1(k)$ corresponding to the first electron band, as seen in figure 10(C) and (D). A similar picture is found for the first hole band $E_{-1}(k)$ and this yields the spectrum inside the gap, plotted in figure 9.

In figure 11 we compare the spectral function at finite μ for our regulated quantum electron star (blue data points) to the fermionic spectral function in a pure AdS_4 background with finite chemical potential, either with (green line) and without (red line) regulation by the confining scalar. The comparison is given at $k = 0$ (left) and $k = 1$ (right). The Dirac

JHEP08(2022)222

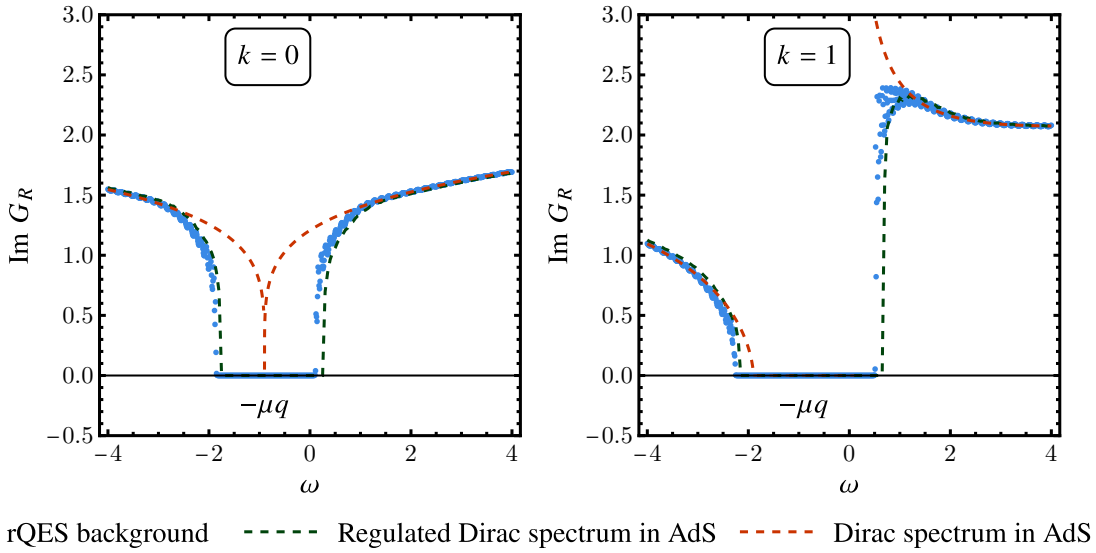

Figure 11. (Confined) Dirac spectral function (blue points) in the rQES background for $k = 0$ (left) and $k = 1$ (right), compared with the standard/unconfined (red dashed line) and regulated/confined (green dashed line) Dirac spectral function in AdS with finite electrostatic potential.

spectrum in AdS_4 is well-known [30]:

$$G_R(\omega,k) = \begin{cases} \dfrac{2}{\omega^2-k^2}\dfrac{\Gamma(1/2-m)}{\Gamma(1/2+m)}\left[-\dfrac{i}{2}\left(\omega^2-k^2\right)\right]^{2m+1}\left[\omega\gamma^0-k\gamma^1\right] & \text{if } \omega > k\,, \\ \dfrac{2}{\omega^2-k^2}\dfrac{\Gamma(1/2-m)}{\Gamma(1/2+m)}\left[\dfrac{i}{2}\left(\omega^2-k^2\right)\right]^{2m+1}\left[\omega\gamma^0-k\gamma^1\right] & \text{if } \omega < -k\,. \end{cases} \tag{3.12}$$

It has a conformal branch-cut at $\omega = k$ and a gap for $\omega^2 < k^2$. For AdS_4 with finite electrostatic potential, one merely needs to replace $\omega \to \omega + \mu q$ in the previous expression. Adding confining potential by turning on the chirality-breaking flat scalar widens the gap to $(\omega+\mu q)^2 < k^2 + \lambda^2$; in particular the gap is open also at $k = 0$. The rQES solution outside the gap exhibits qualitatively the same spectral function as that of the confined Dirac spectrum in pure AdS_4 but for renormalized IR values $\omega_{\rm IR}, k_{\rm IR}, \lambda_{\rm IR}$ given in (2.25). It is important to emphasize that none of the modes in this continuum are normalizable and thus do not contribute when building the bulk rQES, even when μq is large enough that $\omega_+(k) < 0$. This is guaranteed by our choice of UV boundary conditions.

4 Towards a self-confining quantum electron star

4.1 Comparison to the holographic superconductor

By construction the confinement in our setup gives an AdS_4-to-AdS_4 solution. With the fully backreacted solution in hand we can also understand what the field theory dual describes. The confining regulator scale λ gaps the field theory fermion spectral function. Considering then the RG flow from the IR emergent conformal field theory towards the UV, this means that as one increases the energy scale it takes a finite distance for occupiable fermion states

JHEP08(2022)222

to be encountered. This can also be seen in the band structure of figure 6. At this scale the theory deforms away from the strict conformal theory up to the scale μ beyond which it is no longer energetically favorable to occupy more states. The flow up the RG then continues towards the UV AdS_4 fixed point.

In the more usual flow from the UV to the IR this is not a natural RG trajectory. The generic IR will not be a non-trivial conformal field theory. Nevertheless, within holography such AdS_4-to-AdS_4 domain walls are well-known. Especially in the search for the holographic dual of the holographic superconductor ground state, Horowitz and Roberts and independently Gubser and Rocha have found AdS_4-to-AdS_4 domain walls (in some cases with logarithmic corrections) in a finite parameter range [16, 17]; the other solution found is the Lifshitz geometry. It was later understood that Lifshitz rather than an AdS_4 IR is the generic holographic superconductor ground state [17, 18], but this is only seen with the inclusion of a stabilizing quartic potential.

In detail of course the solutions are different. The Horowitz-Roberts-Gubser-Rocha holographic superconductor ground states do not need an additional confining scalar. They can also be obtained classically without the need for a one-loop Hartree mean field. This is due to the fact that the bosonic field already couples quadratically to the electrostatic potential A_t. A fermion only couples linearly, but its one-loop contribution can couple at all orders. This is why for fermionic systems one needs to go to one-loop.

4.2 Confinement in the rQES solution

Given that the Horowitz-Roberts-Gubser-Rocha AdS_4-to-AdS_4 solutions do not need a confining potential, and that the more generic holographic superconductor Lifshitz solutions are known, it is a natural question why we do not try to remove the soft-confining regulator alltogether. There was in fact a concerted effort to do so several years ago [5, 9, 12], culminating in the QES model of [14, 15]. The latter two articles show in detail how the presence of the gap and the discretized spectrum are crucial to construct any type of quantum fermionic backreacted solution, i.e. where one or a small finite number of radial modes are occupied. Any attempt to remove the confining potential results in a uncontrolled continuum spectrum.

It is precisely this insight that was the starting point for our confining potential. What we have furthermore shown, is that even then there are several severe technical hurdles to overcome to construct a converging fully backreacted confined quantum electron star solution. At the same time the general insight still holds. Our infrared boundary conditions crucially depend on the coupling to the scalar $\Phi(z)$ to extend the domain of existence of normalizable modes of AdS_4 all the way to $k = 0$. The parameter λ, as we previously noted, acts as a momentum shift in this domain such that a mode at $k = 0$ will behave as a mode at $k_{\text{eff}} = \lambda$ and therefore normalizable modes with $|\omega + \mu q| < \lambda$ will be found. These can be populated and will condense in the bulk. Turning off the potential, even slowly, will invariably lead to a lack of normalizable modes at the lowest momenta and will bring us back to a situation similar to that of AdS_4.

One sliver of hope would be that the domain wall solution itself, after convergence, can support a well in the Schrödinger potential such that a regulator is no longer necessary. We have therefore looked at this (figure 12) by comparing the Schrödinger potential for a $k = 0$,

JHEP08(2022)222

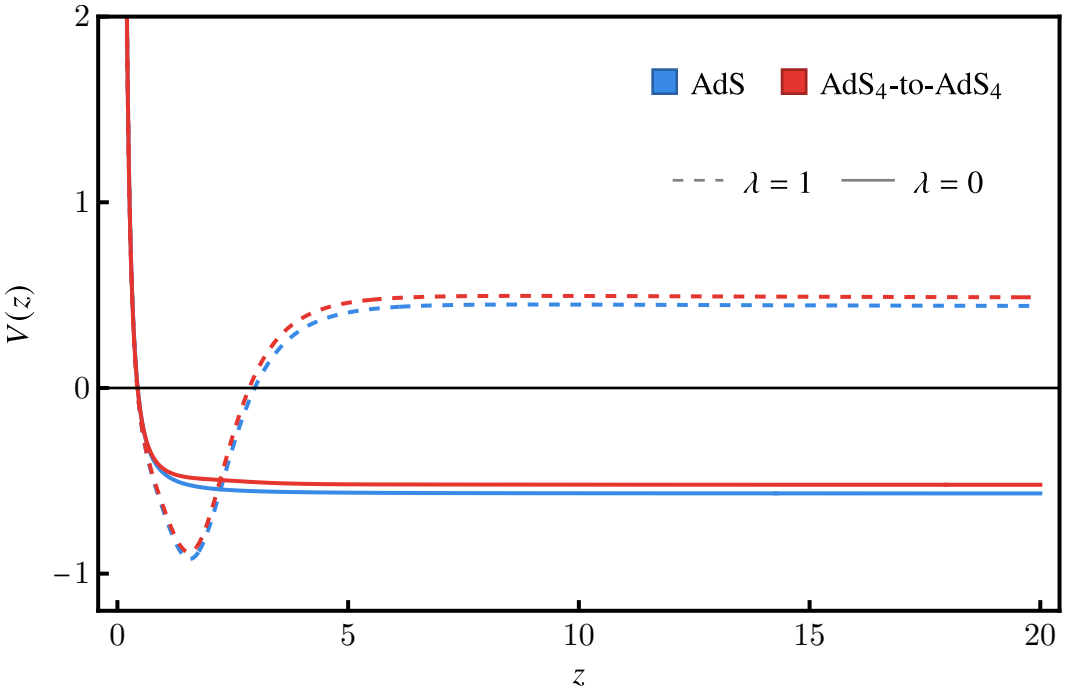

Figure 12. Comparison of the Schrödinger potential for the AdS_4 (blue) and AdS_4-to-AdS_4 (red) solutions with (dashed) and without (solid) regulator, for $\{m, \mu q, k, \omega\} = \{0.1, 1.05, 0, -0.027\}$.

$\omega = E_1(0)$ mode in the confined quantum electron star AdS_4-to-AdS_4 background with and without the confining potential. Without a potential, however, the AdS_4-to-AdS_4 quantum electron star domain wall solution is not confining. We do see that $V_{\text{domain wall}}(z \to \infty) > V_{\text{AdS}}$ which means the wedge of existence of normalizable modes is indeed wider in the domain wall solution than in the AdS_4 solution. Yet, the modes with sufficiently small momenta (including $k = 0$) are always outside the wedge.

This therefore leads us to believe a true QES would not *remove* the regulator but must *incorporate* it into the model, i.e. make the scalar field a dynamical dilaton which couples to the Dirac fermion and drives the geometry from one fixed point to another.

5 Discussion and conclusions

In this paper we have constructed a self-consistent model of a single band confined holographic Fermi liquid. The crucial technical problem, the infrared divergence brought about by the fermionic wavefunctions, is solved by controlling it by hand. We control the far infrared by the means of a scalar regulator, equivalent to a soft-confining potential. The confinement is drastic and 100%: our regulated quantum electron star is dual to a gas of infinitely-long living particles with zero self-energy. In the limit where we compute, it is a single-band Fermi-gas rather than a Fermi-liquid.[6] At higher energies, the spectrum switches to the featureless continuum inherited from the UV conformal field theory (though it is not conformally invariant due to the presence of the confining potential).

[6]This holds at zero temperature. At finite temperature a black hole horizon would form, causing inevitably some dissipation even in the presence of the confinement.

JHEP08(2022)222

The regulated quantum electron star is the thermodynamically preferred solution over the Reissner-Nordström background for $\mu q/m > (\mu q/m)_{\text{critical}}$. The transition is first order, which means that the there is no continuous exchange of charge from the RN solution to the bulk Fermi sea. Instead all the charge is carried by the infinitesimally small rQES. This is somewhat different from the conundrum that we mention in the Introduction: the onset of a log-oscillatory signal in the spectral function signaling a putative instability and the presence of normalizable solutions. The first order transition is essentially unrelated to the RN horizon instability.

Although it is not yet clear how the rQES is related to the final state after the conjectured continuous quantum phase transition which destroys the Reissner-Nordström black hole horizon signalled by the log-oscillatory instability, we nevertheless feel it is a step in the right direction, bringing us closer to the full unregulated quantum electron star. The reasons are the following:

1. It is now much clearer what a healthy Fermi liquid should do on the gravity side: it should self-consistently form a geometry which yields such an effective potential for the Dirac fermion that it is just confined enough not to diverge in far IR but not so much that the bulk Fermi sea dies out in the far IR, failing to influence the low-energy physics.

2. We have inspected in some detail the spectrum and the phenomenology of the dual confined Fermi liquid. Although our confining bulk construction is somewhat more natural in holography — it just uses a non-dynamical rather than a dynamical scalar — than the hard-wall model [13], and it now allows us to compute the backreaction, qualitatively the field-theory side description is only marginally improved. Similar to the hard-wall model, the occupied fermions have vanishing self-energy. The main effect of the backreaction is to understand how this confined Fermi gas emerges in an RG-flow from the UV conformal field theory. In the likely event that an unregulated (confining) quantum electron star — supported for instance by a dynamical rather than a non-dynamical scalar (such as the fluid electron star in [19]) — has a Lifshitz IR rather than an AdS_4 IR, possible decay into the Lifshitz horizon could provide a finite lifetime and an honest Fermi liquid.

3. Unlike the global AdS radius regulator of [15] which cannot be easily sent to infinity, our scalar can at least in principle be made dynamical. That would be a perfectly natural holographic model, given the ubiquity of non-minimally coupled scalars in top-down holographic actions. Therefore, a very natural line of further research is to turn this construction into a fully dynamical Einstein-Maxwell-Dirac-scalar system, similar to the fluid approach of [19].

Apart from the natural next step — making the dilaton dynamic — a number of other directions of work open up. It would be useful to understand the relation of our work to the AdS/QCD studies, some of which employ a similar type of scalar (soft wall) to impose confinement. The role of the Fock correction (the one-loop exchange diagram) is also not clear yet, and may be important for a fully self-regulating solution and/or a finite self-energy. Finally, the most characteristic property of rQES — the domain-wall-type solution with

JHEP08(2022)222

an infrared AdS_4, is analogous to the domain-wall holographic superconductor solutions of Horowitz-Roberts-Gubser-Rocha [16, 18, 31]. Based on those results and the macroscopic electron star with dynamical dilaton studied in [19], it strongly suggests that Lifshitz IR quantum electron stars must also exist.

Acknowledgments

We thank Jan Zaanen for discussions. This reserach has made use of the excellent Sci-Hub service. This research was supported in part by the Netherlands Organization for Scientific Research (NWO) (project 680-91-116 *Planckian dissipation and quantum thermalisation: from black hole answers to strange metal questions*; project FOM-164 *Scanning New Horizons*), the Netherlands Organization for Scientific Research/Ministry of Science and Education (NWO/OCW), Ministry of Education, Science and Technological Development of the Republic of Serbia and Science Fund of the Republic of Serbia, under the Key2SM project (PROMIS program, Grant No. 6066160).

References

[1] L. Huijse and S. Sachdev, *Fermi surfaces and gauge-gravity duality*, *Phys. Rev. D* **84** (2011) 026001 [arXiv:1104.5022] [INSPIRE].

[2] H. Liu, J. McGreevy and D. Vegh, *Non-Fermi liquids from holography*, *Phys. Rev. D* **83** (2011) 065029 [arXiv:0903.2477] [INSPIRE].

[3] M. Cubrovic, J. Zaanen and K. Schalm, *String Theory, Quantum Phase Transitions and the Emergent Fermi-Liquid*, *Science* **325** (2009) 439 [arXiv:0904.1993] [INSPIRE].

[4] T. Faulkner, H. Liu, J. McGreevy and D. Vegh, *Emergent quantum criticality, Fermi surfaces, and AdS_2*, *Phys. Rev. D* **83** (2011) 125002 [arXiv:0907.2694] [INSPIRE].

[5] S.A. Hartnoll and A. Tavanfar, *Electron stars for holographic metallic criticality*, *Phys. Rev. D* **83** (2011) 046003 [arXiv:1008.2828] [INSPIRE].

[6] V.G.M. Puletti, S. Nowling, L. Thorlacius and T. Zingg, *Holographic metals at finite temperature*, *JHEP* **01** (2011) 117 [arXiv:1011.6261] [INSPIRE].

[7] S.A. Hartnoll and P. Petrov, *Electron star birth: A continuous phase transition at nonzero density*, *Phys. Rev. Lett.* **106** (2011) 121601 [arXiv:1011.6469] [INSPIRE].

[8] S.A. Hartnoll, D.M. Hofman and D. Vegh, *Stellar spectroscopy: Fermions and holographic Lifshitz criticality*, *JHEP* **08** (2011) 096 [arXiv:1105.3197] [INSPIRE].

[9] M. Cubrovic, Y. Liu, K. Schalm, Y.-W. Sun and J. Zaanen, *Spectral probes of the holographic Fermi groundstate: dialing between the electron star and AdS Dirac hair*, *Phys. Rev. D* **84** (2011) 086002 [arXiv:1106.1798] [INSPIRE].

[10] J. Zaanen, Y. Liu, Y.-W. Sun and K. Schalm, *Holographic Duality in Condensed Matter Physics*, Cambridge University Press (2015) [DOI].

JHEP08(2022)222

[11] S.A. Hartnoll, A. Lucas and S. Sachdev, *Holographic quantum matter*, arXiv:1612.07324 [INSPIRE].

[12] M.V. Medvedyeva, E. Gubankova, M. Čubrović, K. Schalm and J. Zaanen, *Quantum corrected phase diagram of holographic fermions*, *JHEP* **12** (2013) 025 [arXiv:1302.5149] [INSPIRE].

[13] S. Sachdev, *A model of a Fermi liquid using gauge-gravity duality*, *Phys. Rev. D* **84** (2011) 066009 [arXiv:1107.5321] [INSPIRE].

[14] A. Allais, J. McGreevy and S.J. Suh, *A quantum electron star*, *Phys. Rev. Lett.* **108** (2012) 231602 [arXiv:1202.5308] [INSPIRE].

[15] A. Allais and J. McGreevy, *How to construct a gravitating quantum electron star*, *Phys. Rev. D* **88** (2013) 066006 [arXiv:1306.6075] [INSPIRE].

[16] G.T. Horowitz and M.M. Roberts, *Zero Temperature Limit of Holographic Superconductors*, *JHEP* **11** (2009) 015 [arXiv:0908.3677] [INSPIRE].

[17] S.S. Gubser and F.D. Rocha, *The gravity dual to a quantum critical point with spontaneous symmetry breaking*, *Phys. Rev. Lett.* **102** (2009) 061601 [arXiv:0807.1737] [INSPIRE].

[18] S.S. Gubser and A. Nellore, *Ground states of holographic superconductors*, *Phys. Rev. D* **80** (2009) 105007 [arXiv:0908.1972] [INSPIRE].

[19] S.A. Hartnoll and L. Huijse, *Fractionalization of holographic Fermi surfaces*, *Class. Quant. Grav.* **29** (2012) 194001 [arXiv:1111.2606] [INSPIRE].

[20] C.P. Herzog, *A Holographic Prediction of the Deconfinement Temperature*, *Phys. Rev. Lett.* **98** (2007) 091601 [hep-th/0608151] [INSPIRE].

[21] G.F. de Teramond and S.J. Brodsky, *Excited Baryons in Holographic QCD*, *AIP Conf. Proc.* **1432** (2012) 168 [arXiv:1108.0965] [INSPIRE].

[22] A. Karch, E. Katz, D.T. Son and M.A. Stephanov, *Linear confinement and AdS/QCD*, *Phys. Rev. D* **74** (2006) 015005 [hep-ph/0602229] [INSPIRE].

[23] Z. Fang, D. Li and Y.-L. Wu, *IR-improved Soft-wall AdS/QCD Model for Baryons*, *Phys. Lett. B* **754** (2016) 343 [arXiv:1602.00379] [INSPIRE].

[24] N. Iizuka, N. Kundu, P. Narayan and S.P. Trivedi, *Holographic Fermi and Non-Fermi Liquids with Transitions in Dilaton Gravity*, *JHEP* **01** (2012) 094 [arXiv:1105.1162] [INSPIRE].

[25] L.D. Landau and E.M. Lifshitz, *Statistical Physics, Part 2: Theory of the Condensed State*, Fizmatlit (2004).

[26] S.S. Gubser, F.D. Rocha and P. Talavera, *Normalizable fermion modes in a holographic superconductor*, *JHEP* **10** (2010) 087 [arXiv:0911.3632] [INSPIRE].

[27] F. Denef, S.A. Hartnoll and S. Sachdev, *Quantum oscillations and black hole ringing*, *Phys. Rev. D* **80** (2009) 126016 [arXiv:0908.1788] [INSPIRE].

[28] K. Hashimoto and N. Iizuka, *A Comment on Holographic Luttinger Theorem*, *JHEP* **07** (2012) 064 [arXiv:1203.5388] [INSPIRE].

[29] N. Iqbal, H. Liu and M. Mezei, *Semi-local quantum liquids*, *JHEP* **04** (2012) 086 [arXiv:1105.4621] [INSPIRE].

[30] N. Iqbal and H. Liu, *Real-time response in AdS/CFT with application to spinors*, *Fortsch. Phys.* **57** (2009) 367 [arXiv:0903.2596] [INSPIRE].

[31] G. Horowitz, A. Lawrence and E. Silverstein, *Insightful D-branes*, *JHEP* **07** (2009) 057 [arXiv:0904.3922] [INSPIRE].

JHEP08(2022)222